2013

Multi-physics Model Of Key Components In High Efficiency Vehicle Drive

Shao Hua Lin
University of Central Florida

MULTI-PHYSICS MODELING OF KEY COMPONENTS IN HIGH EFFICIENCY VEHICLE DRIVE

by

SHAOHUA LIN
B.S. in Electrical Engineering, University of Central Florida, 2005
M.S. in Electrical Engineering, University of Central Florida, 2007

A dissertation submitted in partial fulfillment of the requirements
for the degree of Doctor of Philosophy
in the Department of Electrical Engineering and Computer Science
in the College of Engineering and Computer Science
at the University of Central Florida
Orlando, Florida

Fall Term
2013

Major Professor: Thomas Wu

ABSTRACT

Hybrid Electric Vehicles (HEVs) and Electric Vehicles (EVs) are crucial technologies for the automotive industry to meet society's demands for cleaner, more energy efficient transportation. Meeting the need to provide power which sustains HEVs and EVs is an immediate area of concern that research and development within the automotive community must address. Electric batteries and electrical motors are the key components in HEV and EV power generation and transmission, and their performance plays very important role in the overall performance of the modern high efficiency vehicles. Therefore, in this dissertation, we are motivated to study the electric batteries, interior permanent motor (IPM), in the context of modern hybrid electric/electric drive systems, from both multi-physics and system level perspectives. Electrical circuit theory, electromagnetic Finite Element Analysis (FEA), and Computational Fluid Dynamic (CFD) finite volume method will be used primarily in this work. The work has total of five parts, and they are introduced in the following.

Firstly, Battery thermal management design is critical in HEV and EV development. Accurate temperature distribution of the battery cells during vehicle operation is required for achieving optimized design. We propose a novel electrical-thermal battery modeling technique that couples a temperature dependent battery circuit model and a physics-based CFD model to meet this need. The electrical circuit model serves as a heat generation mechanism for the CFD model, and the CFD model provides the temperature distribution of the battery cells, which can also impact the heat generation of the electrical battery model. In this part of work, simulation data has been derived from the model respective to electrical performance of the battery as well

as the temperature distribution simultaneously in consideration of the physical dimensions, material properties, and cooling conditions. The proposed model is validated against a battery model that couples the same electrical model with a known equivalent thermal model.

Secondly, we propose an accurate system level Foster network thermal model. The parameters of the model are extracted from step responses of the CFD battery thermal model. The Foster network model and the CFD model give the same results. The Foster network can couple with battery circuit model to form an electric-thermal battery model for system simulation.

Thirdly, IPM electric machines are important in high performance drive systems. During normal operations, irreversible demagnetization can occur due to temperature rise and various loading conditions. We investigate the performance of an IPM using 3d time stepping electromagnetic FEA considering magnet's temperature dependency. Torque, flux linkage, induced voltage, inductance and saliency of the IPM will be studied in details. Finally, we use CFD to predict the non-uniform temperature distribution of the IPM machine and the impact of this distribution on motor performance.

Fourthly, we will switch gear to investigate the IPM motor on the system level. A reduced order IPM model is proposed to consider the effect of demagnetization of permanent magnet due to temperature effect. The proposed model is validated by comparing its results to the FEA results.

Finally, a HEV is a vehicle that has both conventional mechanical (i.e. internal combustion engine) and electrical propulsion systems. The electrical powertrain is used to work with the conventional powertrain to achieve higher fuel economy and lower emissions.

Computer based modeling and simulation techniques are therefore essential to help reduce the design cost and optimize system performance. Due to the complexity of hybrid vehicles, multi-domain modeling ability is preferred for both component modeling and system simulation. We present a HEV library developed using VHDL-AMS.

ACKNOWLEDGMENTS

I would like to express my deepest gratitude to my advisor Prof. Thomas Wu for his guidance, inspiration, and patience throughout my study since my undergraduate at UCF. I really appreciate the opportunity to work under his guidance. I would like to thank Prof. Louis Chow for his kindly support, understanding, and advice in my study. I would like to thank all my defense committee members Dr. Kalpathy Sundaram, Dr. Parveen Wahid, and Dr. Lei Wei for their kindly assistance and willingness. Finally, I would like to especially thank my dear father Dongwen Lin and mother Ruifen Li, and my lovely wife Qingqiu Mao. They love and support me in every possible way, I love them with all my heart and I am indebted to them forever.

TABLE OF CONTENTS

LIST OF FIGURES

CHAPTER 1: INTRODUCTION

Hybrid electric vehicle and electric vehicle are the future trend of automotive industry. Among the extensive research in the related areas in HEV/EV development, battery [1]-[25] and permanent magnet motor [26]-[50] modeling have been two of the most important topics because they provide sustaining power for both HEV and EV on the road. In this dissertation, our primary research interests are modeling battery and interior permanent magnet (IPM) motors on both device and system levels from multi-physics perspective.

One of the major challenges in battery development is battery thermal management design. Without optimized cooling design, high temperature rise or local hot spots could lead to battery degradation and thermal runaway. The existing models can either provide temperature distribution or heat generation. However, a model that predicts both is highly desirable. Therefore, we propose a novel electrical-thermal modeling technique that couples a temperature dependent battery circuit model and a CFD model. The circuit model serves as a heat generation mechanism for the CFD model, and the CFD model provides the temperature distribution of the battery cells, which can affect the heat generation of the electrical battery model.

Thermal network model and battery circuit model are coupled to study the battery performance considering temperature effect. Thermal capacitance and thermal resistance are used in the thermal network model. In order to obtain accurate results, the number of thermal capacitors and resistances is large to achieve good accuracy there the thermal network model can be quite complex to calibrate. To replace the thermal network, we propose a Foster network thermal model. Foster network model also consists of capacitors and resistors, however they do

not have the same physical meaning like those in the traditional thermal network, instead they represent the transfer function of the thermal system. We extract the values of the capacitors and resistors in the Foster network from the step responses of the battery thermal system, which can be obtained either from CFD simulation or testing. The results of Foster network are the same as the CFD model but it is simulation time is comparable to the traditional thermal network therefore it is suitable for system simulation with very high accuracy.

Interior permanent magnet (IPM) motors [51]-[75] are widely used in various high-performance electric and hybrid electric vehicles. When an IPM machine is overloaded or after a short circuit, irreversible demagnetization may occur due to a strong demagnetizing field and/or temperature increases. Demagnetization can significantly reduce the magnet's ability to create flux, which, in turn, decreases the electric machine's overall efficiency. Overloading and temperature rise can happen independently or simultaneously during a fault or during normal operation. Temperature gradients in the magnet often cause different parts of the magnet to demagnetize non-uniformly. We will study the temperature effects on the IPM motor's electrical and mechanical performance.

Finite Element Analysis (FEA) [75]-[100] is one of the most popular tools used to carry out study and design of IPM. FEA provides detailed electrical and magnetic performance of the IPM considering material properties, excitation, physical dimensions, and etc. Therefore, FEA is well suited for IPM designers to design and optimize the machine. However, for system level simulation, the speed of FEA is not ideal. For system level simulation, we are concerned about the performance of the entire system rather than just the IPM. So it is desirable to have an IPM

model that is accurate enough to capture the main characteristic of physics, but runs at circuit simulation speed. Also, the permanent magnet materials are temperature dependency should be included. Therefore we propose a reduced order IPM model that considers the magnet temperature dependency. We will validate the proposed model using the FEA results.

Including electrical powertrain into the conventional vehicle drive system has increased the research costs. Computer based modeling and simulation techniques are therefore essential to help reduce the design cost and optimize system performance. We present a new HEV library developed using VHDL-AMS. The library provides reusable and extensible generic components for further design.

1.1. Organization of the Dissertation

In Chapter 2, the implementation of the proposed multi-physics battery model is provided. The model can predict battery temperature distribution and heat generation.

In Chapter 3, an LIT thermal model is presented for battery. The method is simple but very accurate. The implementation and validation of the proposed model will be provided.

In Chapter 4, the change in the performance of IPM motor as temperature increases and load changes will be studied in details using FEA and CFD.

In Chapter 5, we propose a novel reduced order temperature dependent IPM model which is suitable for system level simulation. We will discuss the implementation and validation in details.

In Chapter 6, we introduce the VHDL-AMS modeling library for vehicles.

In Chapter 7, the conclusion of the dissertation is drawn.

CHAPTER 2: ELECTRICAL THERMAL BATTERY MODELING

2.1. Background

HEV and EV are crucial technologies for the automotive industry to meet society's demands for cleaner, more energy efficient transportation. Meeting the need to provide power which sustains HEVs and EVs is an immediate area of concern that research and development within the automotive community must address. Considering this power concern, extensive efforts have been undertaken to develop battery modeling methodologies that can expedite industrial implementation. One of the major challenges in battery development is battery thermal management design. Without optimized cooling design, high temperature rise or local hot spots could lead to battery degradation and thermal runaway. Therefore the usage of physics-based simulation method to obtain battery's temperature distribution is required for HEV/EV battery thermal management design.

A particular physics based simulation method is CFD which has been quite popular for battery pack thermal management design as in [101]-[102]. CFD can accurately predict temperature distribution based on the given heat generation, fluid cooling conditions, geometry, material properties, and other essential parametric criteria. However, inherently CFD cannot accurately establish heat generating mechanisms that involves electrochemistry. Therefore, performing CFD analysis usually requires user to provide pre-defined heat source profile obtained from either measurement or other heat estimation methods. Notice obtaining the heat generation and temperature individually is very common in battery thermal management design, simply neglecting the coupling between them. This assumption could be invalid if the battery loading changes rapidly, which could happen during a normal drive cycle of the HEV or EV.

Electrochemical model is the most accurate model in terms of predicting heat generation because it describes the fundamental physics of the electrochemical process in battery cells [103]-[104]. However, this model requires in-depth knowledge of the electrochemistry, so it is not easy for thermal management design engineer to use on a daily basis.

Battery circuit models have gained popularity in recent battery modeling research and development [105]-[109]. The parameters of the circuit models are usually curve fitted from measurement data. They can accurately predict electrical performance values such as heat generation, load voltage, battery run time, state of charge, non-linear capacity effect, and etc. Electrical circuit models are mature and are inherently well understood by electrical engineers; however, these methods that would afford a great deal of utility cannot provide temperature distribution which becomes exclusionary for such analysis to be used for battery thermal management design.

The ability to offer battery thermal designers a methodology to systematically predict accurate heat generation within the battery cells and to provide temperature distribution simultaneously of the battery system would be a tremendous asset for HEV/EV battery thermal management design. This is the motivation to propose a methodology based on the preliminary work we first proposed in [110].

We propose a novel electrical-thermal modeling technique that couples a temperature dependent battery circuit model and a CFD model. The circuit model serves as a heat generation mechanism for the CFD model, and the CFD model provides the temperature distribution of the battery cells, which can impact the heat generation of the electrical battery model.

2.2. Model Implementation

The proposed electric-thermal battery analysis consists of a temperature dependent battery electrical circuit model and a CFD model. Both a circuit solver and CFD solver are required to undertake the analysis. The heat generated by the circuit model for each time step is sent to CFD model as the heat source. The CFD model utilizes this heat source to calculate the temperature distribution, and the averaged volumetric temperatures of the battery cells are sent back to the battery electrical circuit model to calculate the heat generation for the next time step. The heat and temperature are processed iteratively between the two solvers until the user defined termination of simulation time. The circuit model is implemented in Simplorer and the CFD model is implemented in Fluent. The battery electrical circuit model is referred to as the circuit model in this work; battery electrical circuit model coupled with the CFD model is called circuit-CFD model. Circuit-CFD model is ultimately the proposed methodology for analysis.

2.2.1. Temperature Dependent Circuit Model

The model in [105] is selected as the base line circuit model due to its simplicity and general acceptance [111]-[115]. Figure 2.1 shows the circuit model. The circuit model as shown would drive a current load and the voltage designated as V_{load} across the current load will be defined as the load voltage of the battery. I_{load} is the current loading applied to the model, $R_{transient\_l}$ and $C_{transient\_l}$ represent the long time constant effect, $R_{transient\_s}$ and $C_{transient\_s}$ represent the short time constant effect, R_{series} is the internal resistance, VOC is the open circuited voltage, $C_{capacity}$ is the battery capacity, and $R_{self\_discharge}$ models self-discharge effect. The value for $R_{self\_discharge}$ in the model is infinite because self-discharge time is much longer than the load discharging time. Note that on the left hand side of the circuit, I_{load} is connected in parallel with $C_{capacity}$ and $R_{self\_discharge}$,

the voltage V_{soc} across $C_{capacity}$ is the State of Charge (*SOC*) of the battery. Equations (1) to (6) identify the component values are functions of SOC V_{soc} [106], except I_{load}. $a_{1\text{-}6}$, $b_{1\text{-}3}$, $c_{1\text{-}3}$, $d_{1\text{-}3}$, $f_{1\text{-}3}$, and $g_{1\text{-}3}$ are the coefficients of the functions. To demonstrate the proposed methodology, we used the values provided in [105]. How to generate these coefficients is out of the scope of the work, nevertheless, for any given new battery module, the coefficients should be re-generated. For instance, they can be obtained by using the least-squares method described in [116]-[119].

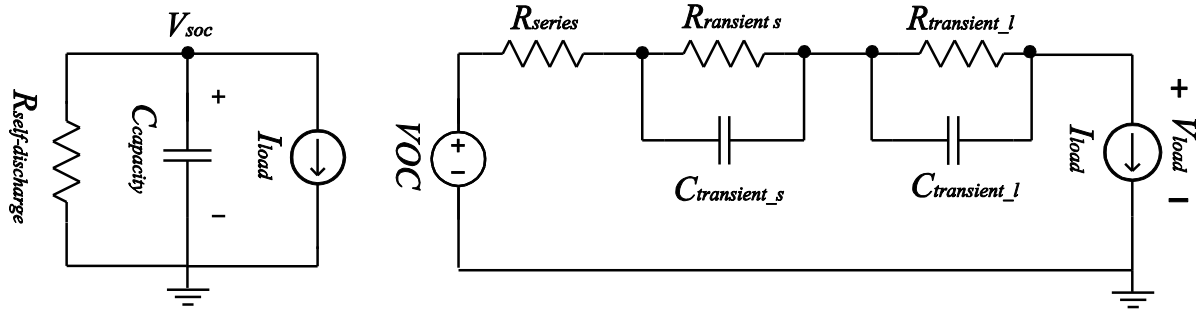

Figure 2.1: Circuit model of a single cell battery.

$$VOC = a_1 e^{a_2 V_{soc}} + a_3 + a_4 V_{soc} + a_5 V_{soc}^2 + a_6 V_{soc}^3 \tag{2.1}$$

$$R_{series} = b_1 e^{b_2 V_{soc}} + b_3 \tag{2.2}$$

$$R_{transient\_s} = c_1 e^{c_2 V_{soc}} + c_3 \tag{2.3}$$

$$C_{transient\_s} = d_1 e^{d_2 V_{soc}} + d_3 \tag{2.4}$$

$$R_{transient\_l} = f_1 e^{f_2 V_{soc}} + f_3 \tag{2.5}$$

$$C_{transient\_l} = g_1 e^{g_2 V_{soc}} + g_3 \tag{2.6}$$

The circuit model in [105] is isothermal. To establish thermal dependence, the thermal effect in [106] is included. The temperature dependency α and rate factor β [106] on the SOC V_{soc} is introduced by equation (7):

$$V_{soc} = 1 - \frac{1}{C_{capacity}} \int_0^t \alpha\beta I_{load} \, dt \tag{2.7}$$

Additionally, a potential correction term, which is a function of battery temperature, is also included to the open-circuit-voltage according to [106]. In this work, we assume that the battery cell exhibits the temperature dependency and rate dependency in [106], which allows us to demonstrate the methodology. For any new given battery cell, these dependencies should be re-established through procedures in [106].

Figure 2.2 shows the load voltage V_{load} of the modified single cell circuit model is temperature dependent under the above assumption. Let the modified model discharge at 1 A current to 3 V when its temperature is at 283, 293, 303, 313, 323, and 333 K. It is important to note that the battery can be damaged due to excessive temperature rise even though it can produce higher load voltage at higher temperature. Therefore monitoring the temperature of battery cells and ensuring the temperature is within the safety range during the entire operation is very important to protecting the battery cells. We will see later our model makes this possible.

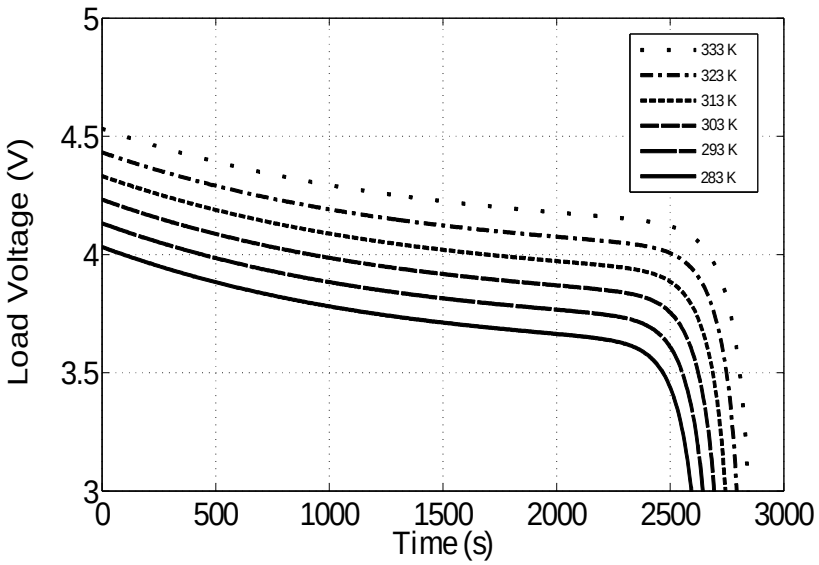

Figure 2.2: Load voltage of a single cell circuit model discharging at 1 A current load at 283, 293, 303, 313, 323, and 333 K.

Figure 2.3 shows how the cell discharges at 0.3, 0.5, 1, 1.5, 2 and 3 A at a temperature of 293 K. The battery discharges faster at higher currents.

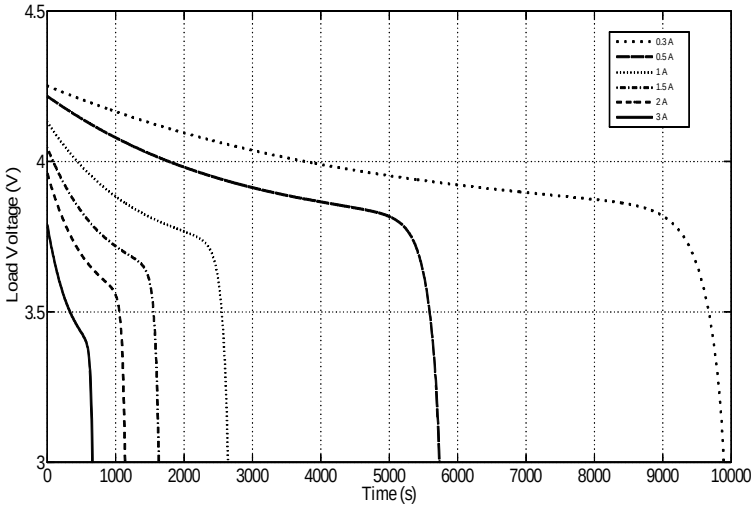

Figure. 2.3: Load voltage of a single cell circuit model discharging at 0.3, 0.5, 1, 1.5, 2, and 3 A, at 293 K.

The modified circuit model is both temperature and loading dependent; therefore, it can be used in the proposed circuit-CFD model. It is worth mentioning that we chose to combine the circuit models proposed in [105] and [106] as our model because of their general acceptance and simplicity. However, the proposed co-simulation methodology is not limited to this circuit model only. Other temperature dependent circuit models could also be used in the proposed circuit-CFD methodology.

2.2.2. 3D CFD Physics Based Model

The 3D CFD model of the single cell battery is shown in Figure 2.4. The blue area is the cooling fluid flow which is typically air or water, and the green cylinder is the battery cell. The radius of the battery cell is 20 mm, the height is 120 mm. Generally, the materials exhibit thermal dependence, but in this work, effective forced convection cooling is assumed and temperature variation is not expected to be large, so the material properties can be taken to be

temperature independent for simplicity. However, the proposed methodology is not limited to temperature independent materials. Fluid mass flow rate is assigned to the inlet boundary, and pressure boundary is assigned to the outlet. The initial temperature of the CFD model is 300 K.

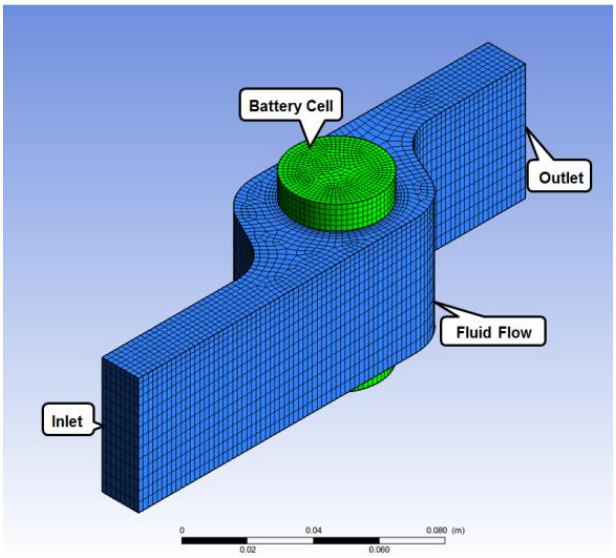

Figure 2.4: CFD model of a single cell battery.

Figure 2.5 displays a temperature distribution from the CFD model. The temperature is plotted on a cross sectional plane. The inner region of the cell has higher temperature, and it decreases towards the surface of the cell as an effect of the cooling fluid. CFD provides good insight into the thermal system, considering geometry, material properties, cooling condition, and etc. This insight is the primary reason for the use of CFD which is widely accepted in battery thermal management design in automotive industry.

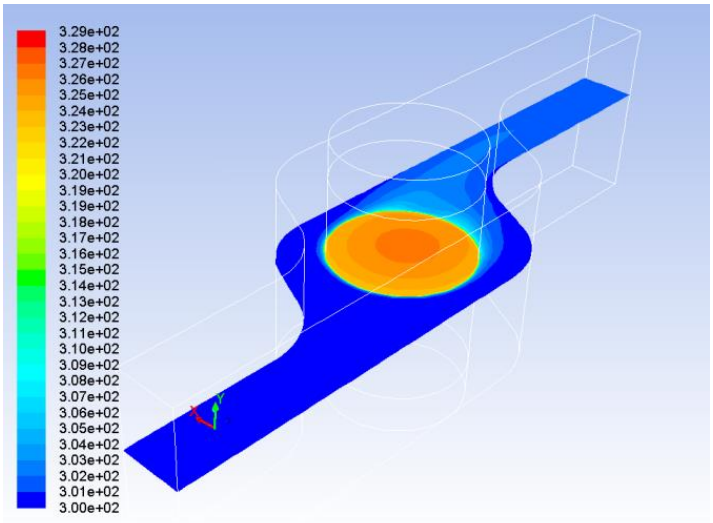

Figure 2.5: CFD temperature distribution of a single battery cell. The range is from 300K to 329K.

2.3. Methodology Execution and Validation

In this section, we will execute and validate the proposed methodology. Figure 2.6 shows a temperature dependent 4-cell circuit model. The model consists of 4 single cell models in section II and they are connected in series to a current load I_{load}. The Load voltage V_{load} is defined as the voltage across I_{load} similarly.

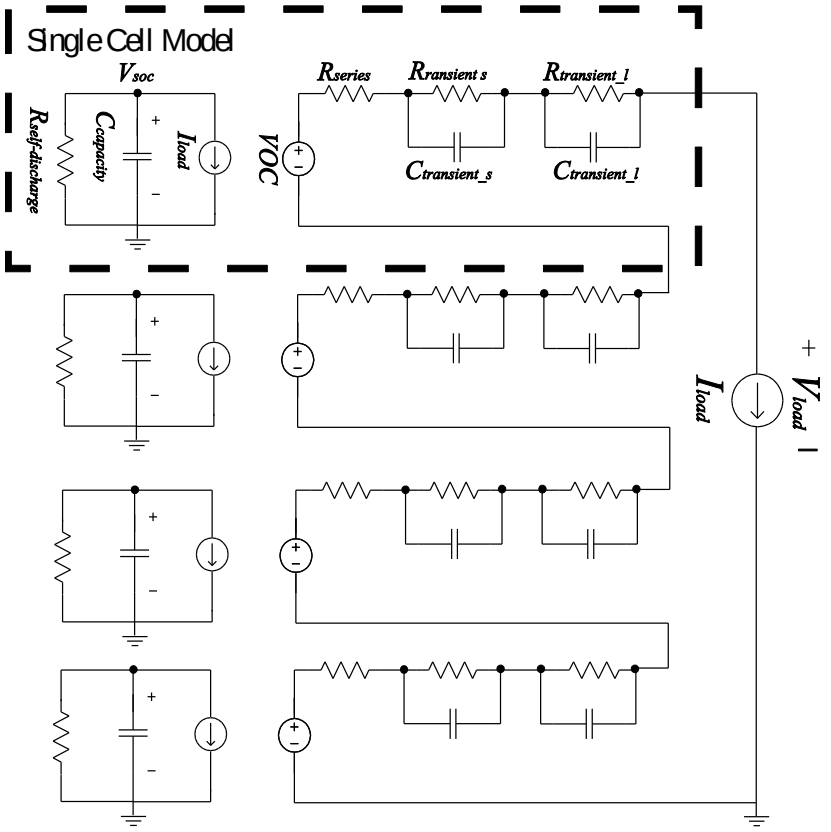

Figure 2.6: 4-cell circuit model. The 4 battery cells are in series connection.

Figure 2.7 displays the load voltage of the 4-cell circuit model at 283 to 333 K, at 10 K increment, discharging by a constant current load of 1 A to 12 V. In addition, Figure. 2.8 shows 6 instances of constant current discharge and the corresponding load voltages at a fixed temperature of 293 K.

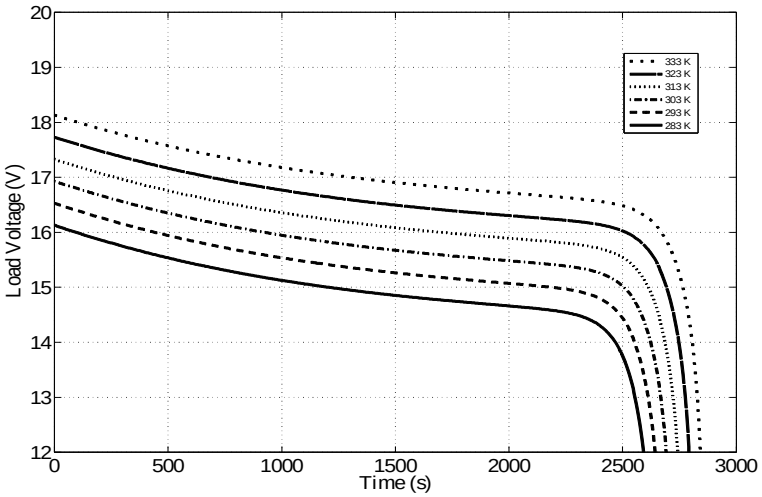

Figure 2.7: Load voltage of the 4-cell electrical circuit battery model discharging by 1 A current load at 283, 293, 303, 313, 323, and 333 K.

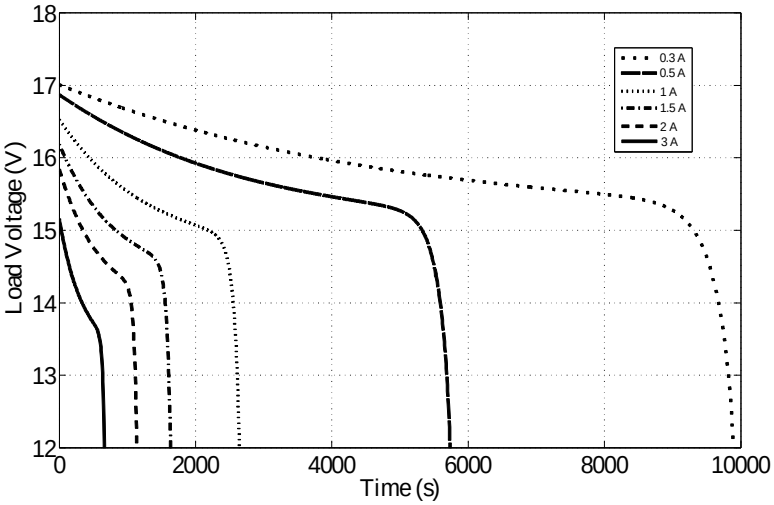

Figure 2.8: Load voltage of the 4-cell circuit model discharging at 0.3, 0.5, 1, 1.5, 2, and 3 A, at 293 K.

The results in Figure 2.7 and Figure 2.8 prove that the 4-cell circuit model is both temperature and current loading dependent, thus it is suitable for the proposed circuit-CFD model.

Additionally, represented in the CFD domain, the 4-cell CFD model is shown in Figure 2.9. The dimensions of the cells are the same as the single battery cell. The cells are placed closely but not touching each other so the flow can provide effective cooling surrounding each cell. The flow region has increased to accommodate the four cells compared to the single cell case. The 4-cell circuit model in Figure 2.6 and the 4-cell CFD model in Figure 2.9 are coupled as described in Section II.

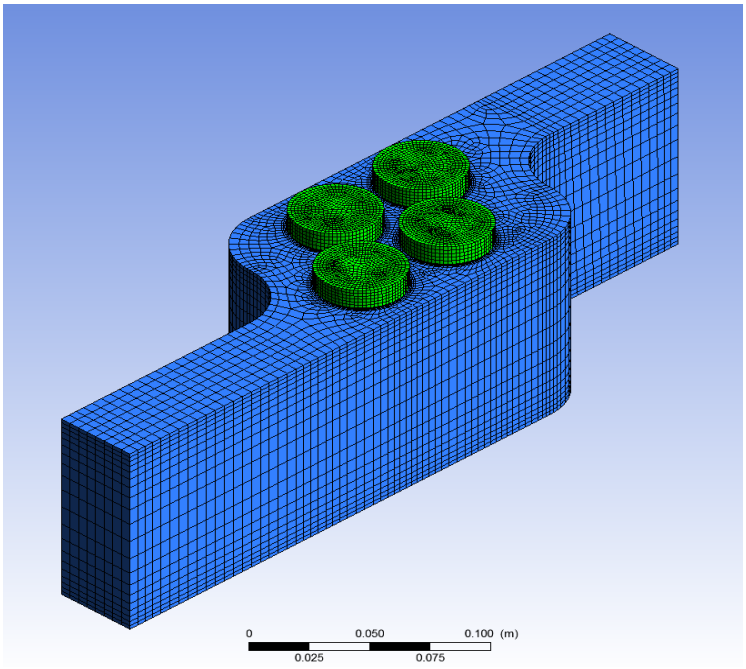

Figure 2.9: 4-cell CFD mesh.

The proposed circuit-CFD methodology obtains solutions using an analog circuit solver and a finite difference CFD solver. The solver executes iteratively in progression of solutions that are coupled through sequential processing and exchange of parameters with relative time steps. The circuit and CFD equations are not solved simultaneously; therefore, it is possible to have

numerical error propagate, accumulate, and lead to a divergent solution. Concerning this divergent possibility, an execution of the methodology is presented. The result of the proposed circuit-CFD model will be compared to the result of its equivalent circuit model where the electrical and thermal equations are modeled and solved in the circuit solver.

The circuit-CFD model is composed of a battery electrical circuit model and a CFD model. If an equivalent circuit thermal model from the CFD model can be generated, it can be shown that the entire model can be modeled within the circuit domain through replacement of the CFD model with the equivalent circuit thermal model.

There are many methods to effectively generate the equivalent model of physics based thermal systems [120]-[124]. In this work, we use the Linear Time Invariant (LTI) method in [20] to extract the equivalent thermal model owing to its simplicity or effectiveness. The circuit model and the LTI thermal model form the circuit-LTI model that can be solved simultaneously in the analog circuit domain. The circuit-LTI model is defined as the simultaneous model to signify its electrical and thermal equations are solved simultaneously. A LTI thermal model is therefore extracted from the 4-cell CFD model in Figure 2.9. The average temperature of each cell is the output of the LTI model, the input is the heat generated by the battery circuit model in Figure 2.6. The process and requirement of generating the LTI model can be found in [120].

Next, 3 defined current loadings Load 1, Load 2 and Load 3 are applied to the circuit-CFD model and the simultaneous model. Load 1 is constant current, Load 2 is pulse current with 50% duty cycle, and Load 3 is from proprietary industrial measurement which has been conditioned as a profile shown in Figure 2.10.

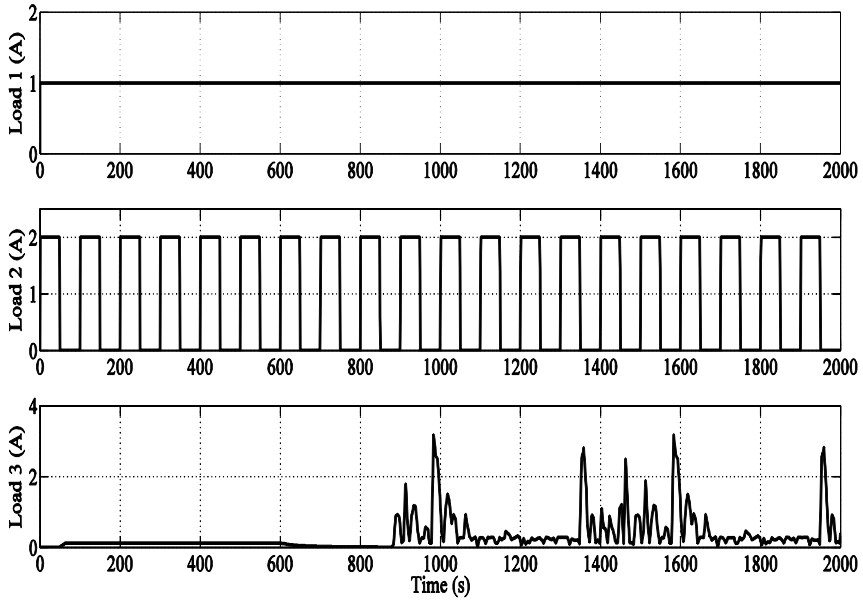

Figure 2.10: 3 current loadings. The duration of each is 2000 seconds. Load 1 is 1A constant current. Load 2 is pulse current with 50% duty cycle. Load 3 is a scaled measurement data.

The load voltages of both models under the 3 current loading profiles are benchmarked in Figure 2.11. The results exhibit very good agreement, notably the differences in the curves are less than 1%. The differences can be explained as numerical error of the proposed model, and the differences are well within generally accepted tolerances for purposes of engineering. The excellent agreement between the circuit-CFD model and simultaneous model validates the proposed circuit-CFD modeling methodology.

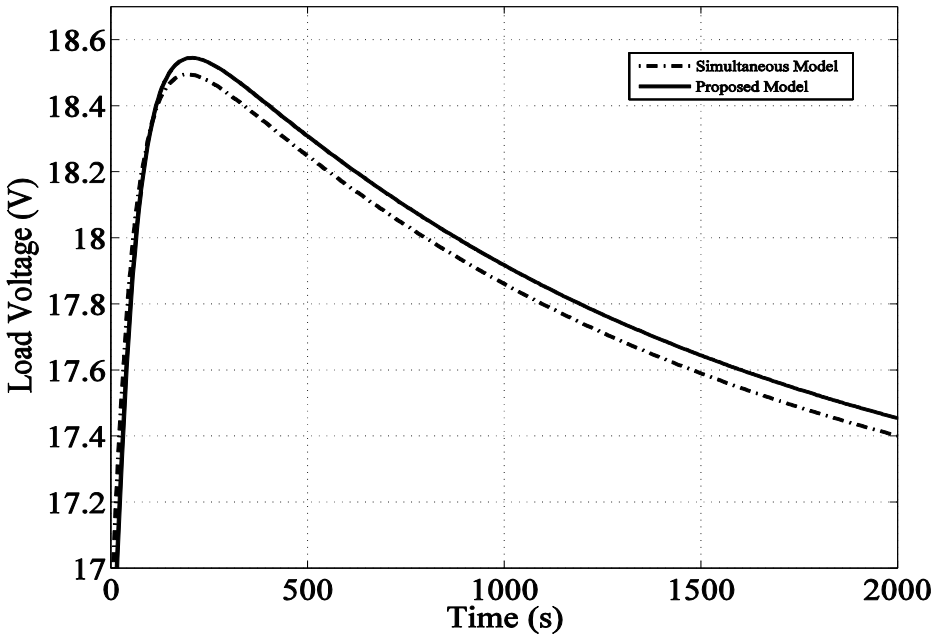

(a) Load voltages under Load 1.

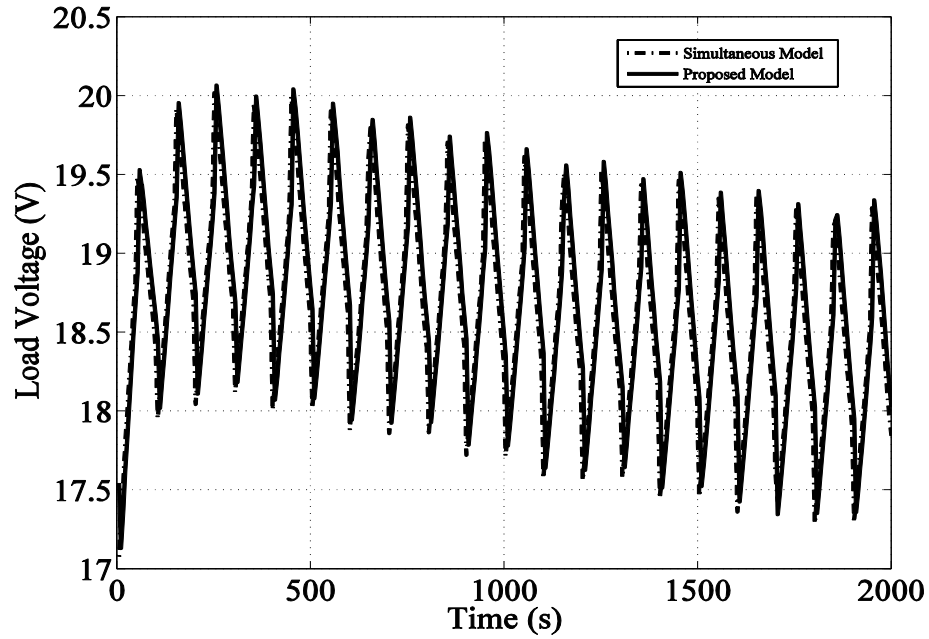

(b) Load voltages under Load 2.

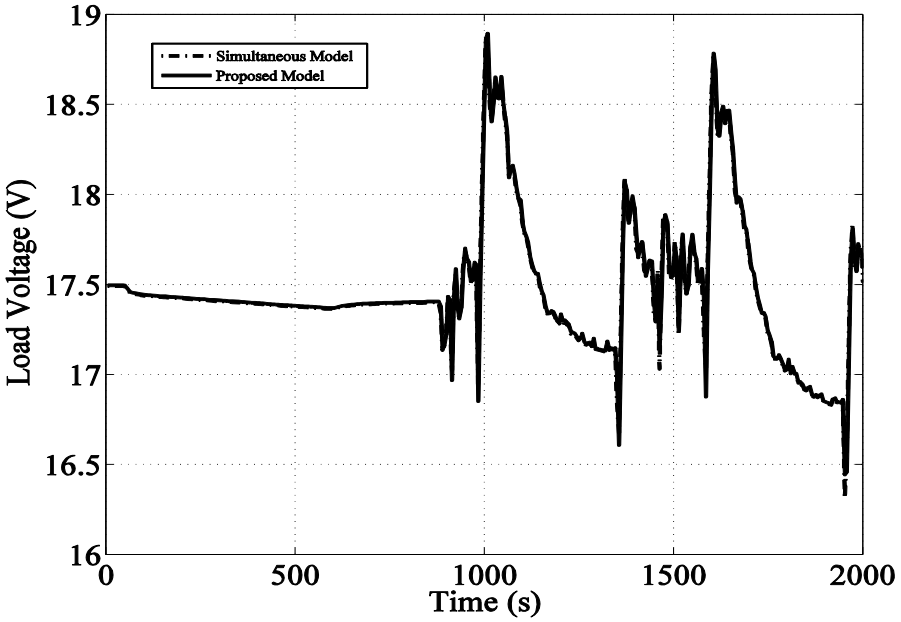

(c) Load voltages under Load 3.

Figure 2.11: 4-cell load voltage comparison between circuit-CFD model and simultaneous model under 3 current loadings

Figure 2.12 shows the temperature distribution of the 4-cell circuit-CFD model at 1600 s, 1620 s, 1640 s, and 1660 s time instants during Load 3 discharging in Figure 2.11 (c). The temperature distributions of cells are different spatially, and the distributions change with as time as well. Due to the heat generation mechanism as provided through the circuit model and the capability of CFD to predict the temperature distributions of the system, the value of the proposed methodology for HEV/EV battery thermal management design is apparent. On the other hand, it is worth noting the simultaneous model can provide electrical terminal results as shown in Figure 2.11, as well as the average cell temperature, but it cannot provide temperature distribution like the proposed model due to its lumped nature. This is also the drawback of any lumped thermal model used in thermal management design. Further supporting analysis will be

presented in section IV when CFD temperature results using the proposed methodology for detailed inspection of 6-cell and 16-cell circuit-CFD models are reported.

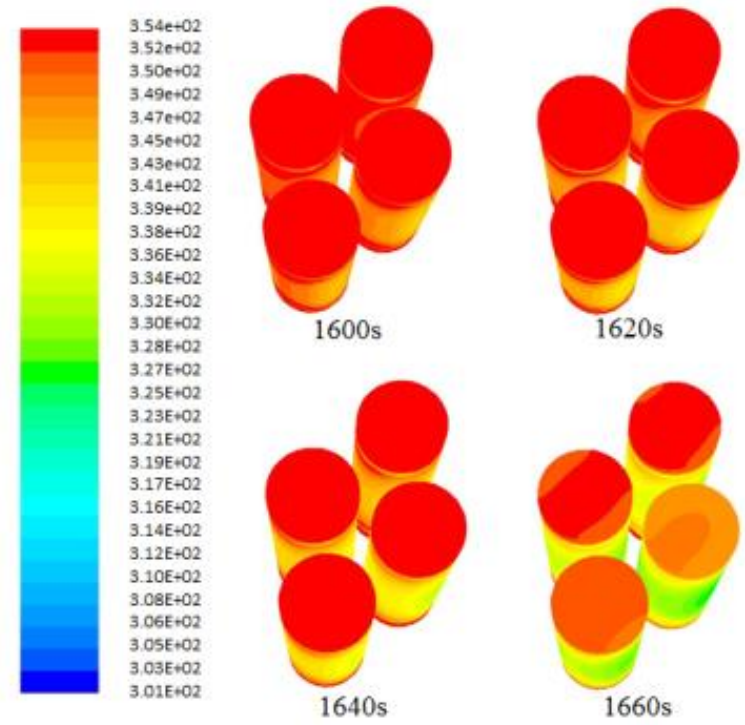

Figure 2.12: Temperature distribution results from the 4-cell circuit-CFD model. The temperature distribution is recorded during Load 3 discharging, and it is presented at 1600, 1620, 1640, and 1660 s.

2.4. More CFD Results and Scalability of the Proposed Circuit-CFD Model

This section presents a 6-cell and a 16-cell battery model. The 6-cell circuit-CFD model is shown in Figure 2.13. The 6 single cells are connected in series electrically. The cell dimension is same as the single cell model and the 6 cells are arranged in similar fashion as the 4-cell model spatially. The temperature distributions on the cross-section of the 3D CFD model at 8 different instants of time during a constant resistive load discharge process are shown in Figure 2.14. The

electrical terminal results are omitted here because they are similar to those in Figure 2.11, and we will focus on the CFD nature of the proposed model in this section.

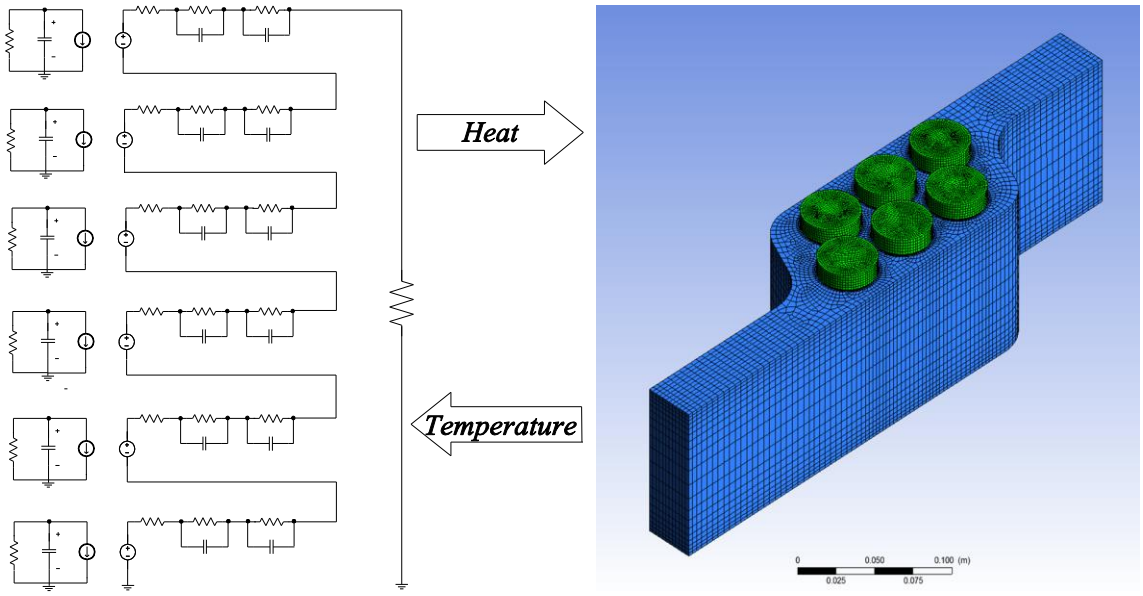

Figure 2.13: 6-cell circuit-CFD model.

Initially in the discharging process, the battery cells heat up relatively quickly in 750 s and reach their first temperature peaks as shown in Figure 2.14(a) - 2.14(c). Subsequently, there is an extended period of time from 750 s to 4500 s where the temperature decreases slowly as shown in Figure 2.14(d) - 2.14(f). Observe that there is a non-uniform temperature distribution in the battery pack when the temperature is undergoing a slow temperature decline. Towards the end of the discharge process, a sudden temperature ramp-up occurs from 5300 s to 5700 s as shown in Figure 2.14(g) – 2.14(h). Cells exhibit different temperatures at different rates due to the unique

location of each cell in the battery pack. The proposed circuit-CFD model holistically predicts temperature distributions at various time instants within the physical geometry.

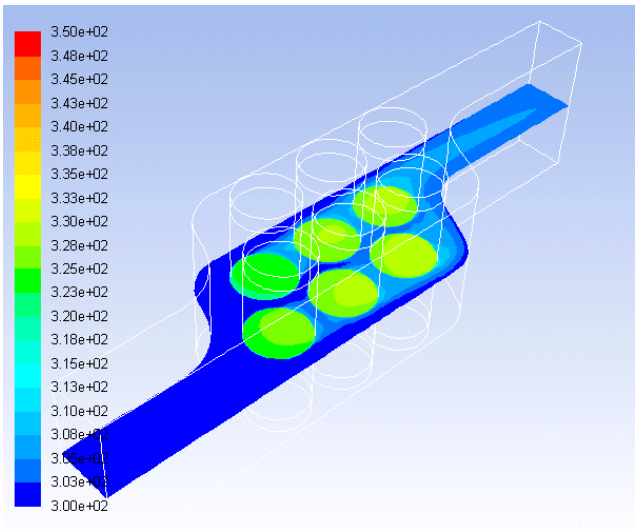

(a) At 50 s. The discharging process starts here.

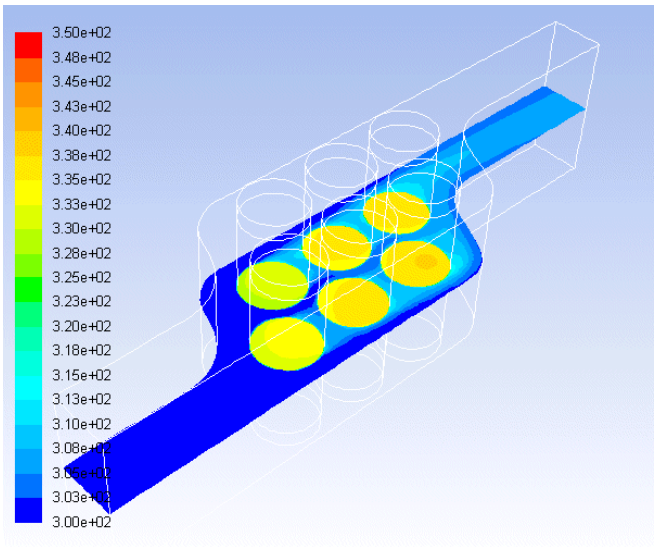

(b) At 150 s. The temperature starts to increase.

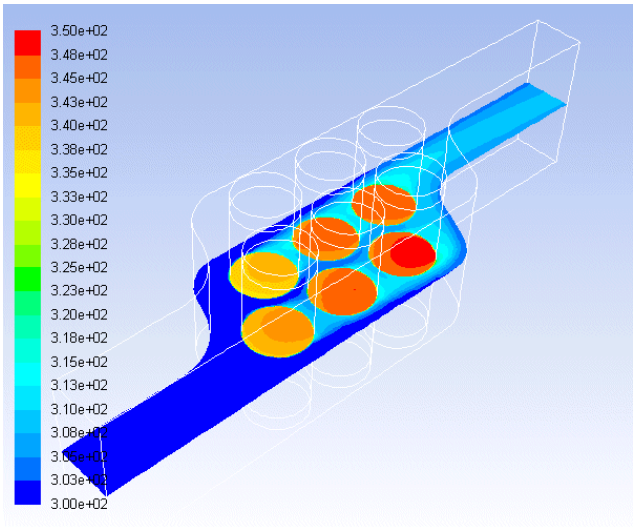

(c) At 750 s. The temperature starts to increase rapidly to its first peak value.

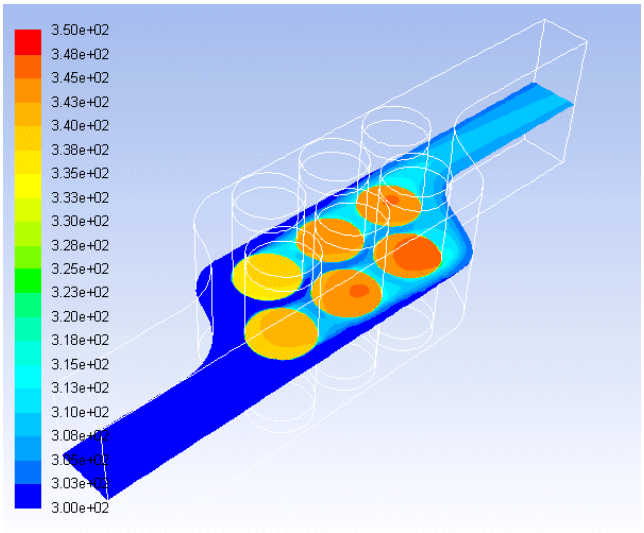

(d) At 2000 s. The temperature starts to decrease.

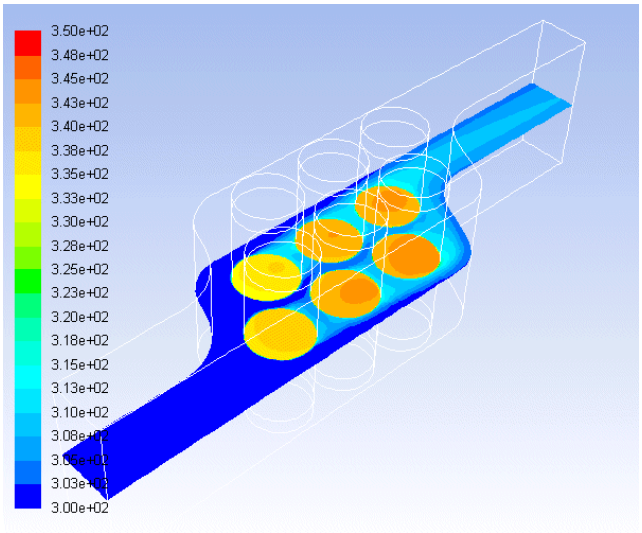

(e) At 3500 s. The temperature continues to decrease slowly.

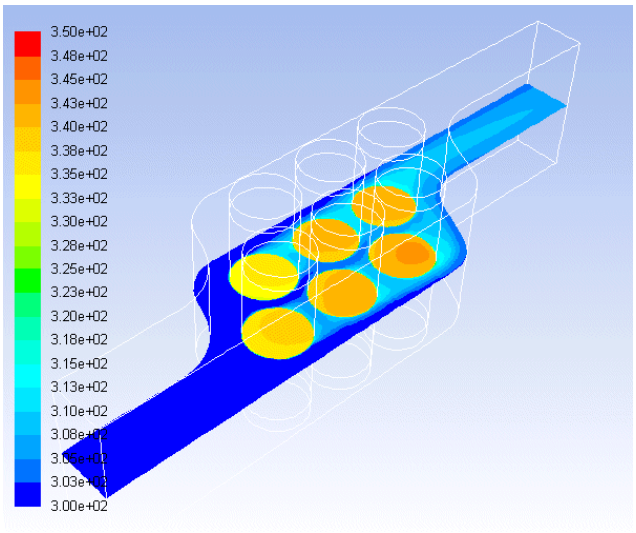

(f) At 4500 s. The temperature continues to decrease slowly.

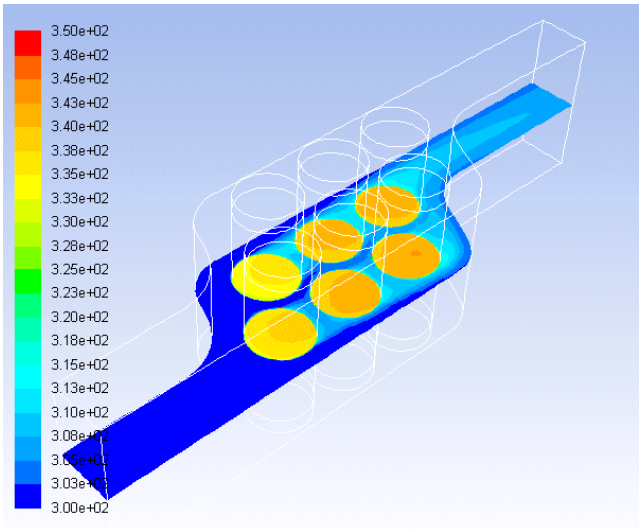

(g) At 5300 s. The temperature starts to increase again.

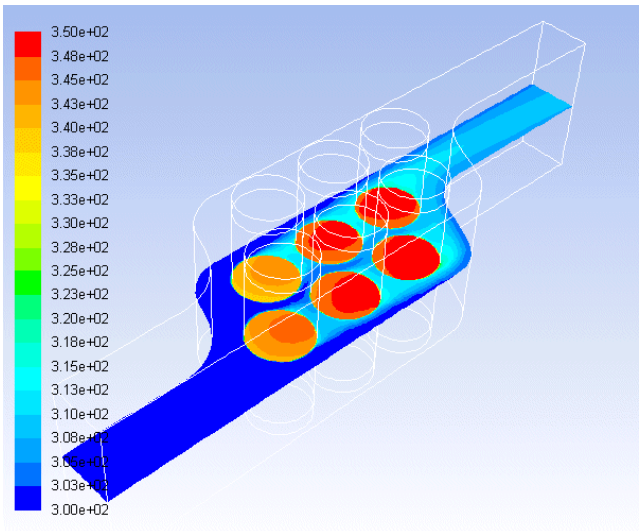

(h) At 5700 s. The temperature starts to increase rapidly to its highest temperature, which is very close to the end of the discharging process.

Figure 2.14: The temperature contour on the cross section of the 6-cell battery model at 8 time instances during a discharging process.

As far as the scalability is concerned, the proposed model can also be used to study battery packs with any larger numbers of cells, the only limiting factor is the availability of the computer

hardware. Also, the computation time of the proposed model is dictated by the CFD model because it is a field solver and it has many more unknowns than the circuit model, the circuit model will not have much overhead in addition to the CFD standalone model solving time while providing a dynamic heat generation mechanism. As an example, Figure 2.15 shows the circuit-CFD model of a 16 battery cell model. The cells have similar dimensions as that in Figure 2.5 and Figure 2.9. The temperature distribution at a time instant during the constant current discharge process is shown in Figure 2.16. The cells as indicated by the graphic identify the thermal distribution that is of concern to engineering application. The circuit-CFD methodology of analysis has made this possible.

In summary, the proposed circuit-CFD methodology is scalable and can provide detailed temperature distribution for any number of cells while taking into account the dynamic heat generation aspect of the battery cells.

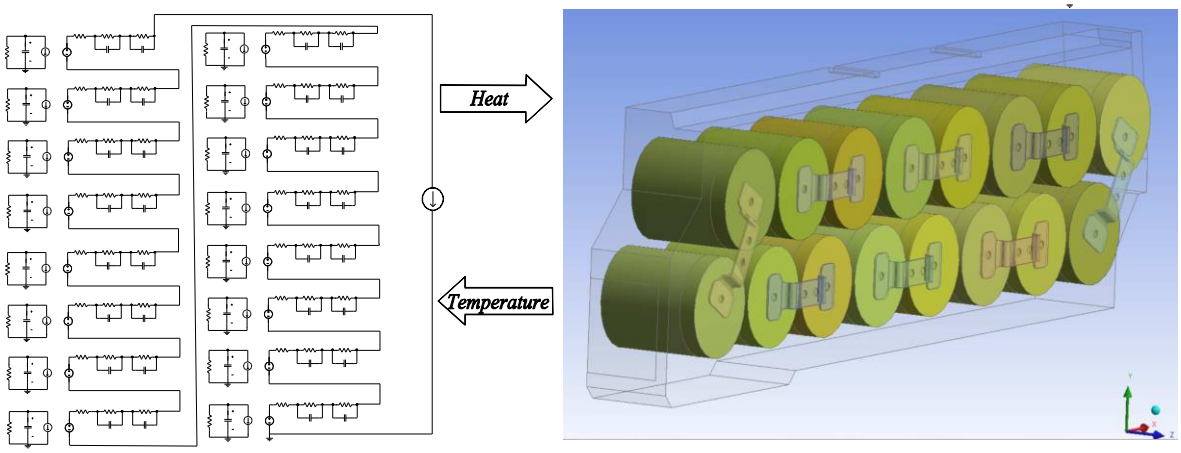

Figure 2.15: 16-cell circuit-CFD model.

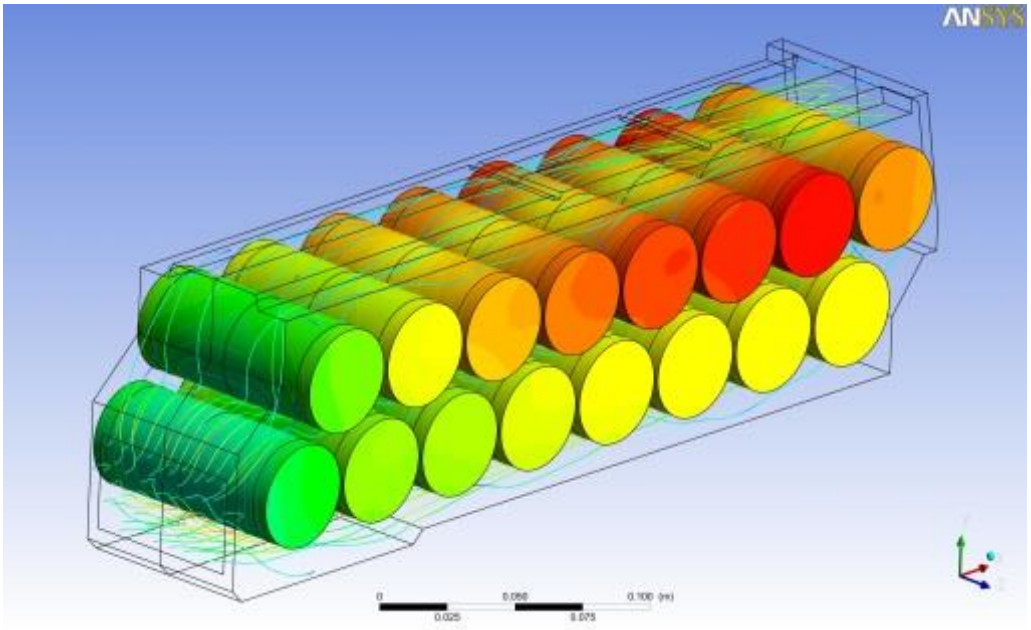

Figure. 2.16: Temperature distribution of the 16-cell circuit-CFD model.

2.5. Summary

In conclusion, a novel circuit-CFD methodology of analysis has been proposed for HEV/EV battery thermal management design. The model consists of a heat generating electrical circuit model and a CFD model predicts temperature distribution. The functionality of the analysis provides temperature distribution of the battery while having an accurate runtime heat generation mechanism taken into account which is a function of temperature. The analysis can be used to predict electrical terminal performance but most importantly the temperature distribution that are due to various battery geometries, materials, current loadings, and cooling conditions. Implementation, simulation results and validation have been provided for the 4-cell battery model under 3 current loading conditions. Finally, a 6-cell and a 16-cell battery models have

been presented to show the flexibility and scalability of the proposed methodology for implementation in engineering design and development.

CHAPTER 3: LINEAR TIME INVARIANT THERMAL MODEL

3.1. Background

There have been many battery models emerged for electrical/hybrid vehicles. There are in general two types of battery models, electrochemistry models [125]-[127] and system level electrical circuit models [128]-[130]. The electrochemistry models are known to be the most accurate models because they describe the electro-chemistry process. On the other hand, electrical circuit models are very poplar choices for system level simulation due to ease of use. They are built of R and C components. The battery circuit models are capable of predicting state-of-charge, I-V characteristics, and dynamic behavior of a battery. If the impact of temperature on battery performance is considered, the electrical modes can be further divided into 2 groups. Isothermal battery models [128] are for low power application whose thermal effect is negligible. On the other hand, for high power applications such as electrical/hybrid vehicles, we use thermal network models [129]-[130] coupling with battery electrical models to take into account temperature impact on battery performance. Thermal capacitance and thermal resistance are used in thermal network models. The number of thermal resistances and capacitances are usually quite large to get accurate results, which makes the model too complex to calibrate. If the number of components is reduced such that each battery cell has only one thermal node [129], the model could easily lose accuracy.

In this part of the work, we propose a new thermal model using Foster network. Foster network also uses resistances and capacitors to represent the transfer function of the thermal system but they do not have the same physical meaning as those in the traditional thermal

network. The way that the resistors and capacitors are connected and how their values are extracted are different from traditional thermal network models. The resistors and capacitors in thermal network models are arranged according to the actual arrangement of the battery cells, and their values are extracted respective to its governing physics or lab testing. On the other hand, the component arrangement of the Foster network is the same once the Foster network order is chosen, in spite of the battery's physical arrangement. The values of the components in the Foster network are obtained by curving the steps responses of the battery thermal systems. The step responses can be collected either from measurement or by using CFD models under linear and time invariant assumptions. To create an accurate traditional thermal network model, the engineer needs to have both in-depth knowledge of the thermal system on hand and good engineering judgment. The Foster network takes systematic approach instead. We will show that a Foster network model can give identical results as the CFD model or testing would if the system is under linear and time invariant assumptions. The simulation time of the Foster network is comparable to that of the thermal network, which is orders of magnitude faster than CFD field simulation. In electronics cooling applications [131]-[132] the Foster network approach has been used for some time, nevertheless this is the first time we introduce it to battery cooling applications.

3.2. Battery Thermal LTI Representation

The battery pack can be considered as a system. A system is an entity that takes inputs and generates outputs [133]. The inputs signals are functions of time in this application. For battery application, the heats dissipated in the battery cells is the inputs, and the temperatures at specific locations the outputs.

If a system is linear and time invariant (LTI), the system will possess two interesting characters. Firstly, its impulse response can completely describe the system itself. For a single input single output system, its output response can be obtained by convolving the input with the impulse response when the system is initially at rest [134]. Secondly, two systems are identical if their impulse responses are identical. According to the second character, we can describe a LTI thermal system using a LTI Foster network, if their impulses or step responses are identical. To obtain the thermal responses such as temperatures of the battery system, we can solve the Foster network of the system using the circuit simulator, which are ordinary differential equations, instead of the partial differential equations. For simplicity, we will study a single battery cell system. Then a six and a sixteen battery cells modules will be presented to demonstrate the application of the method on more complex systems.

3.3. Foster Network Model for Single Battery Cell

In this section, we will discuss a one cell battery system that has only one input and one output. Figure 3.1 illustrates the CFD model of the system. The model has one pressure outlet and one flow inlet. The middle of the domain is the battery cell. This is a standard conjugate heat transfer problem where the convection heat transfer takes away the heat generated by the battery cell.

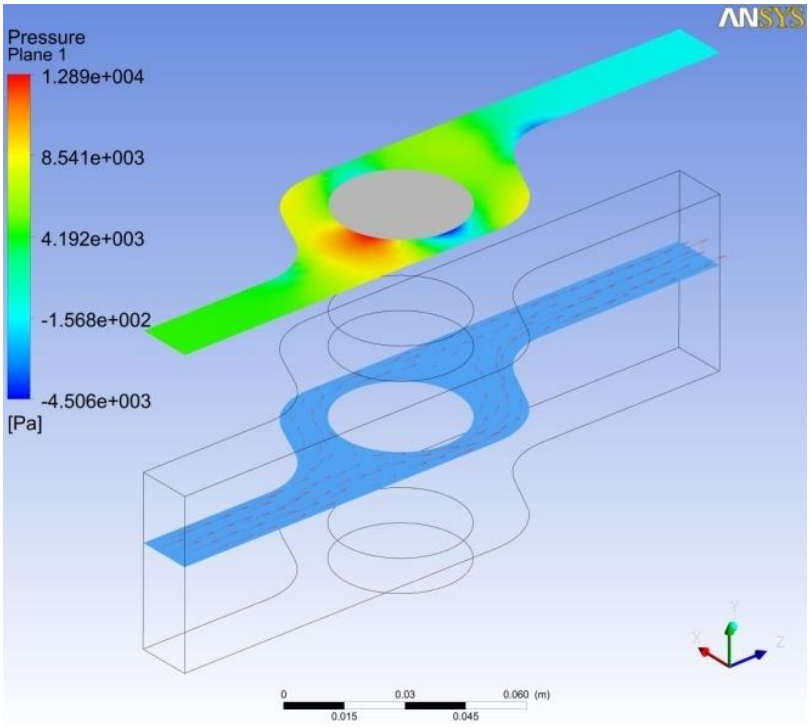

Figure 3.1: Single cell battery cooling system.

The time varying power consumed in the battery cell is the input and the time varying volumetric average temperature cell is the output. Under the assumptions of constant flow rate, constant specific heat, constant density, constant transport properties, and linear boundary conditions, the system can be considered as a LTI system. Examples of linear boundary conditions are temperature and heat flux boundary conditions. Example of non-linear boundary condition is radiation boundary. Constant density and properties are good assumptions for water cooling and forced air cooling battery thermal systems in a narrow range of temperature variation. We will present a benchmark comparing the results from a Foster network and a non-linear CFD model of the same battery module. The results will ensure the Foster network has good accuracy

and practical value. Radiation can be ignored under the assumption of narrow temperature range and furthermore, constant pump speed can realize frozen velocity fields.

The battery thermal system is an LTI system under these assumptions above. Therefore it can be characterized by its impulse response, which in this case is the history of temperature rise of the battery cell given it is excited by a unit heat source at time equals zero. In our study, we obtain the impulse response from CFD simulation, but it can also come from lab testing. Figure 3.2 shows an impulse response of the system.

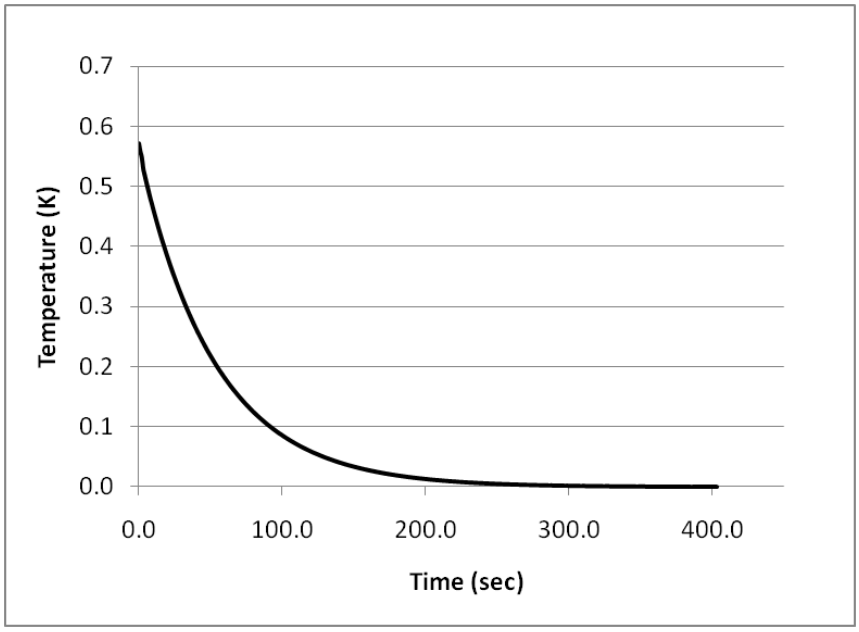

Figure 3.2: A typical impulse response curve.

According to linear system theory, the system output can be obtained by convolving the impulse response with the transient input, the convolution equation is given as (3.1), and the output is the volume average temperature of the battery cell in our study.

$$y(t) = \int_0^t x(\tau)h(t-\tau)d\tau \tag{3.1}$$

where *x* is the input which is a time domain power dissipated, y is the output temperature, and *h* is the impulse response of the system. The convolution is usually written as:

$$y(t) = x(t) * h(t) \tag{3.2}$$

The temperature history under some arbitrary input using CFD and convolution are compared in Figure 3.3. The excellent agreement proves that impulse response completely characterizes the thermal system. Convolution method can reduce the simulation time in order of magnitude compared to the CFD method.

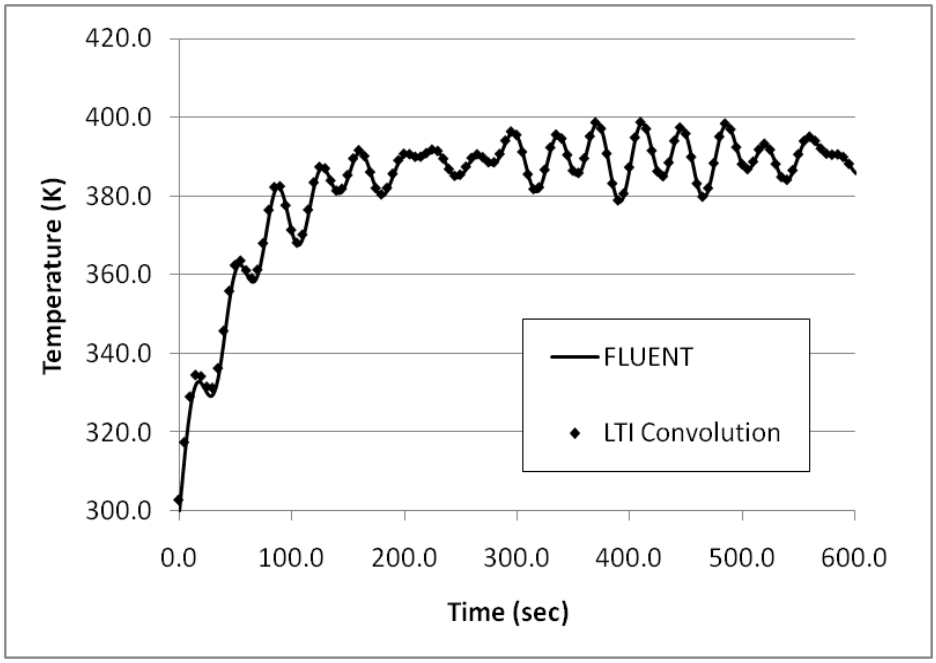

Figure 3.3: Comparison between CFD and convolution results

To generate temperature output of the thermal system from an arbitrary waveform input, the convolution method above is much faster than CFD calculation. However, when the system has multiple outputs and inputs, it is not convenient. Instead, obtaining a LTI model to represent the thermal network appears to be a better approach. A Foster network is one kind of LTI models, which is accurate, fast, and can be co-simulated with an electrical battery circuit model.

A Foster network is a LTI electrical circuit network, if it has the same step response as the thermal system, then it can represent the thermal system. Its parameters can be curve-fitted by using step responses. In this approach, we enforce the Foster network to have the same step response of the battery thermal system. Non-linear least squares method can be used to perform the fitting task. Figure 3.4 shows a typical Foster network. The number of RC pairs can be changes, as well as the RC values.

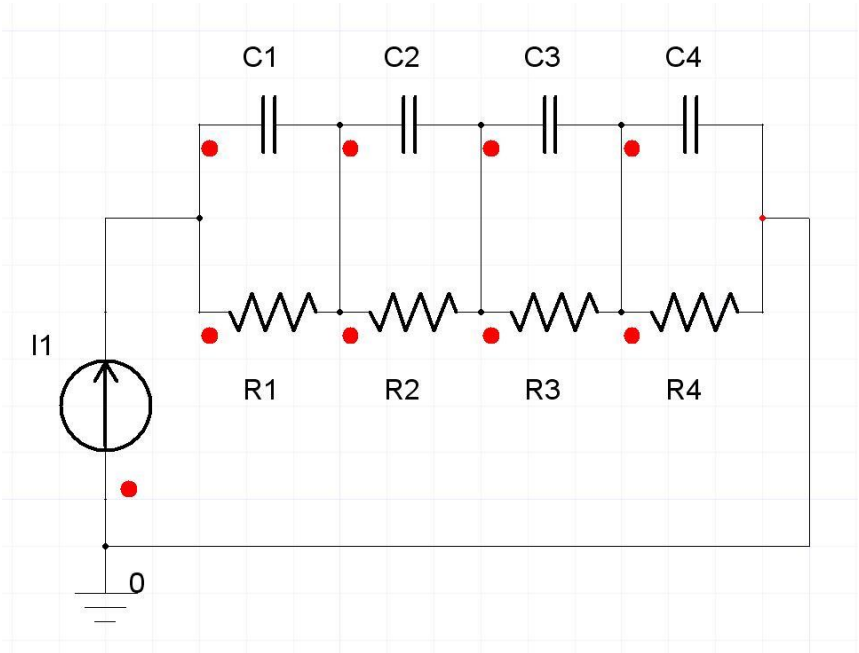

Figure 3.4: A typical Foster network.

In Figure 3.4, the current source is the time varying heat dissipation, and the voltage across the current source is the predicted temperature. Figure 3.5 compares the results between Foster network and CFD of a sin wave heat loss input. The agreement in results shows that the Foster network is an accurate representation of the battery thermal network.

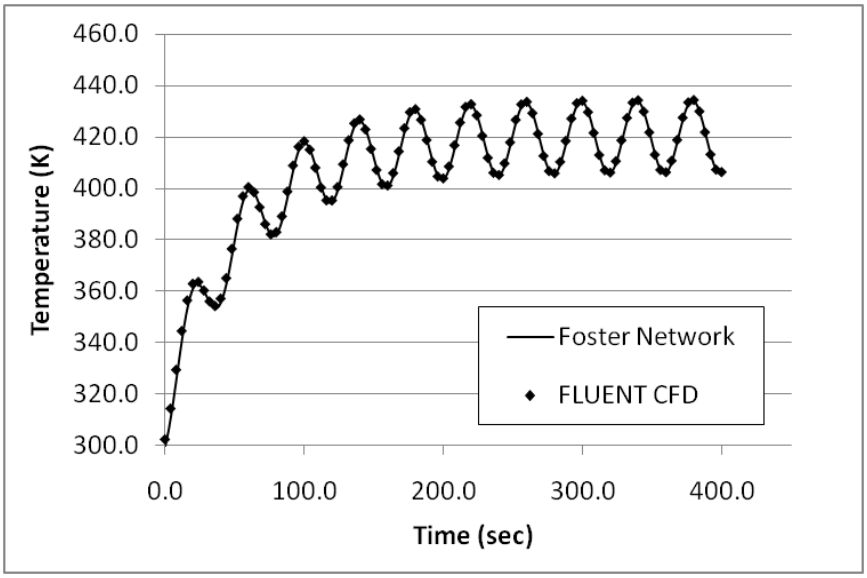

Figure 3.5: Comparison between CFD and Foster network results

In a thermal system that has more than one heating elements, we can have both self-heating as well as cross-heating phenomena. The self-heating step response can be fitted easily. On the other hand, the fitting of cross heating needs additional mathematical manipulation. This is because of the different natures of the self and cross heating responses. Figure 3.6 and Figure 3.7 show the typical self and cross heating step responses, respectively. The self-heating curve has positive slope at the start of the curve and its shape is similar to first order RC response.

However the cross-heating's slope starts at zero, which makes sense because the heat generated from one cell takes time to reach the second cell. The step output of a Foster network is given by the following equation:

$$V = I \cdot \sum_{i=1}^{m} R_i \cdot \left(1 - e^{-t/\tau_i} \right) \tag{3.3}$$

, where the number of RC pairs is m, and Ri and τi can be found by using curve fitting. The Foster network does not allow slope equals to zero therefore it cannot model the cross-heating curves. If we allow for negative values for *R* in the curve fitting, we can fit the curve very well with Foster network. Negative R is correct mathematically, but it will not work in circuit simulation because there is no negative resistance. To overcome this problem, *R* will be limited to positive values only, then we subtract the voltage of R, which would otherwise have been negative to fit the cross heating. This way, the *R* values are positive which is understandable by the circuit solver, but they will have negative voltage contribution.

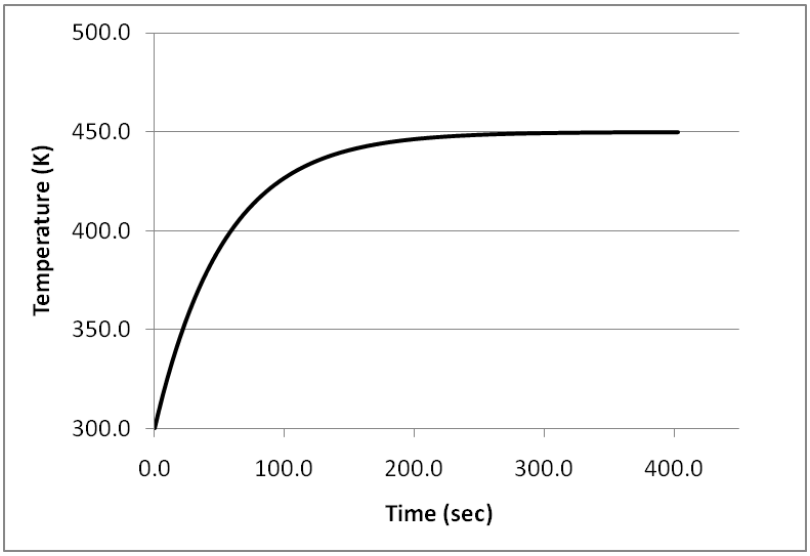

Figure 3.6: A typical step response of self-heating

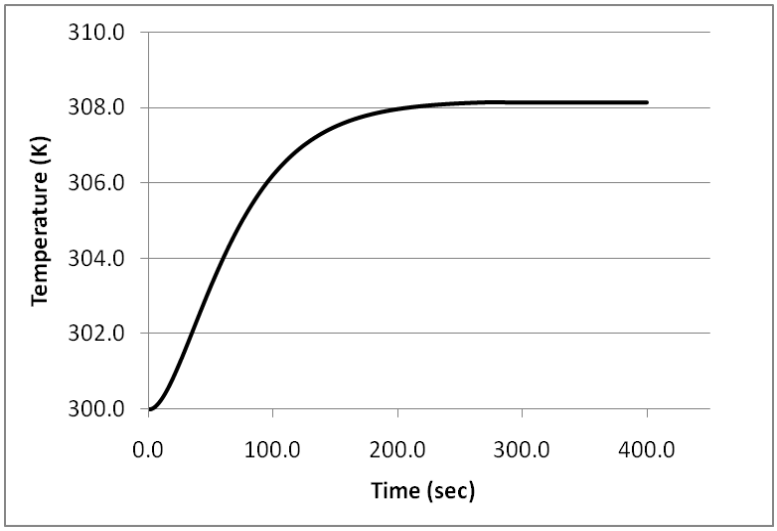

Figure 3.7: A typical step response of cross-heating

3.4. Foster Network for A Battery Module

If the thermal system is linear, then we can use superposition to predict thermal performance of a multiple cell battery module. For example, the temperature of a battery cell can

be calculated by summing up the contributions from all the battery cells in the system. Equation (3.4) is the mathematical representation of superposition.

$$\begin{bmatrix} y_1(t) \\ y_2(t) \\ \vdots \\ y_n(t) \end{bmatrix} = \begin{bmatrix} h_{11}(t) & h_{12}(t) & \cdots & h_{1m}(t) \\ h_{21}(t) & h_{22}(t) & \cdots & h_{2m}(t) \\ \vdots & \vdots & \ddots & \vdots \\ h_{n1}(t) & h_{n2}(t) & \cdots & h_{nm}(t) \end{bmatrix} * \begin{bmatrix} x_1(t) \\ x_2(t) \\ \vdots \\ x_m(t) \end{bmatrix} \tag{3.4}$$

where y_i is the output, the average temperature at the ith battery cell; x_i is the input, the power consumed at the ith battery cell; * here denotes convolution as shown in equation (3.2); h_{ij} in the represents the impulse response of the jth heat input on the ith temperature output. The impulse response matrix completely represents the system mathematically. To determine h_{ij}, we excite one cell at a time. For instance, battery cell number j is excited only with a unit impulse, then the temperature rise as a function of time at battery cell number i becomes the h_{ij}. We can define the inputs and output anywhere of interest in the thermal system. In other word, the matrix in (3.4) is not necessary a square matrix.

As discussed before, Foster network method can be more user friendly than the convolution method. To create a Foster network for a MIMO (Multiple Input and Multiple Output) system, we actually need to create Foster network matrix. In Figure 3.8, we have a six cell battery module where we define 6 power inputs and 6 temperature outputs. Therefore the Foster network matrix contains 36 elements, where each element is a Foster network theoretically. In practice, the effect of some cross heating element is very small therefore can be ignored, which results in matrix size smaller than 36. The Foster network for this battery system is shown in Figure 3.9. The Foster network of each matrix element is represented by two sets of *RCs*. And some cross heating elements are neglected because their effects are negligible. Figure

3.10 compares CFD and Foster network results. Foster network and CFD give the same solution. The solution time of Foster network is less than 30 second and CFD takes 30 minutes on the same computer.

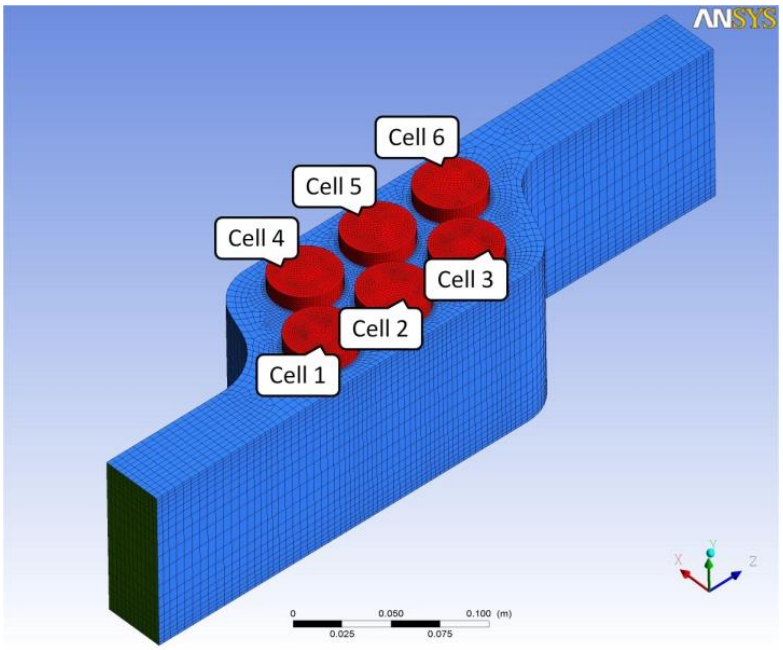

Figure 3.8: A battery system with six battery cells.

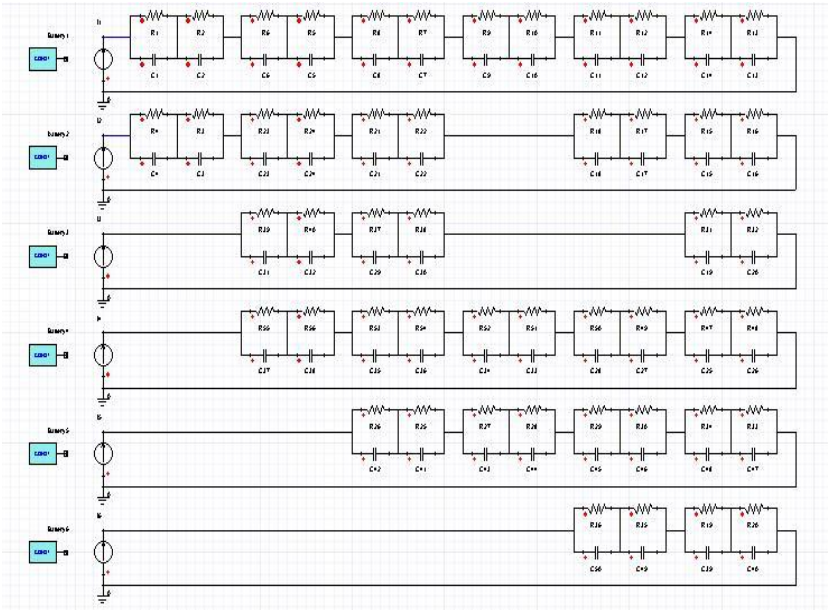

Figure 3.9: Foster network model for the six cell system

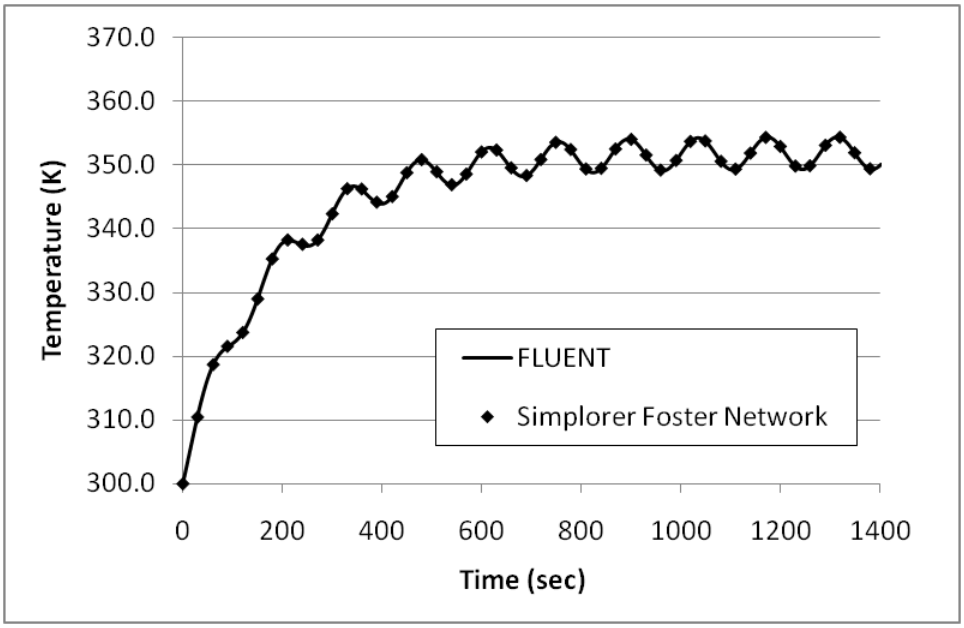

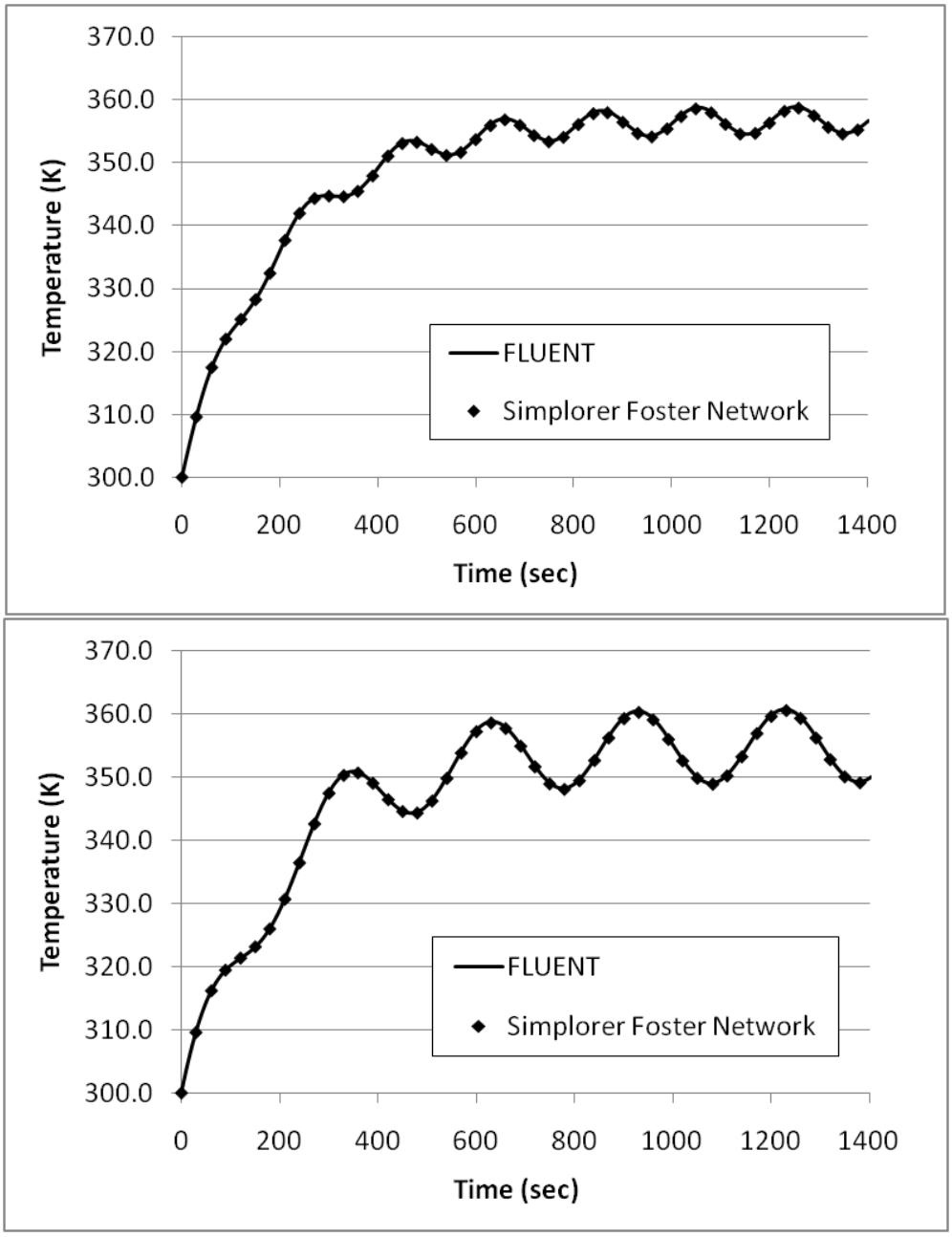

Figure 3.10: Comparison between FLUENT results and Foster network results for three battery cells

CFD model has to be a LTI system in order to have the same results as the Foster network. However, the real battery thermal systems are highly nonlinear. Next we will see how well the Foster network model compares to the non-linear CFD model. We use the same six cell

battery module. A Foster network model is generated from the step responses of the LTI CFD model. Another CFD model of the same battery module that considers nonlinear effects such as ideal gas law for density, temperature dependent material properties under the same flow rate is generated. The results of the Foster network and the realistic CFD model are compared in Figure 3.11 under sinusoidal heat generation. We choose to show the temperature of cell one, the other cells have similarly results. The difference in results is 2% due to non-linearities when the temperature rise of the cell is about 90 K. 2% is within good engineering acceptance because usually battery cells will have a temperature rise less than 90K, which will result in error less than 2%.

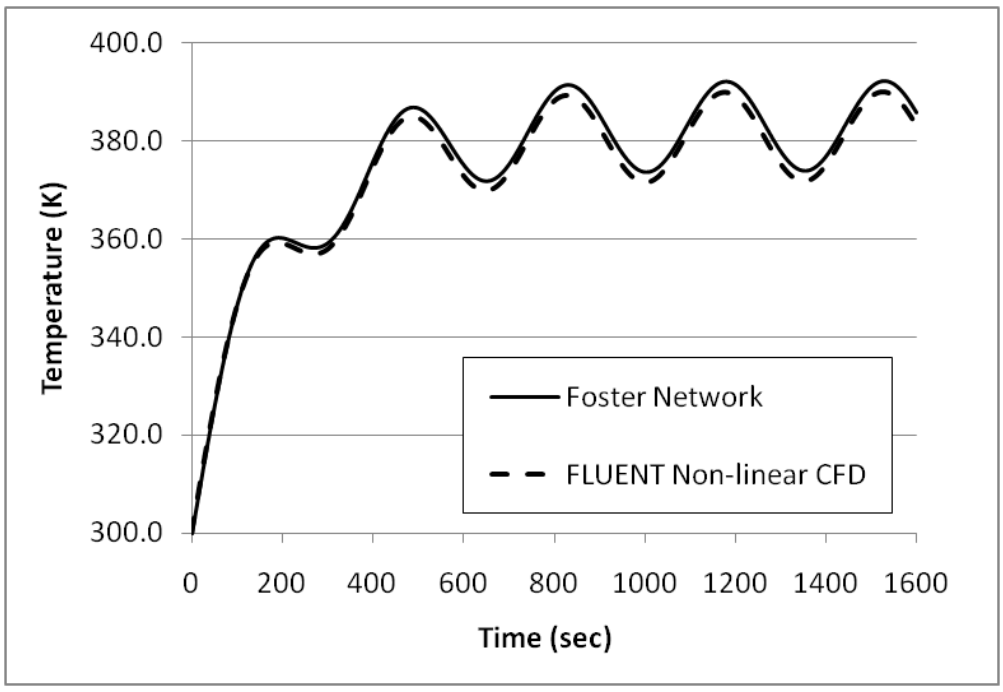

Figure 3.11: Comparison of Foster network model with FLUENT non-linear CFD model.

3.5. Complete battery circuit model

We can use battery circuit model to study the electrical performance of the battery module. A popular battery circuit model [128] is shown in Figure 3.12. A thermal model can be co-simulated with the battery circuit model to consider the thermal effect. Thermal network model is usually coupled with the battery circuit model. Thermal network model is usually not accurate because the number of components of the model is small for simplicity, and the heat transfer coefficient is assumed to be constant for each battery cell. In order to improve the accuracy of the thermal network model, large number of components are needed therefore makes it difficult to calibrate. The thermal network model can be replaced by Foster network model without losing accuracy. One advantage of thermal network over the Foster network is that it does not require the battery thermal system to be LTI system. Nevertheless, we have shown that for battery application, Foster network is accurate results even considering non-linear effects.

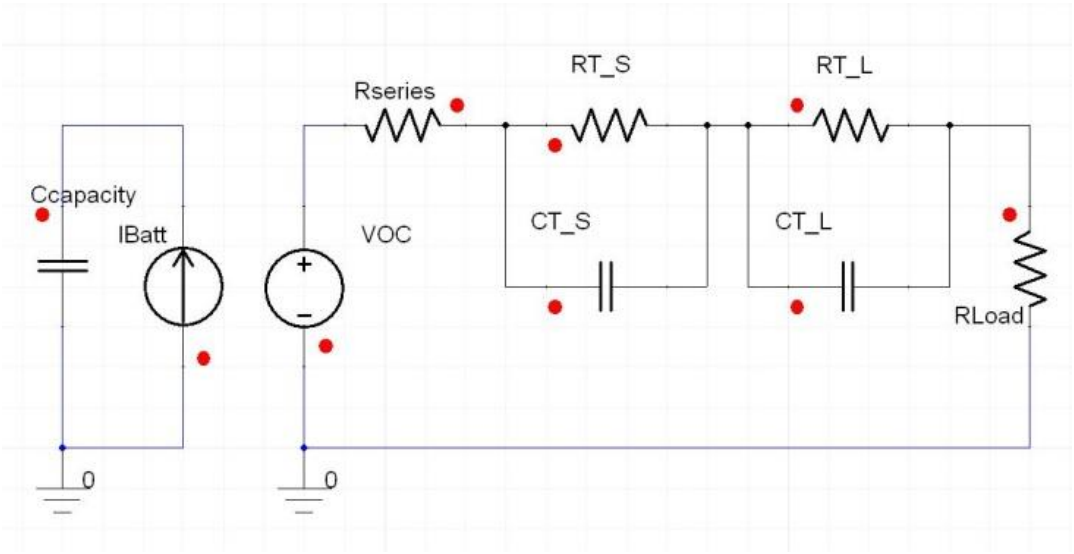

Figure 3.12: An electrical circuit model for a battery cell

3.6. Summary

We can represent battery thermal system by Foster network or Foster network matrix if the thermal system is LTI system. The simulation results of Foster network model are in excellent agreement with CFD model. However, the simulation time of Foster network is order of magnitude shorter than CFD simulation time. To obtain a Foster network, we need to use the CFD model of the battery or experimental testing on the actual battery module to collect the step responses, and the model is created by using least squares curve fitting method. The Foster network can also be coupled with battery circuit model in place of the traditional thermal network without losing accuracy. We have also shown that the Foster network results is within 2% difference comparing to the nonlinear CFD model results with a 90K temperature increase.

CHAPTER 4: MULTI-PHYSICS INTERIOR PERMANENT MOTOR MODELING

4.1. Background

PM electric machine are very important in high performance drive systems such as hybrid and electrical vehicles, and etc. During normal operations, irreversible demagnetization can occur in magnets due to temperature rise and various loading conditions [135]. However, these effects have not been presented in the form of IPM's electric machine quantities in literature. Therefore, we are motivated to investigate the performance of an IPM electric machine due the temperature rise and loading variations. We propose to use 3d time stepping electromagnetic FEA integrated with the temperature dependent permanent magnet model proposed in [136] to study the phenomena. Finally, the non-uniform temperature distribution of the magnets is taken into account by using CFD solution.

Figure 4.1 (a) shows the N5211 rare earth magnet material from Dexter Magnetic Technologies [137], which provides the intrinsic and normal BH curves from -20 ^{o}C to 80 ^{o}C. These curves can be approximated according to the thermal dependent magnet model in (4.1) and (4.2). α and β are the coefficients of the model and they are either provided by the manufacturer or computed by standard curve fitting technique. B_r is remanence, H_{ci} is intrinsic coercivity, T is the magnet temperature, and T_0 is the reference temperature of one intrinsic BH curve. The derived curves are shown in Figure 4.1 (b).

$$B_r(T) = B_r(T_0) \cdot [1 + \alpha(T - T_0)] \tag{4.1}$$

$$H_{ci}(T) = H_{ci}(T_0) \cdot [1 + \beta(T - T_0)] \tag{4.2}$$

The derived ones and the original data curves are in good agreement. The BH curves at other temperature can also be calculated from the model. We will discuss the temperature effects on the IPM performance in details in the next section.

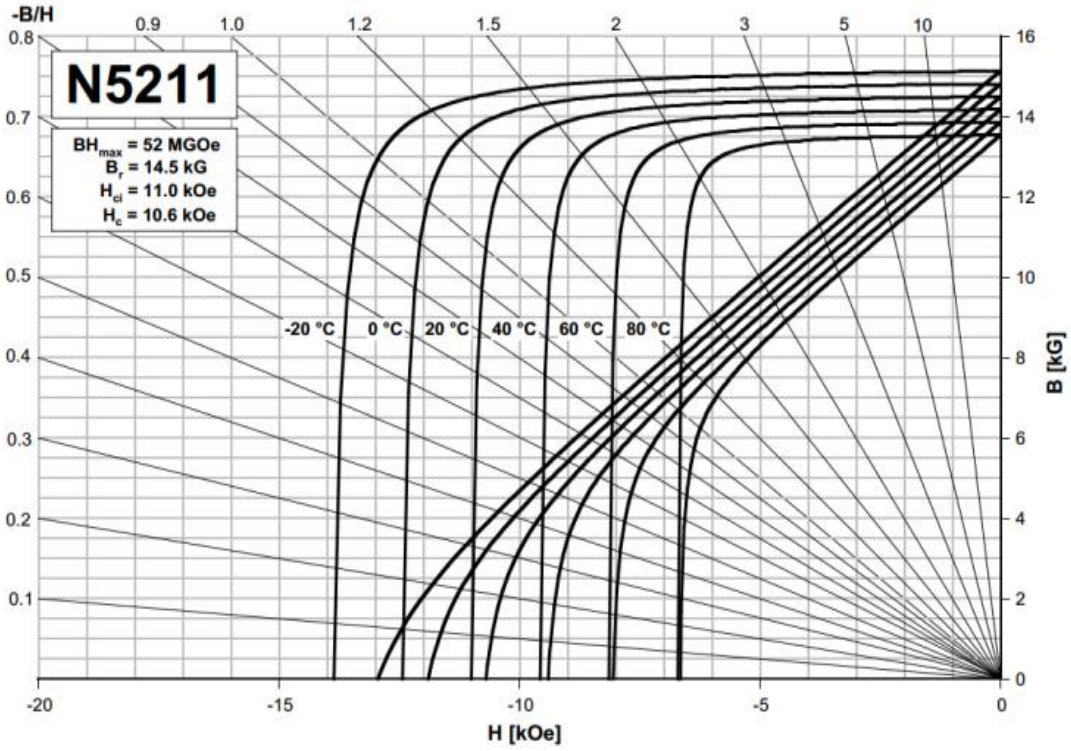

(a) BH curves on N5211 data sheet

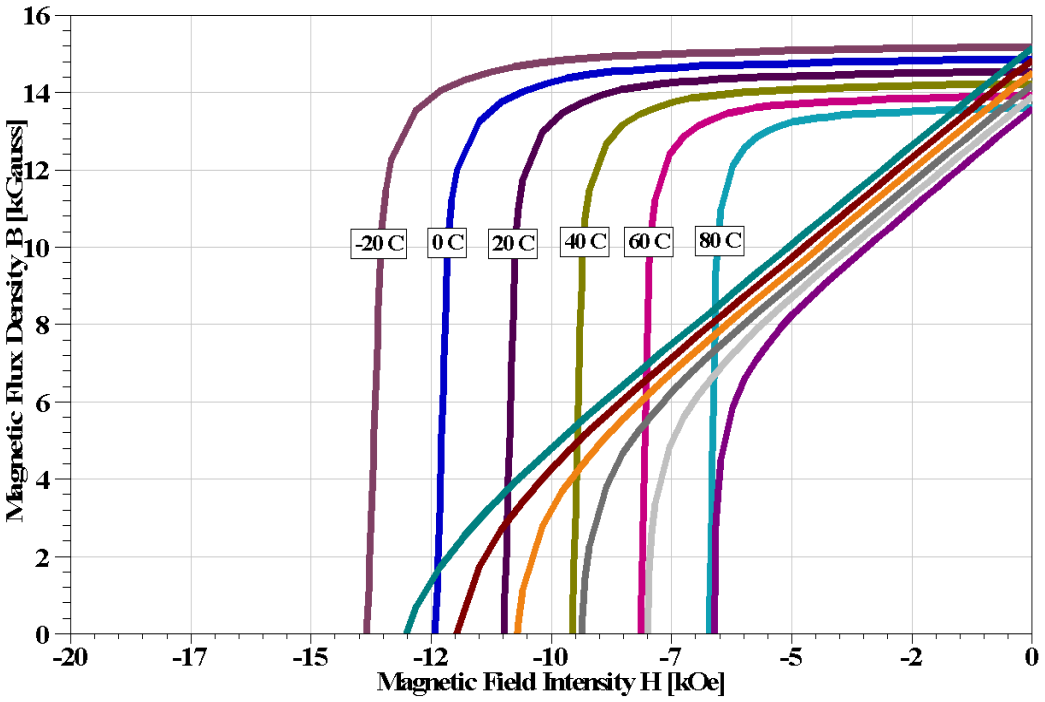

(b) BH curves generated by the temperature dependent magnet model

Figure 4.1: The intrinsic and normal BH curves of rare earth material N5211

4.2. Results and Analysis

The Toyota 2004 Prius IPM motor [138] is used to demonstrate the temperature effects on the magnets as well as the IPM performance. The motor is modeled in ANSYS Maxwell 3D time stepping finite element software. The motor is controlled by three phase balanced currents, we define the control angle as the electrical angle from the d-axis in the rotor reference, the phase peak current is 233 A, and the rotor shaft speed is 3000 rpm. The magnet material used in the model is N5211 and we assume the magnets have uniform temperature distribution for now.

Figure 4.2 shows the torques of the motor at various temperatures when the control angle

is 120 degree. To validate the thermal-dependent magnet model, we obtained torques by using the normal BH curves for 20–80 ^{o}C from Figure 1(a). Then we compare them with the torques by using the thermal-dependent magnet model at the same temperatures, both results are in good agreement and shown as the first 4 curves in Figure 4.2. Notice that there are dots superposed on the curves and they are the solutions using the BH curves of the data sheet. It can be seen that the torque decreases as temperature increases whereas the torque ripple decreases.

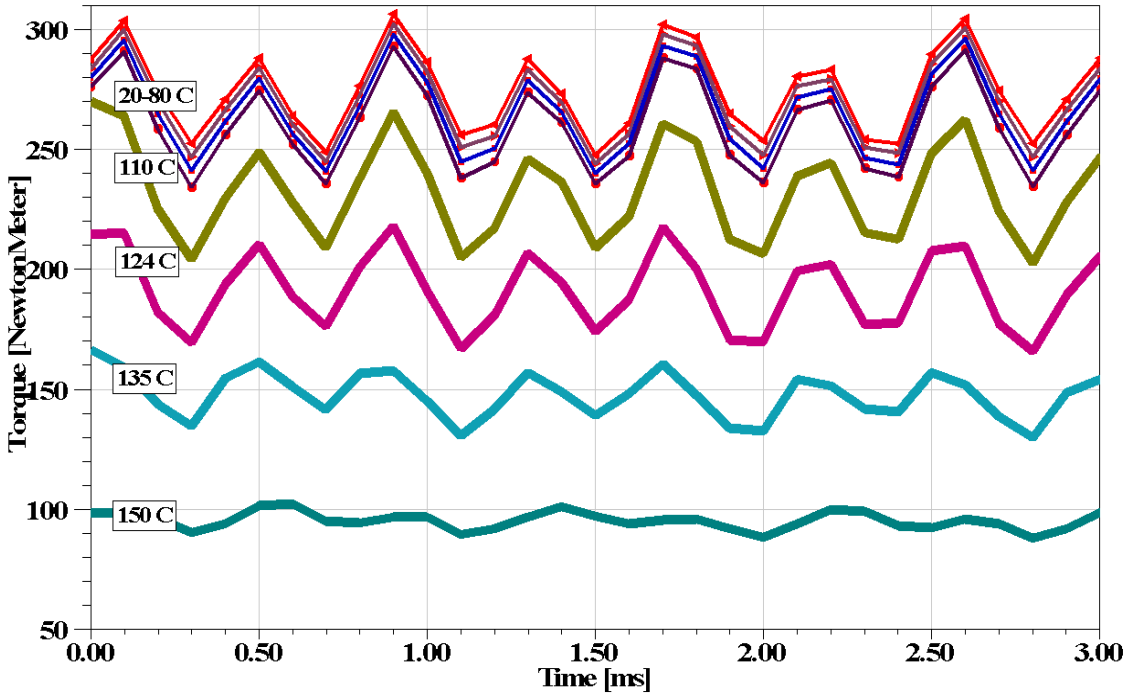

Figure 4.2: Torque vs time at various temperatures.

Figure 4.3 provides the magnetic flux density of the rotor for 20, 120, and 150 ^{o}C, in this case the control angle is 120 degrees. The magnetic flux density B of the magnets as well as the rotor core decreases as the temperature rises. The decrease in magnet flux density means the

magnets are losing its capability of producing flux when operating at the same magnetic field intensity. This is the reason the torque reduces as temperature rises. In addition, decrease in rotor flux density indicates the motor loses its saliency because the d-axis reluctance is reduced. We will look at the saliency in details later on. We will focus on what has occurred in the magnets first.

We then place a measurement point at the center of the magnet on the left, as shown in Figure 4.3(c). The B and H values at the measurement point are plotted on Figure 4.4 at various temperatures. The B and H values of the point are drawn in thicker lines, and the N5211's normal BH curves are drawn in the thinner curves. When the temperature is below 90 ^{o}C, the measurement point operates in the linear region of the BH curves. In the linear region, the demagnetization is reversible. When it is above 90 ^{o}C, the measurement point starts working in the recoil regions, which means irreversible demagnetization has occurred. Also in Figure 4.3(b), the B values at the upper right corners of the magnets are lower than the centers of the magnets. This is because the corners are closer to air in the slots such that the fringing fields in the slots demagnetize the corners first. Therefore the corners of the magnets are more susceptible to demagnetization than the center of the magnet. In other word, if the center of the magnet is under irreversible demagnetization, approximately half of the magnet is also under irreversible demagnetization.

The time average torque of the IPM is plotted against temperature in Figure 4.5 when the control angle is 60, 90 and 120 degrees. The three curves decrease at the same constant slope from 20 to 90 ^{o}C. However, the 120 degree curve decreases faster than the other two curves

when it is above 90 ^{o}C. Also our analysis earlier indicated that at 90 ^{o}C a significant part of the magnet is under irreversible demagnetization at 120 degree control angle. Therefore, the torque vs temperature curve in Figure 4.5 decreases at an increasing slope indicates significant irreversible demagnetization has occurred in the magnet. Notice irreversible demagnetization occurs at 90 ^{o}C for the 120 degree curve, however it will occur above 120 ^{o}C for the 60 and 90 degree curves. IPM machines are known to operate at control angle greater than 90 degree to gain additional reluctance torque [139], which also makes the IPM more susceptible to irreversible demagnetization at lower temperature.

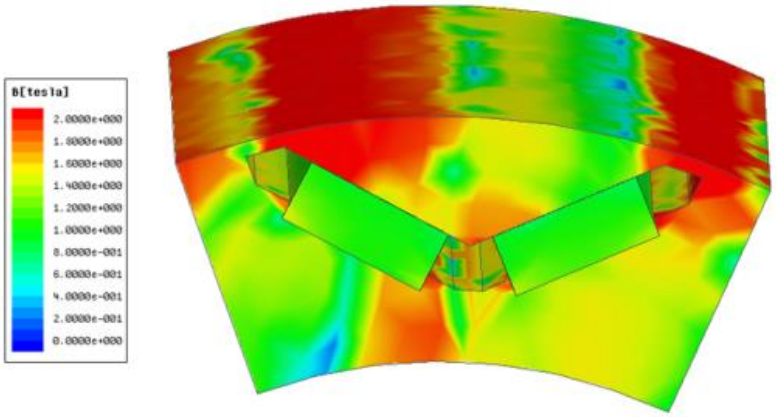

(a) 20 ^{o}C

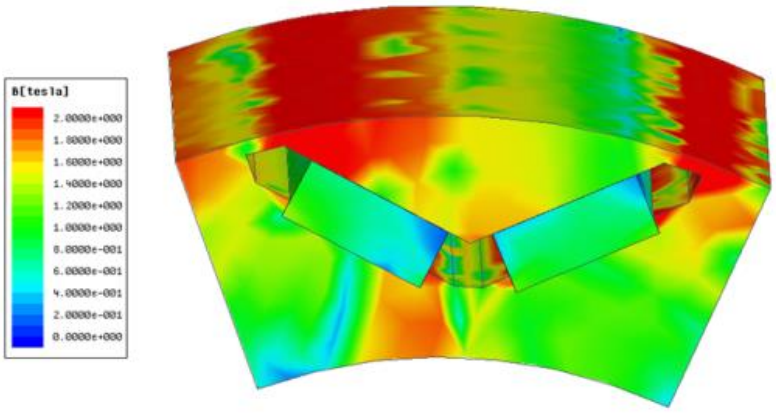

(b) 120 ^{o}C

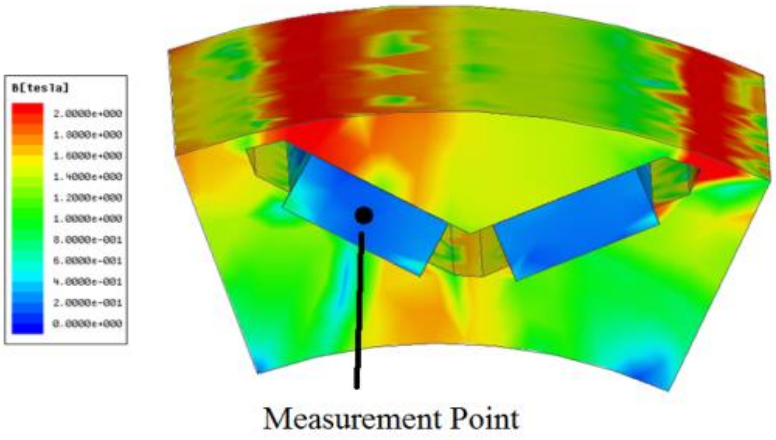

(c) 150 ^{o}C

Figure 4.3: Rotor magnetic flux density at 20, 120, and 150 ^{o}C.

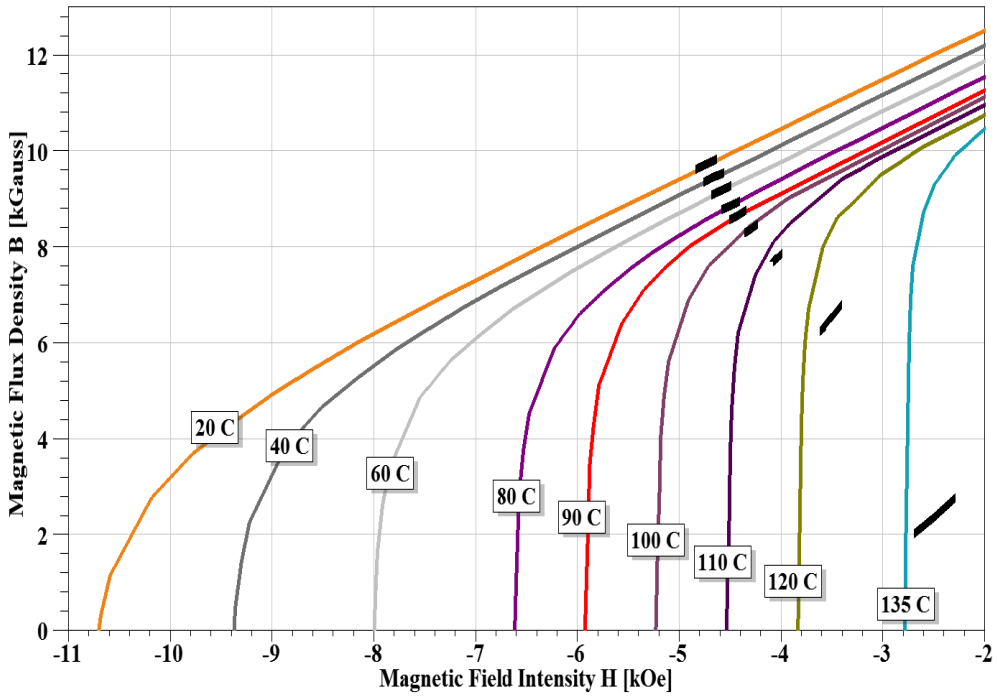

Figure 4.4: Operating points of the measurement point at various temperatures

In addition, when it is above 135 ^{o}C, the 120 degree curve approaches the 90 degree curve. The machine has lost most of its reluctance torque, in other word, its saliency.

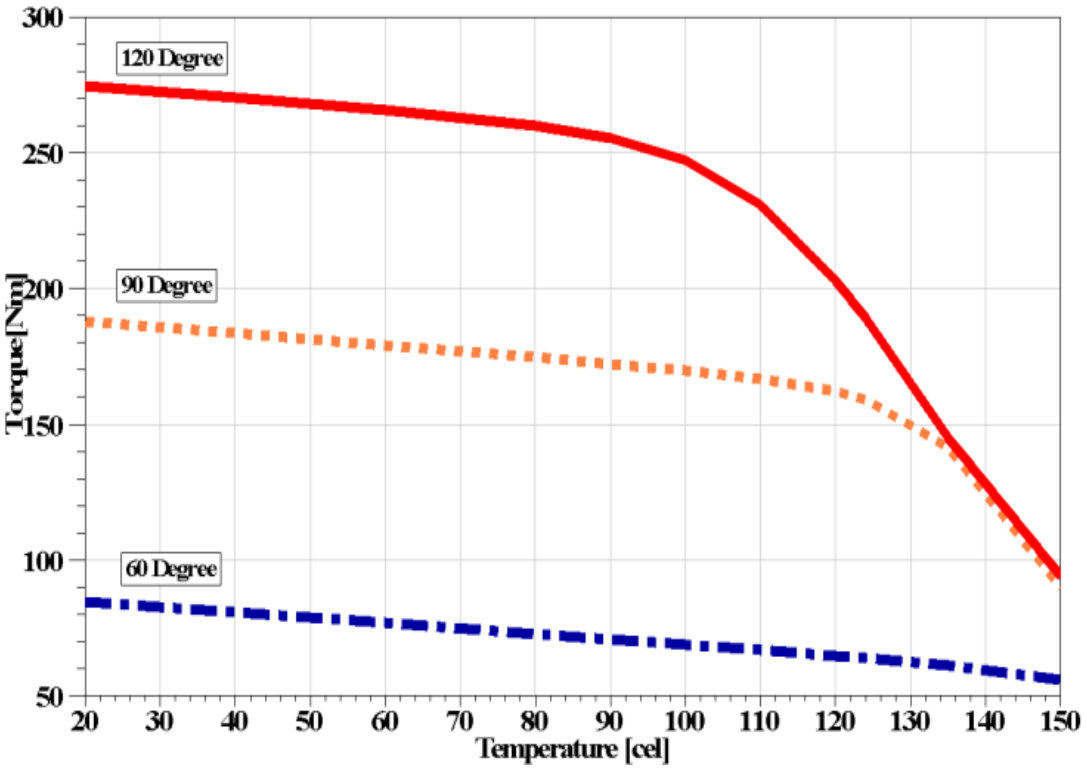

Figure 4.5: Torque v.s. temperature for control angle 120, 90, and 60 degrees

In Figure 4.6, the torque vs control angle is plotted at 20, 120 and 150 ^{o}C. Notice the maximum torque angle varies for each curve. At 20 ^{o}C, the maximum torque angle is 140 degree. At 120 ^{o}C it is 120 degree. Finally at 150 ^{o}C it is 150 degree. The knowledge of the maximum torque angle is very critical for Maximum Torque Per Amp (MTPA) control in the constant torque region.

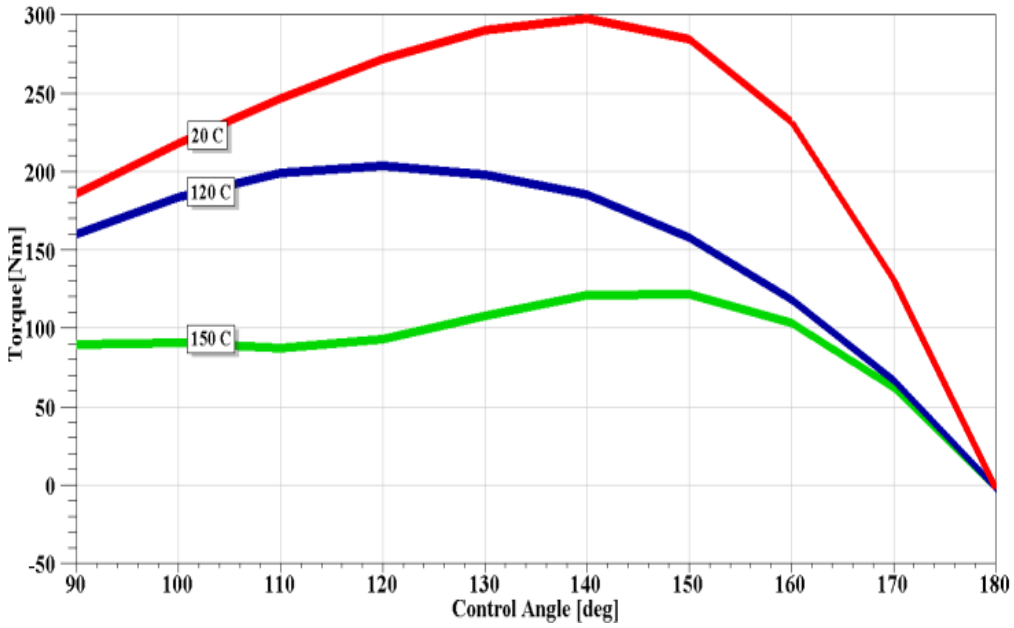

Figure 4.6: Torque vs control angle at 20, 120, and 150 ^{o}C

The current and flux linkage are plotted in Figure 4.7. The current is solid curve whereas the flux linkage is the dotted curve. The flux linkage is moving in phase with the current as temperature rises. This is because the magnet is weakened and the resultant flux is dominated by the armature reaction. Figure 4.8 shows the induced voltage of phase under various temperatures. The induced voltage waveform shifts to the left and increases as temperature rises and it means less voltage will be available in field weakening region at higher temperature.

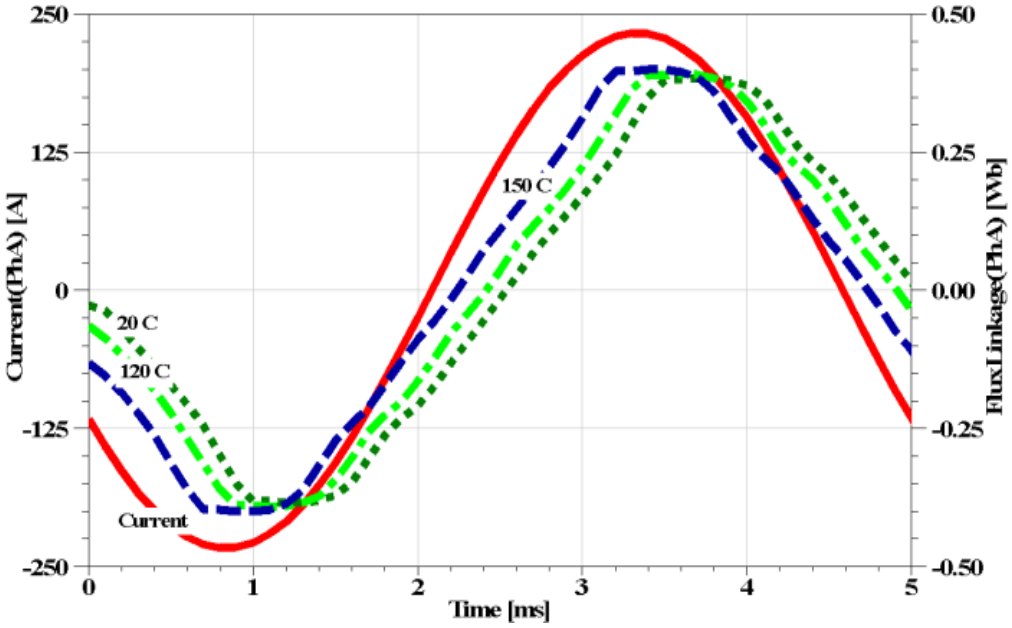

Figure 4.7: Phase A current and flux linkage at 20, 120, and 150 ^{o}C

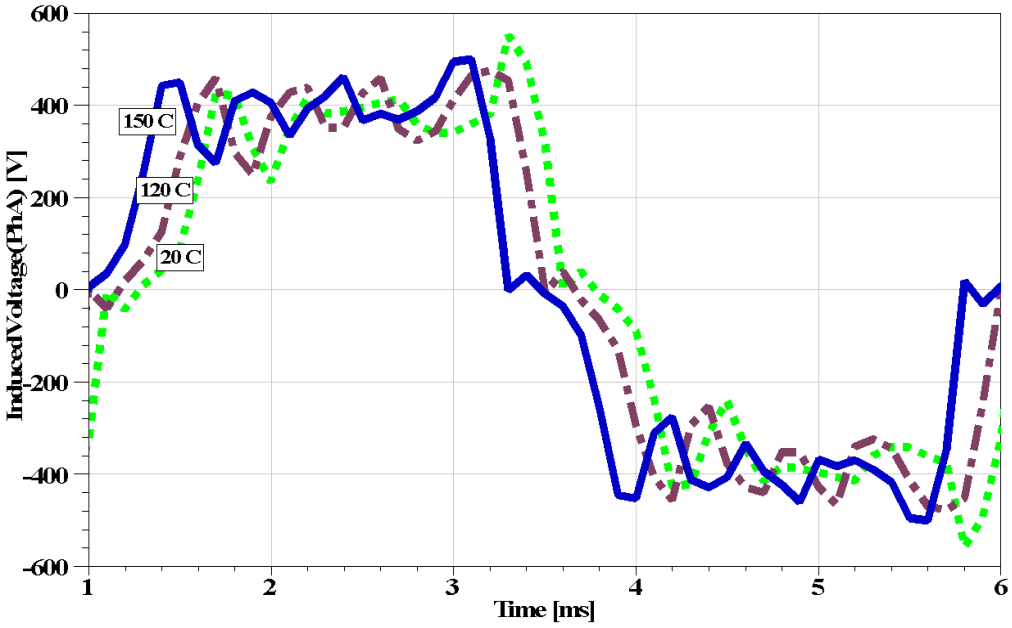

Figure 4.8: Phase A induced voltage when the magnet temperature is 20 ^{o}C, 120 ^{o}C, and 150 ^{o}C

Next, we will investigate the change in IPM's saliency versus temperature. Figure 4.9 shows d-q inductance Ld and Lq, as well as the saliency ratio Lq/Ld, at 120 degree control angle. Ld increases and approaches to Lq as temperature rises. The saliency ratio is closer to 1. These are evidences that the IPM loses its saliency as temperature increases.

In Figure 4.10, the control angle is equal to 90 degree. Ld and Lq are getting closer before 105 ^{o}C and eventually they are equal at 105 ^{o}C. Above 105 ^{o}C, Ld is greater than Lq, and the saliency ratio goes less than 1. This means the motor not only loses it saliency, but also go one step further reversing its saliency - d axis becomes q axis, q axis becomes d axis as temperature increases.

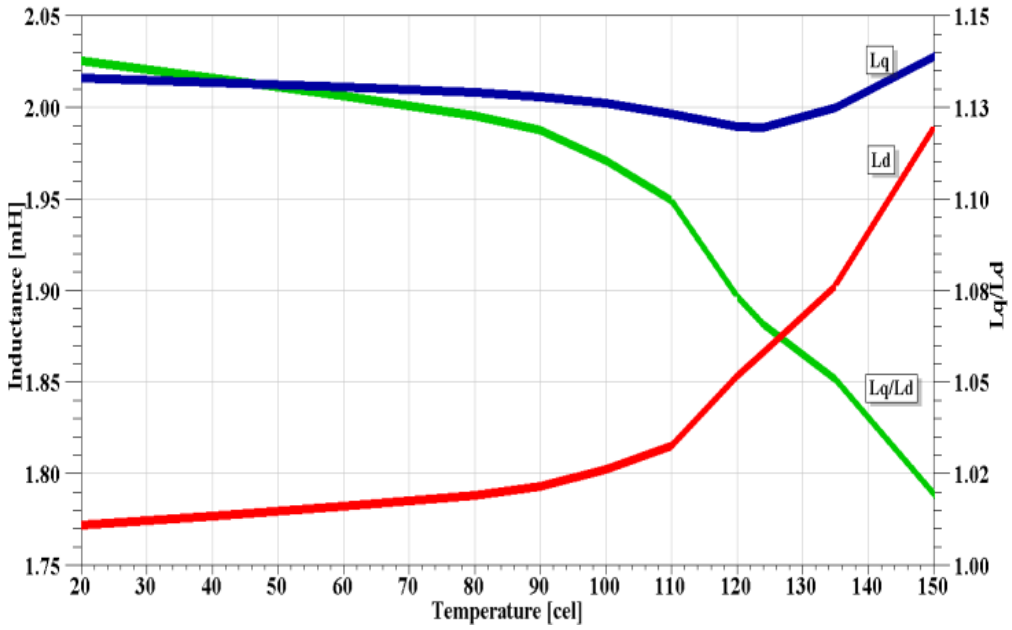

Figure 4.9: Ld, Lq and Lq/Ld vs Temperature at 120 degree control angle

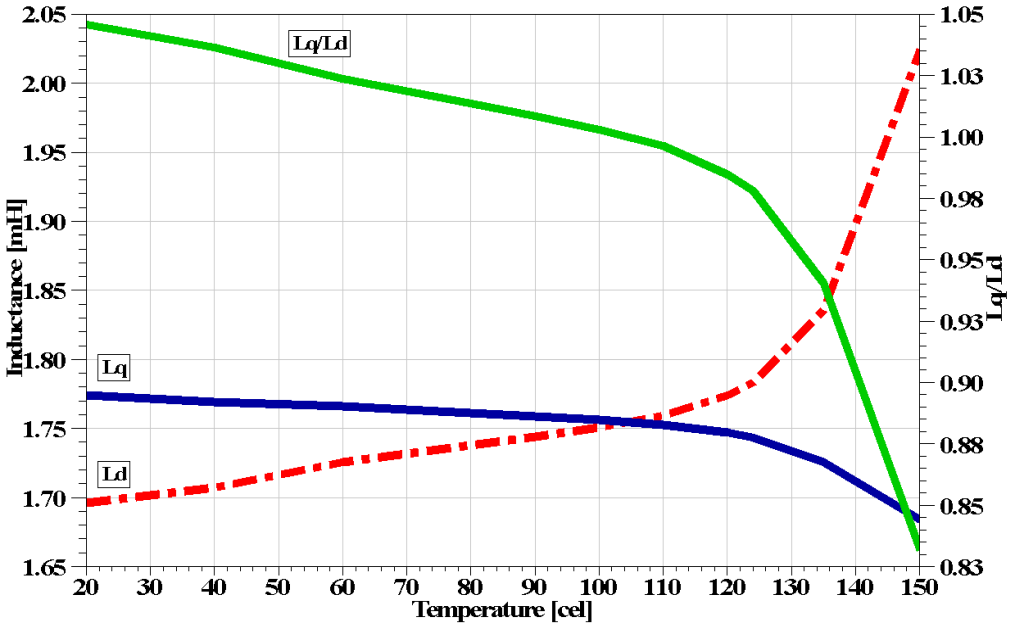

Figure 4.10: Ld, Lq and Lq/Ld vs Temperature at 90 degree control angle

The analysis has been based on the assumption the magnet has a uniform temperature. In real applications, there could be temperature gradient in magnets [140]. To predict the temperature gradient effects on the IPM, we therefore create a CFD model in Fluent. The CFD is coupled to the time stepping electromagnetic 3D FEA. The coupled simulation takes 4-5 iterations to converge. The non-uniform temperature distribution of the entire IPM is shown in Figure 4.11. The temperature gradient on the magnet is shown in Figure 4.12 and its corresponding B vectors are plotted in Figure 4.13.

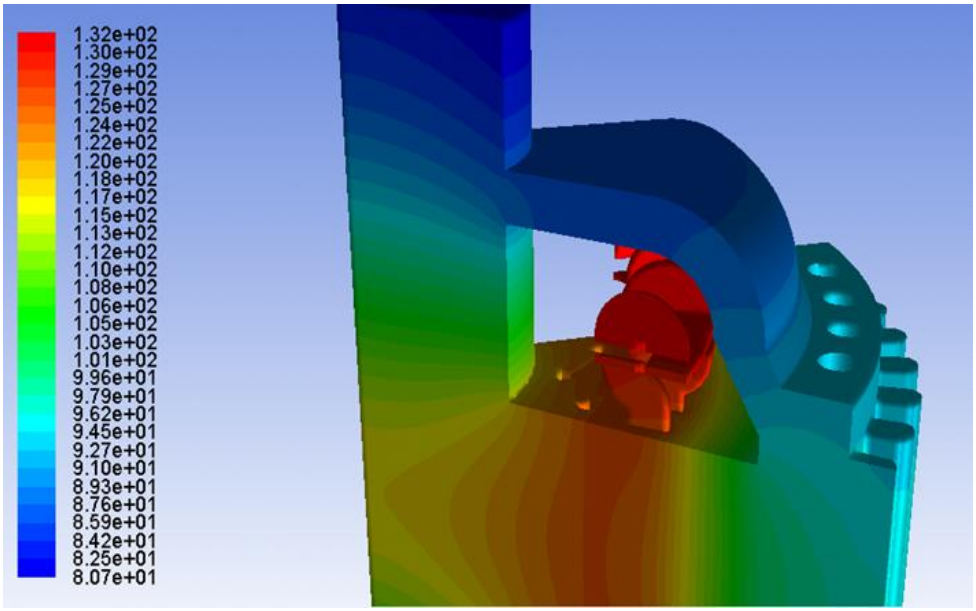

Figure 4.11: Temperature distribution of the IPM motor

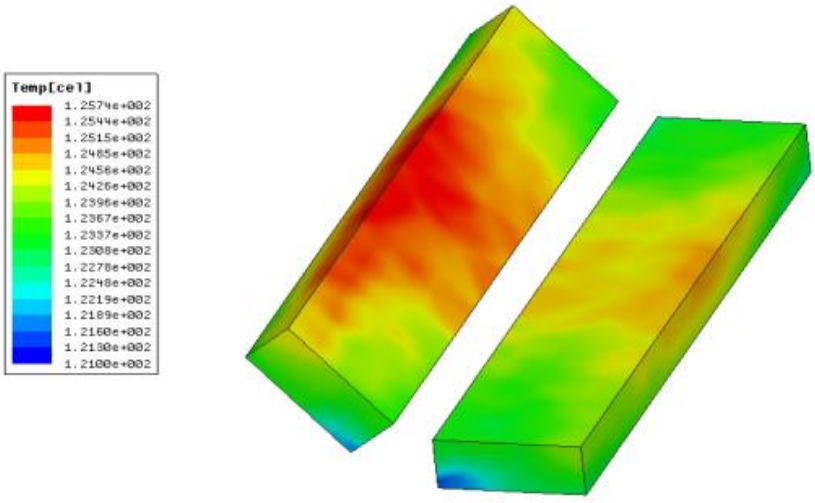

Figure 4.12: Temperature distribution of the magnets

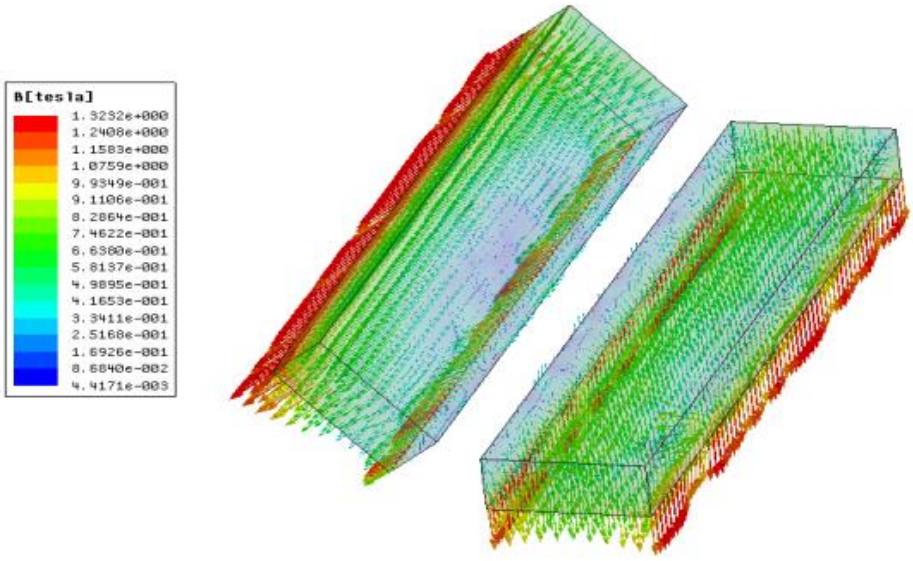

Figure 4.13: Flux density vector of the magnets

Finally, Figure 4.14 gives the comparison of the torque for 20 ^{o}C, 135 ^{o}C and the coupled solution. Notice the difference between the results differ up to 30%. Therefore, obtaining the temperature distribution is necessary to accurately predict the torque of the IPM machine.

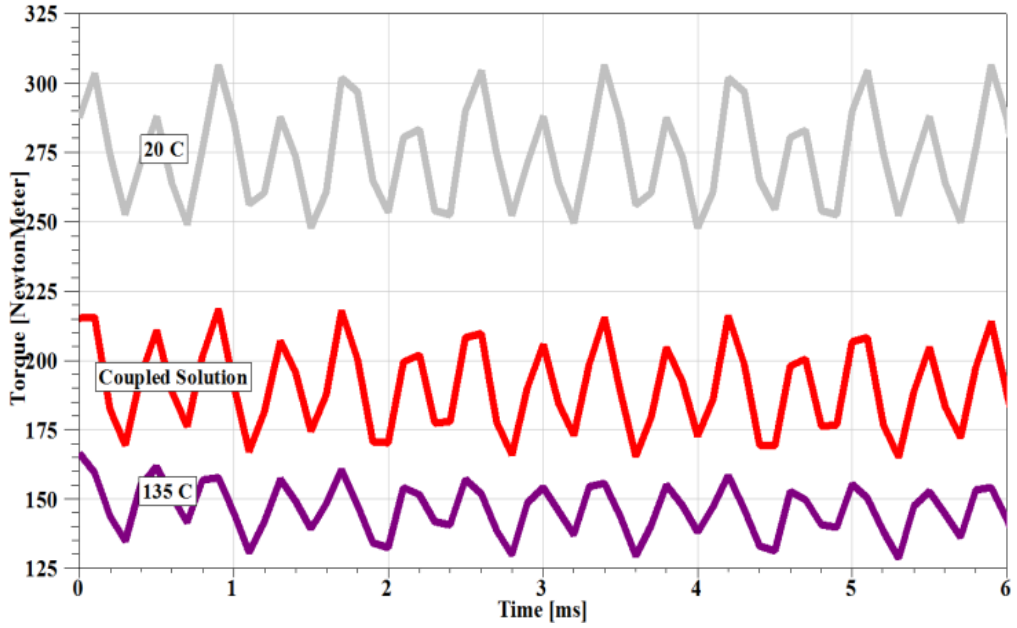

Figure 4.14: Comparison of torques

4.3. Summary

We have shown that the torque of IPM decreases as temperature increases due to reversible and irreversible demagnetization. And when the control angle is greater than 90 degree, the magnets of IPM are more susceptible to irreversible demagnetization due to temperature rise. Also the maximum torque control angle may differ at various temperatures. In addition, the flux linkage and induced voltages increases with temperature. Interestingly, The IPM motor tends to lose its saliency as temperature rises, or even reverse its saliency, depending on the operating control angle. Finally, a non-uniform temperature distribution could change the machine performance significantly. Therefore detailed thermal model is necessary to capture the non-uniform thermal effects on the IPM performance. In conclusion, temperature dependency of the

magnets of the IPM has significant impact to its performance. Therefore it should be studied carefully in any IPM machine design. Our future work is to study the temperature effects on other quantities such as core loss, eddy loss in the magnet, efficiency, and etc.

CHAPTER 5: REDUCED ORDER IPM MODEL CONSIDERING PM TEMPERATURE DEPENDENCY

5.1. Background

IPM motors have been very popular because of high power density and high efficiency characteristics, especial in HEV and EV applications. The operation of the motors is complicated, to study and understand it, the knowledge of the field distribution and material saturation level are required. FEA is the most popular tools to carry out study and design of the IPM. FEA provides detailed field distribution, electrical and magnetic performance of the IPM considering material properties, excitation, and physical dimensions because FEA solves the partial differential Maxwell equations. Therefore, FEA is well suited for IPM designers to design and optimize the machine. However, for system level simulation, the speed of FEA is too slow. For system level simulation, we are concerned about the performance of the entire system rather than just the IPM itself. So it is desirable to have an IPM model that is accurate to capture the main characteristic of physics, but runs at circuit simulation speed. The permanent magnet materials are temperature dependent, which can affect the IPM performance significantly, therefore we are motivated to propose an IPM reduced order model that considers the magnet temperature effect based FEA results. We will validate the proposed model using the FEA results.

5.2. Existing PM Models

The most popular PM model is called the dq model. The dq model is obtained by using the dq theory. The dq theory is a reference frame transformation, after the dq transformation, the sinusoidal inductances of the motor will become constant, the dq fluxes are decoupled mathematically, and dq voltages are only coupled through the speed voltage term. The dq motor equations under balanced excitation are shown as:

$$v_d = R_s i_d + \frac{d\lambda_d}{dt} - \omega_r \lambda_q \tag{5.1}$$

$$v_q = R_s i_q + \frac{d\lambda_q}{dt} + \omega_r \lambda_d \tag{5.2}$$

$$T_e = \frac{3}{2}\frac{P}{2}(\lambda_d i_q - \lambda_q i_d) \tag{5.3}$$

For PM motor, the dq fluxes are:

$$\lambda_d = L_d i_d + \lambda_{PM} \tag{5.4}$$

$$\lambda_q = L_q i_q \tag{5.5}$$

Therefore (5.1) to (5.3) can also be written in terms of the inductances:

$$v_d = R_s i_d + L_d \frac{di_d}{dt} - \omega_r L_q i_q \tag{5.6}$$

$$v_q = R_s i_q + L_q \frac{di_q}{dt} + \omega_r L_d i_d + \omega_r \lambda_{PM} \tag{5.7}$$

$$T_e = \frac{3}{2}\frac{P}{2}\left[\lambda_{PM} i_q + \left(L_d - L_q\right) i_d i_q\right] \tag{5.8}$$

(5.6) to (5.8) together with (5.9) are often used to model PM machines.

$$J\frac{d\omega_m}{dt} = T_e - T_L \tag{5.9}$$

IPM is one special kind of PM machine, so it can also be modeled by these equations. There are in general two types of IPM models and we will introduce them in the following.

5.2.1. Analytical Linear and Non-linear IPM models

Analytical linear IPM model uses the equations (5.6) to (5.9) directly. For IPM, Ld is less than Lq, and they are both constants. So linear model takes into account the saliency of the IPM, but it cannot account for non-linear saturation phenomenon.

Non-linear linear IPM models also use equation (5.6) to (5.9), the Ld and Lq parameters are based on non-linear material BH curve. The model takes into account saliency and non-linear material saturation. However, the non-linear saturation usually is still not accurate due to the dq cross coupling effect, and localized saturation.

5.2.2. IPM Model Based on FEA

The IPM model based on FEA also uses equations (5.6) to (5.9), though it is inductances are calculated from FEA, and the inductances are functions of id and iq:

$$L_d = f(i_d, i_q) \tag{5.10}$$

$$L_q = f(i_d, i_q) \tag{5.11}$$

This phenomenon is known as the cross coupling effect. Figure 5.1 and 5.2 show an example of the FEA Lq and Ld inductances as functions of id and iq. As a result, we can find that the torque is also a function of id and iq in Figure 5.3.

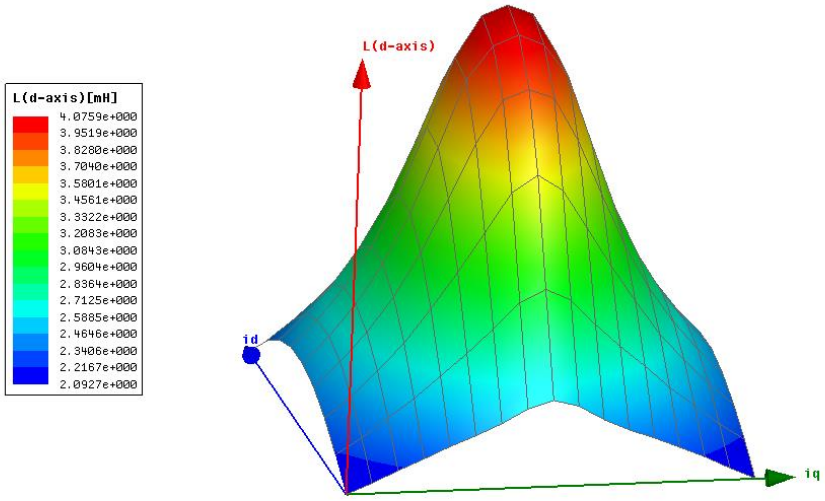

Figure 5.1 Ld is a function of both id and iq

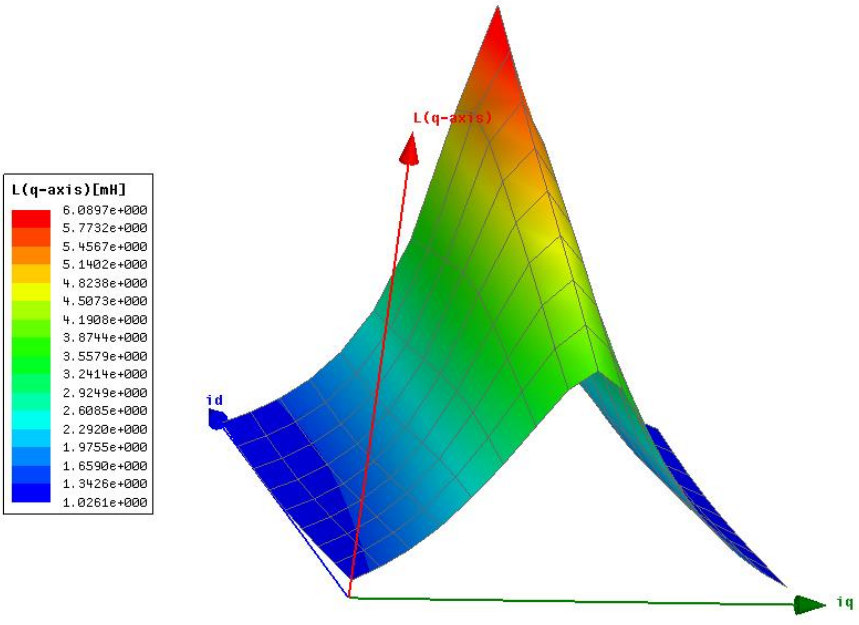

Figure 5.2: Lq is a function of both id and iq

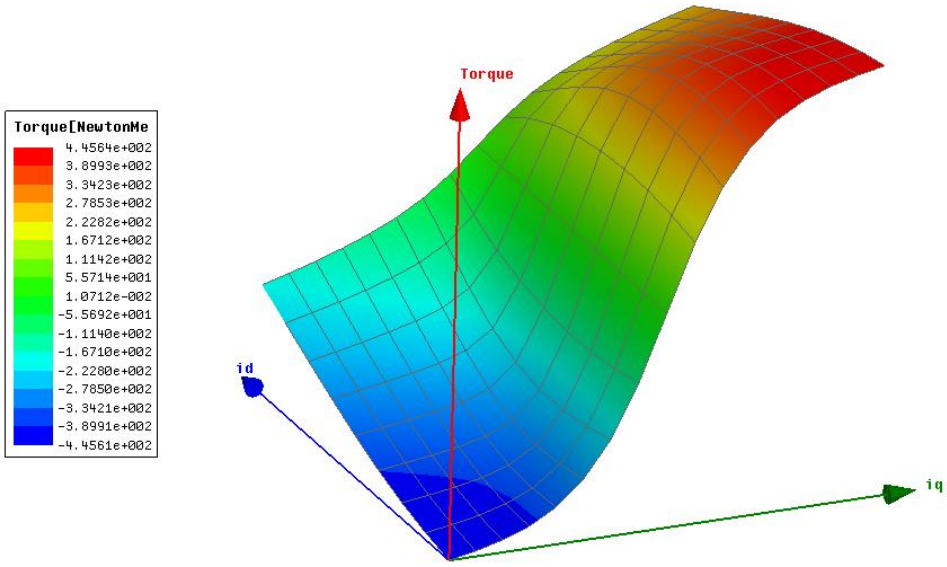

Figure 5.3: Torque is a function of id and iq.

It is often overlooked that the magnet flux linkage is also a function of id and iq, in another word, it is current dependent. Magnet flux linkage obtained at no load is often used, which is a constant. It can be found in Fig.5.3, magnet flux is a function of iq.

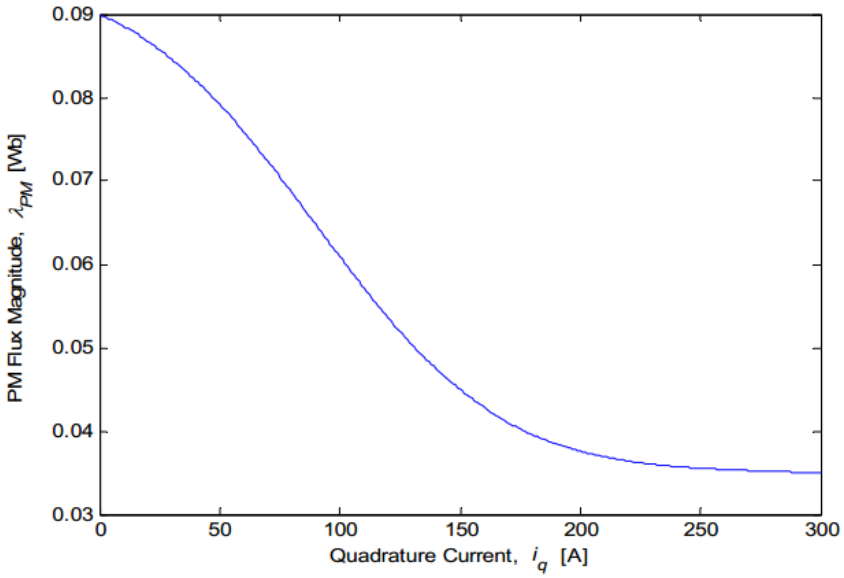

Figure 5.4: PM flux linkage is a function of iq

This dependency can also be recognized if we re-arrange equation (5.7):

$$\lambda_{PM} = (v_q - R_s i_q - L_q \frac{di_q}{dt} - \omega_r L_d i_d) / \omega_r \tag{5.12}$$

We know Ld and Lq are functions of id and iq, so should be the magnet flux linkage. Therefore, to model it correctly, magnet flux linkage should also be extracted from FEA. This requires additional post-processing calculation. The FEA based model is well known to be accurate, but it does not consider the temperature impact on the magnet material which could be substantial.

5.3. The Proposed Temperature Dependent IPM model

To avoid additional calculation for getting magnet flux linkage and incorporate temperature dependence of the permanent magnet, we propose a new model that uses equations (5.1) to (5.3), we write them here again:

$$v_d = R_s i_d + \frac{d\lambda_d}{dt} - \omega_r \lambda_q \tag{5.1}$$

$$v_q = R_s i_q + \frac{d\lambda_q}{dt} + \omega_r \lambda_d \tag{5.2}$$

$$T_e = \frac{3}{2}\frac{P}{2}(\lambda_d i_q - \lambda_q i_d) \tag{5.3}$$

From (5.4) we know that the magnet flux is included in the d axis flux linkage, therefore in our model there is no need to calculate it explicitly.

$$\lambda_d = L_d i_d + \lambda_{PM} \tag{5.4}$$

We extract the d and q flux linkages from FEA at different ids, iqs, and temperatures, so the flux linkages are functions of 3 variables, id, iq and temperature. For completeness, resistance should also be a function of temperature.

$$\lambda_d = f\left(i_d, i_q, Temperature\right) \tag{5.13}$$

$$\lambda_q = f\left(i_d, i_q, Temperature\right) \tag{5.14}$$

$$R_s = f(Temperature) \tag{5.15}$$

Once we collect the flux linkages, the model is implemented using VHDL-AMS language. The detailed implementation of the proposed model is provided in the next section.

5.4. Implementation of The Proposed Model

We use the Toyota Prius 2004 IPM motor as the FEA 2D model and it is shown in Figure 5.5. The PM material is N3521 as shown in Figure 5.6.

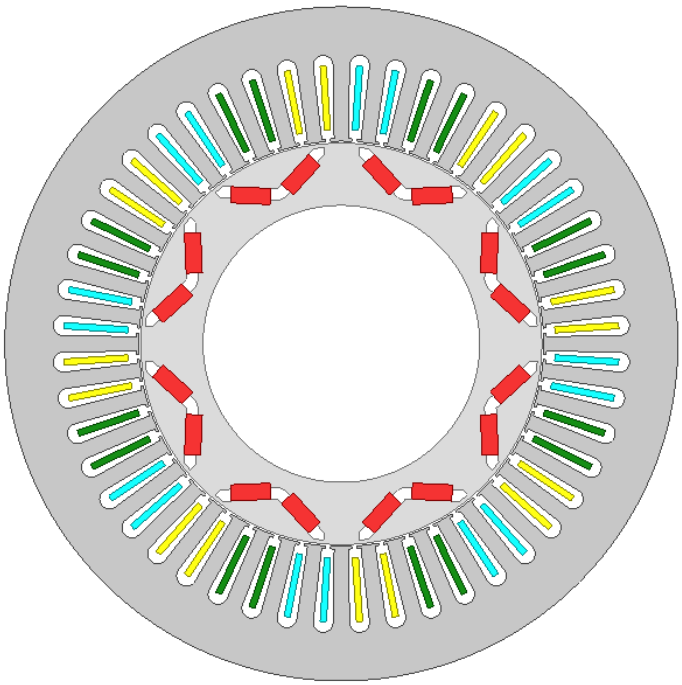

Figure 5.5: IPM FEA model

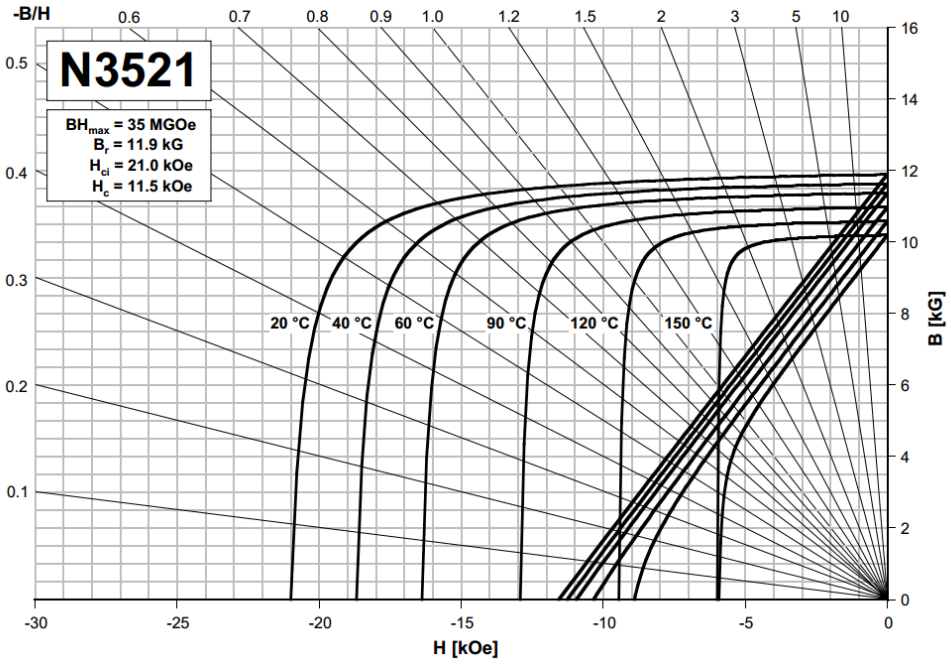

Figure 5.6: PM material N3521

We perform a parametric study for id = -400 to 400A, iq = -400 to 400A, Temperature = 20, 40, 60, 90, 120, 150 °C, total of 1734 variations to capture all the possible operation conditions.

For each variation, the 3 phase flux linkages of the motor model will be calculated from FEA. Figure 5.7 shows the flux linkages for id = 0 A, iq = 100 A, and temperature = 20 °C.

Figure 5.7: 3 phase flux linkages in abc reference frame for id = 0 A, iq = 100 A, temperature = 20 °C

Apply dq transformation to convert the flux linkages from abc reference frame into dq reference frame using (5.15):

$$\begin{bmatrix} \lambda_d \\ \lambda_q \\ \lambda_0 \end{bmatrix} = \frac{2}{3} \begin{bmatrix} \cos(\theta_{me}) & \cos(\theta_{me} - 2\pi/3) & \cos(\theta_{me} + 2\pi/3) \\ -\sin(\theta_{me}) & -\sin(\theta_{me} - 2\pi/3) & -\sin(\theta_{me} + 2\pi/3) \\ 1/2 & 1/2 & 1/2 \end{bmatrix} \cdot \begin{bmatrix} \lambda_a \\ \lambda_c \\ \lambda_c \end{bmatrix} \quad (5.15).$$

Notice λ_0 is zero for balance excitation ia + ib + ic = 0.

The d and q flux linkages is shown in Figure 5.8.

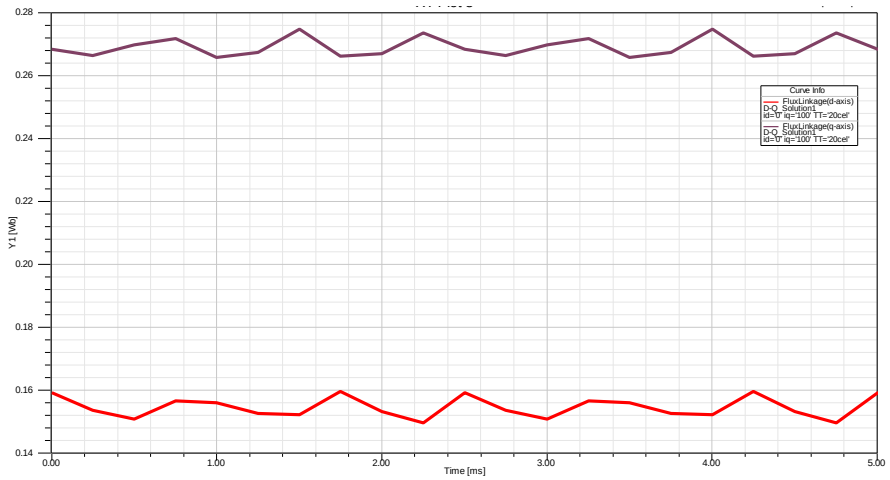

Figure 5.8: d and q flux linkages for id = 0 A, iq = 100 A, temperature = 20 °C

The average dq flux linkages will be used for the proposed motor model. The flux linkages are function of id, iq, and temperature. Figure 5.9 and 5.10 illustrate this.

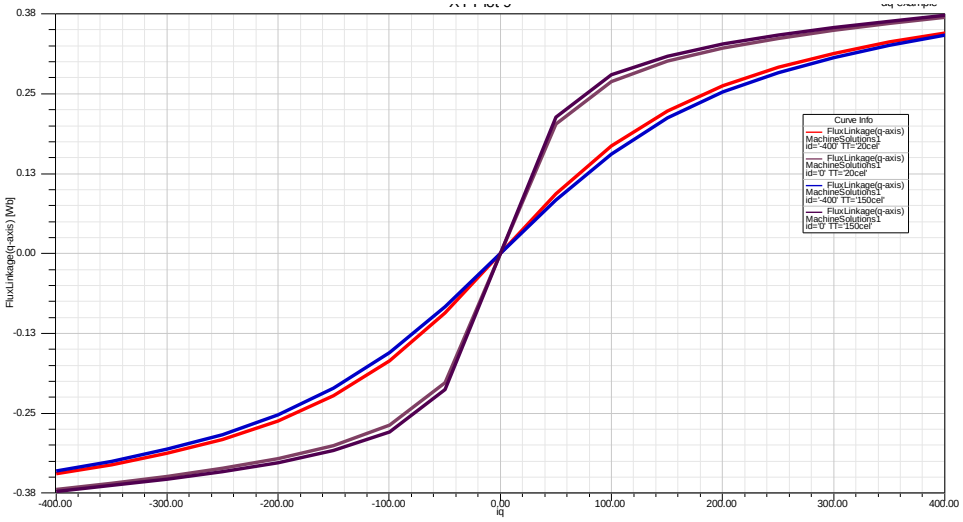

Figure 5.9: Q axis flux linkage is a function of id, iq at 20 °C and 150 °C

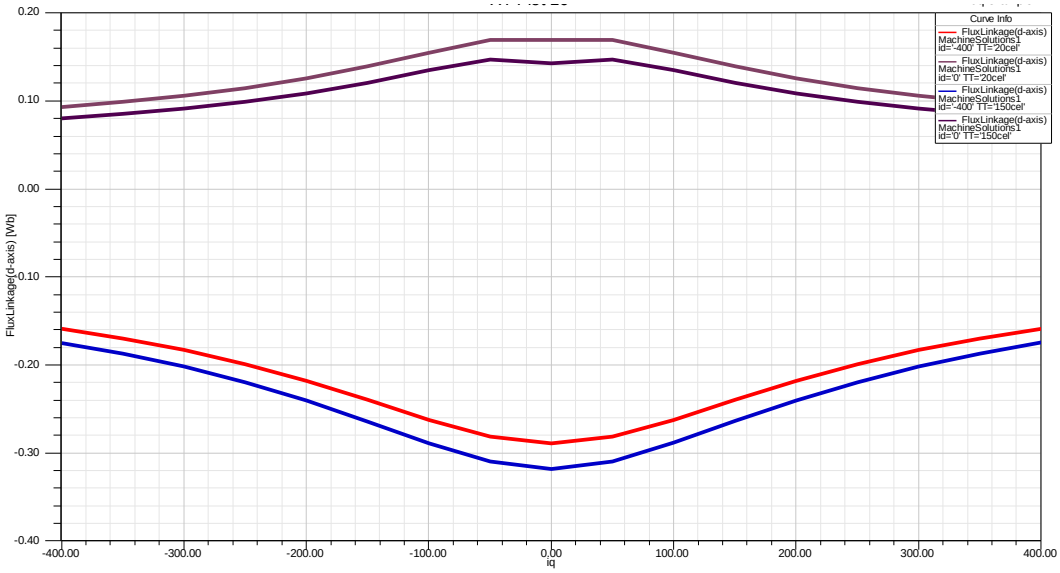

Figure 5.10: D axis flux linkage is a function of id, iq at 20 °C and 150 °C

As a result, from (5.3) we know that torque should also be a function of temperature. Figure 5.11 shows the torque curves vs time. Notice for the same current excitation, the motor generates different torque curves at different temperatures. Figure 5.12 shows that the average torque contours at 20 °C and 150 °C.

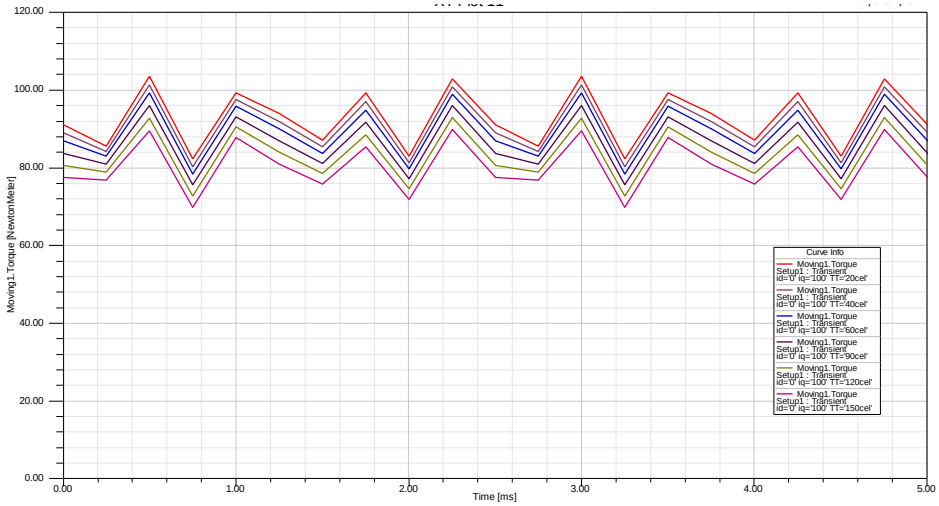

Figure 5.11: Torque is a function of temperature

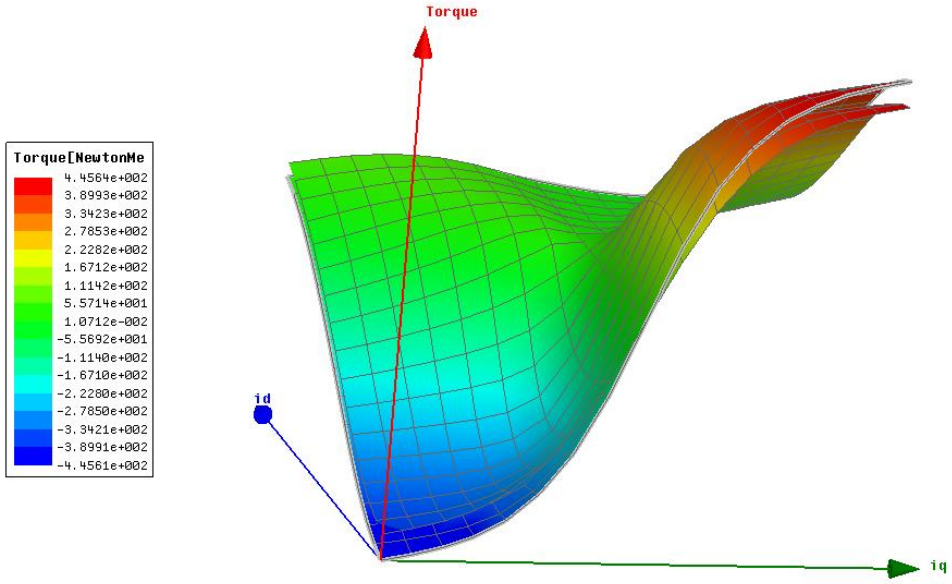

Figure 5.12: Average Torque is a function of id, iq, and temperature

In the proposed model, we will collect the average d and q flux linkages of the IPM motor at 6 temperature values. These values will be used in 3D-lookup table to construct the proposed model in VHDL-AMS language. The d and q flux linkage at temperature 20, 40, 60, 90,

120, and 150 °C are shown from Figure 5.13 to Figure 5.24. In the 12 figures, clearly we find the flux linkages are current dependent and temperature dependent, so is the proposed IPM motor model.

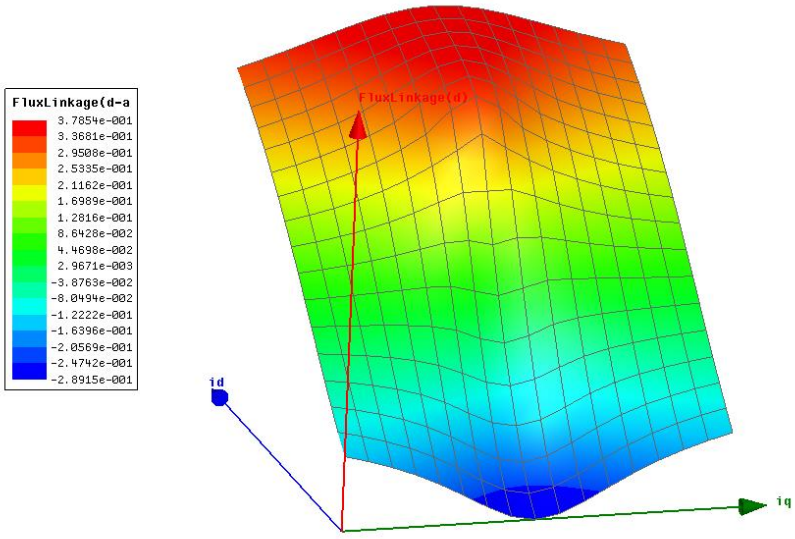

Figure 5.13: D-axis flux linkage at 20 °C

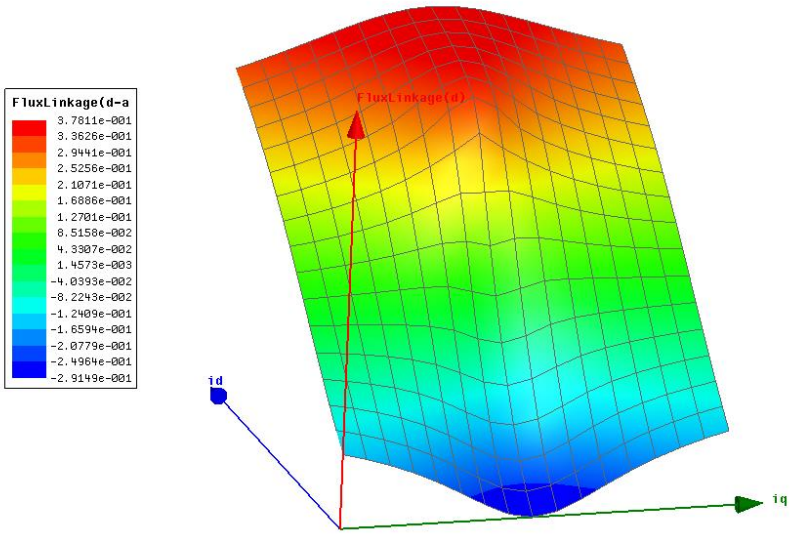

Figure 5.14: D-axis flux linkage at 40 °C

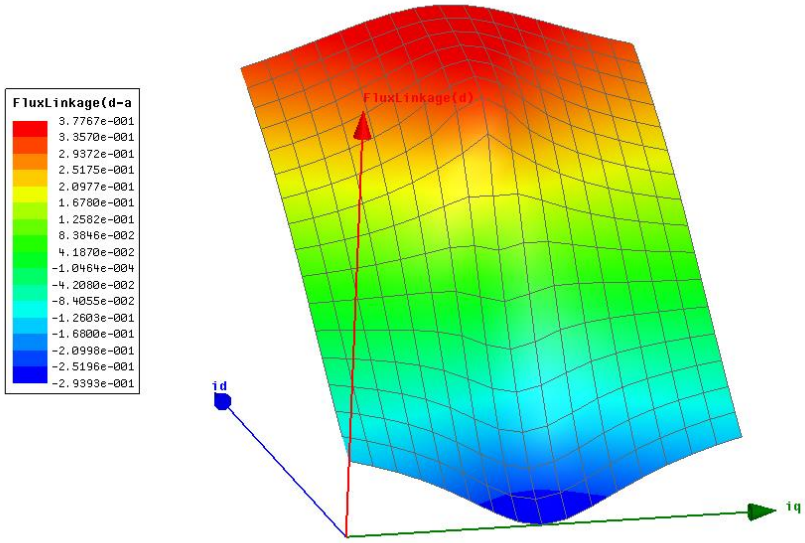

Figure 5.15: D-axis flux linkage at 60 °C

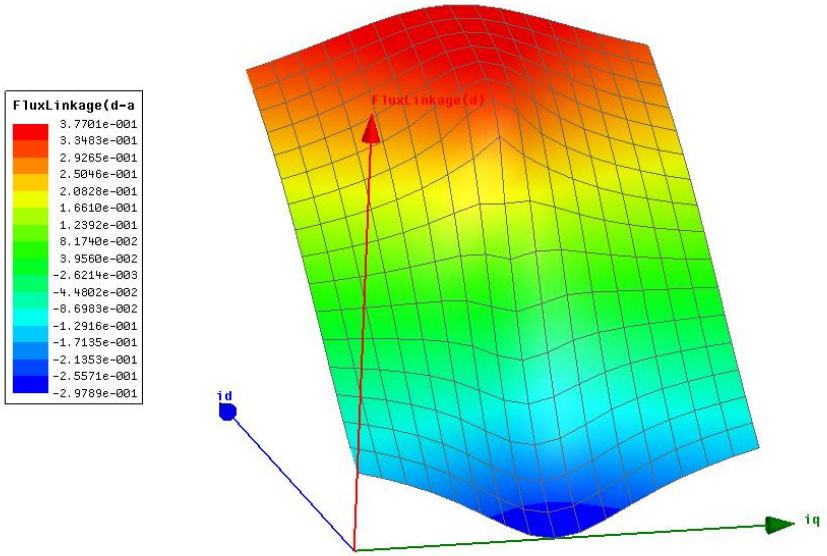

Figure 5.16: D-axis flux linkage at 90 °C

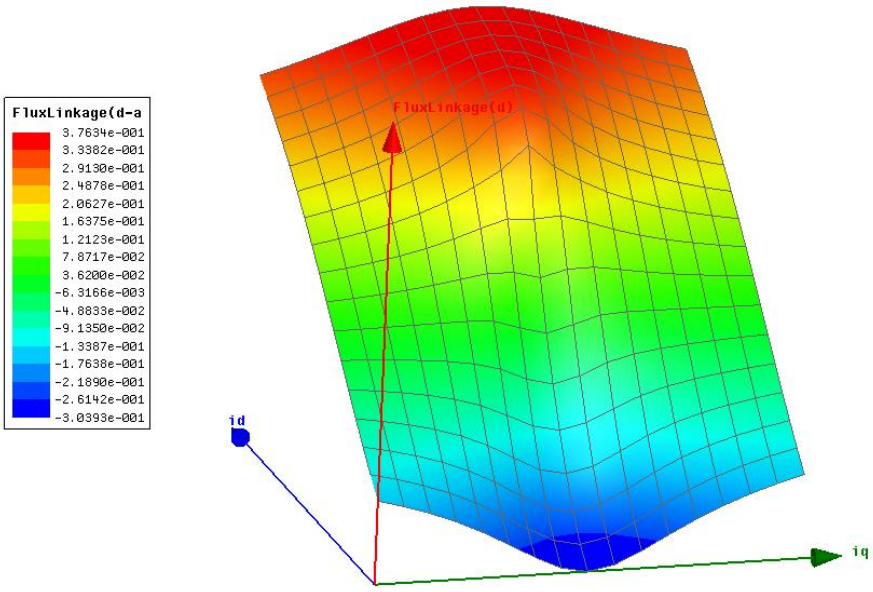

Figure 5.17: D-axis flux linkage at 120 °C

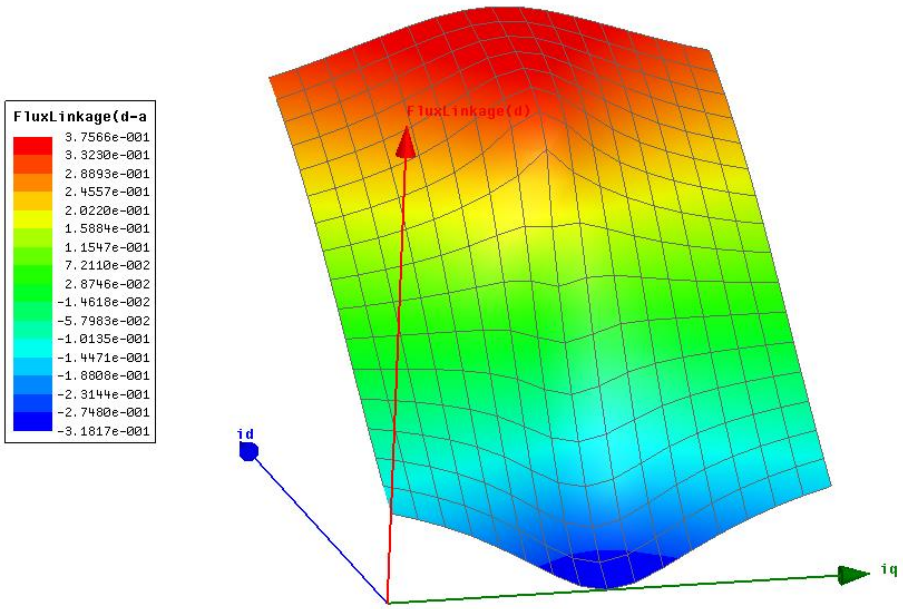

Figure 5.18: D-axis flux linkage at 150 °C

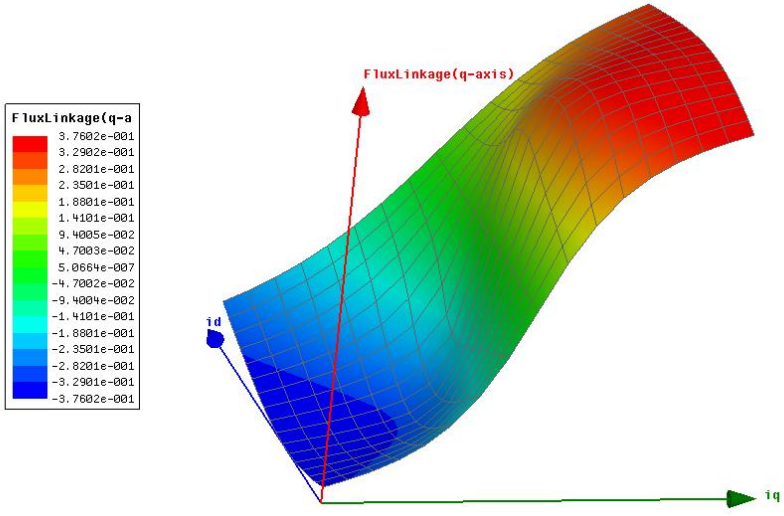

Figure 5.19: Q-axis flux linkage at 20 °C

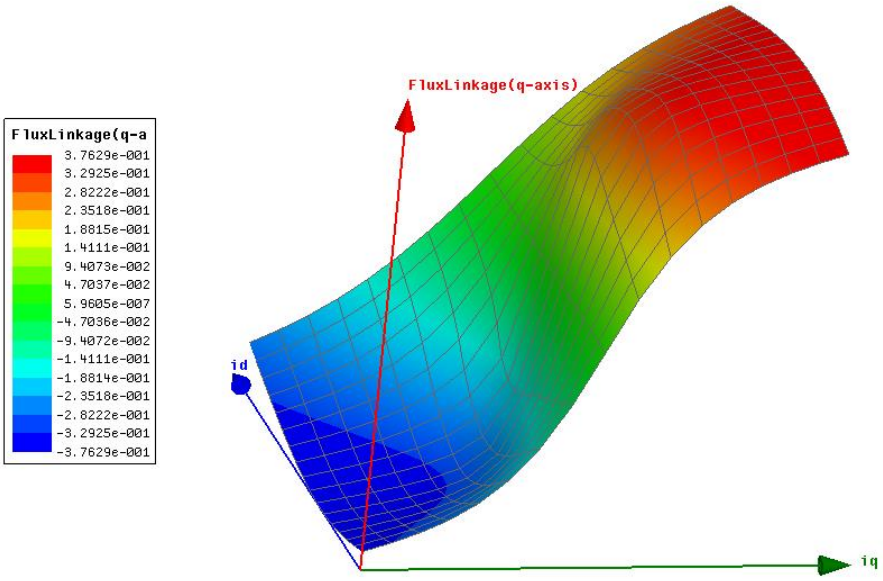

Figure 5.20: Q-axis flux linkage at 40 °C

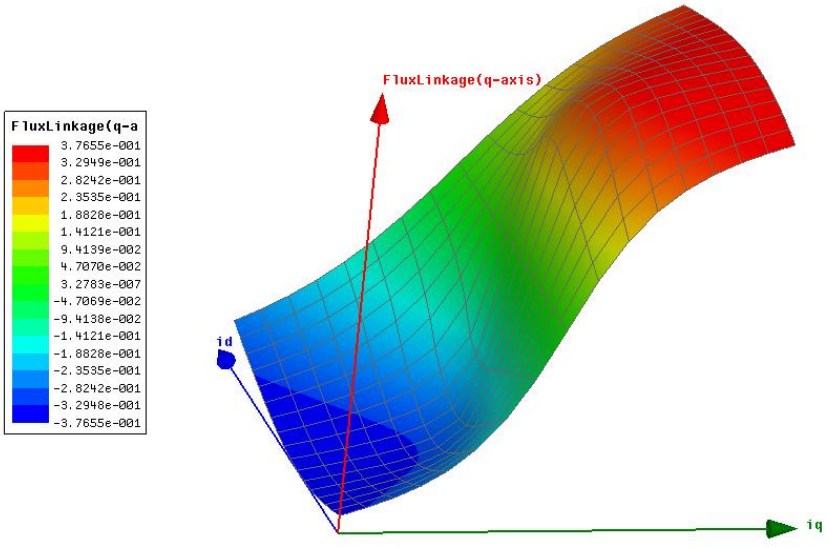

Figure 5.21: Q-axis flux linkage at 60 °C

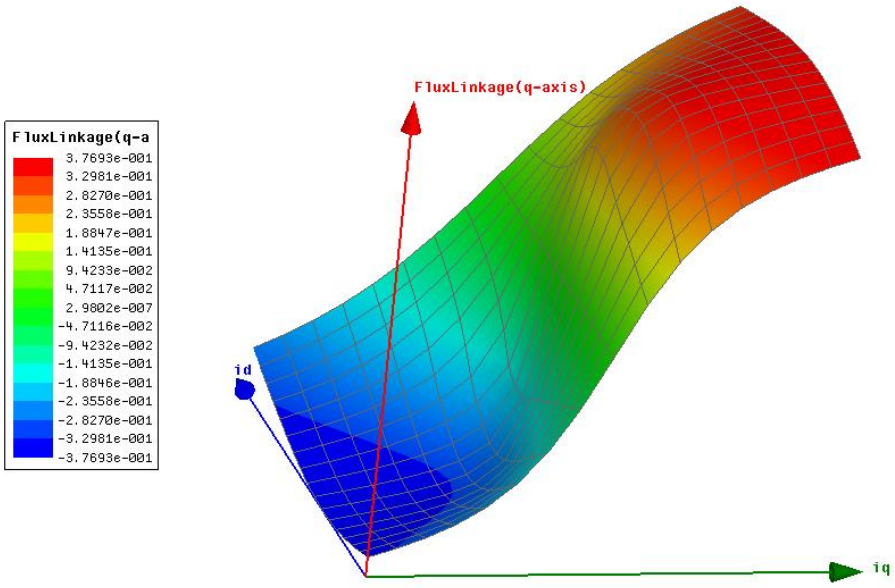

Figure 5.22: Q-axis flux linkage at 90 °C

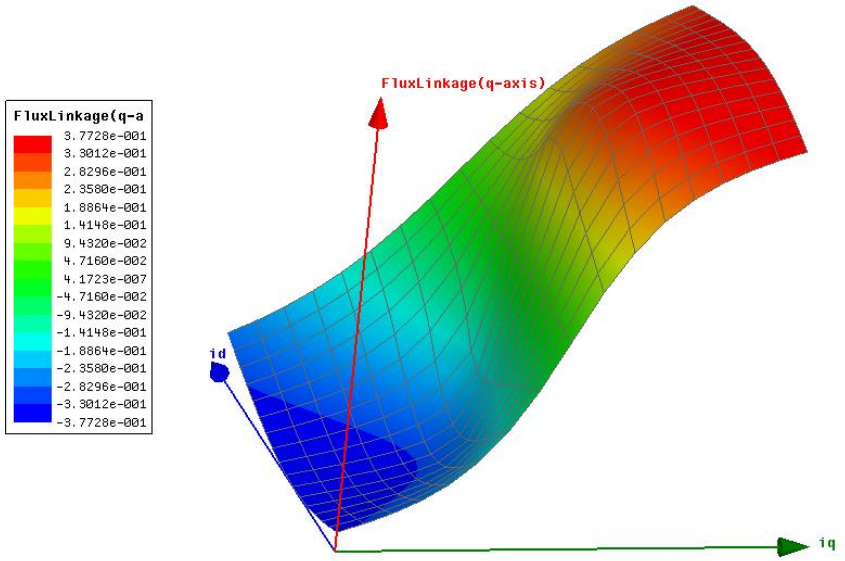

Figure 5.23: Q-axis flux linkage at 120 °C

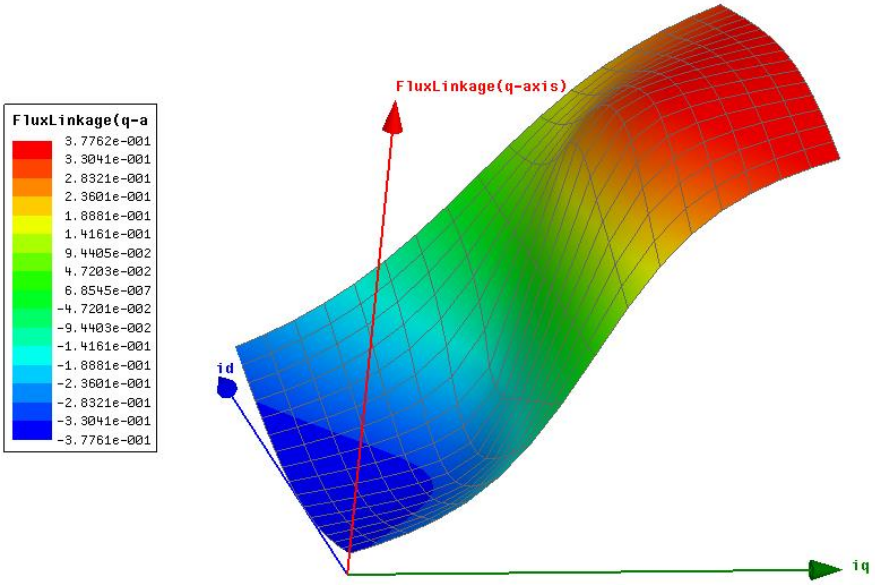

Figure 5.24: Q-axis flux linkage at 150 °C

VHDL-AMS (IEEE 1076.1-1999) is an industry standard multi-domain behavioral description language for modeling and simulation. It is a language extension of the IEEE

standard hardware description language VHDL (IEEE 1076-1993) with the ability to model analog and mixed signal systems. With VHDL-AMS, designers can describe the structure and the functionalities of components and systems at different levels, from the most abstract behavioral description to detailed device level models. Unlike the input-output based causal block oriented modeling approaches used elsewhere, VHDL-AMS provides a more straight-forward and convenient way to model the continuous time dynamics from interconnected components, also known as *acausal modeling*. With acausal modeling, designers do not need to pre-design the computational flow through the system. Well-defined components can be connected directly to represent the system structure. This approach improves reusability of the component models and also makes helps the designer develop more complex hierarchical complex systems.

With equations (5.1),(5.2),(5.3) and (5.9), along with the non-linear temperature dependent flux linkages as shown in Figure 5.13 to Figure 5.24, we construct the proposed IPM model in VHDL-AMS model, 3d look up tables are used to present the flux linkages because the flux linkages are functions of id, iq, and temperature. Figure 5.25 shows the comparison between the results from the proposed model and FEA. The results have excellent agreement in all operation conditions under different temperatures, which validate the proposed IPM model. The proposed model runs at circuit simulation speed which is order of magnitude faster than the FEA simulation. One thing we should point out is that since we use the average flux linkages to model the machine, the torque ripples that we see in the FEA results will not be modeled, we should expect the proposed model to produce the average value of the torque as shown in Figure 5.26.

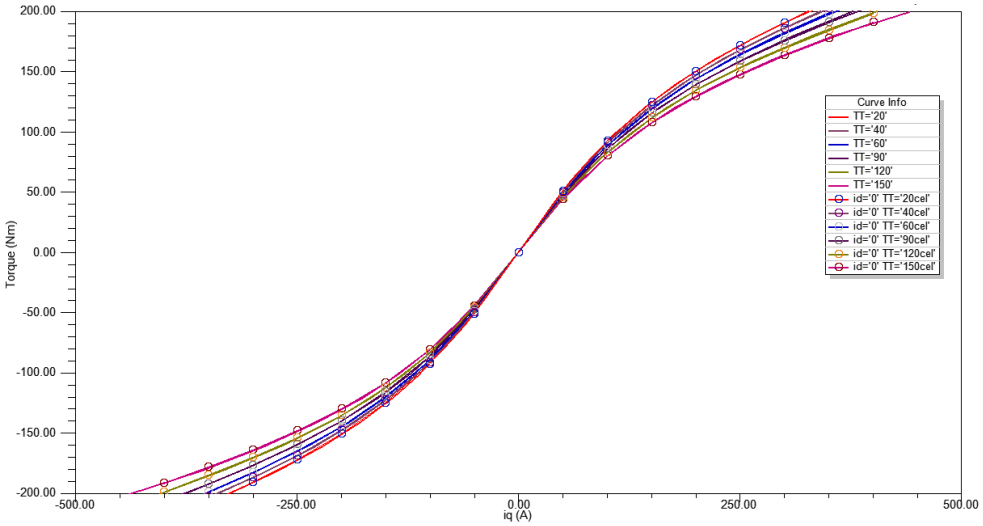

Figure 5.25: Comparison between FEA results and the proposed motor results

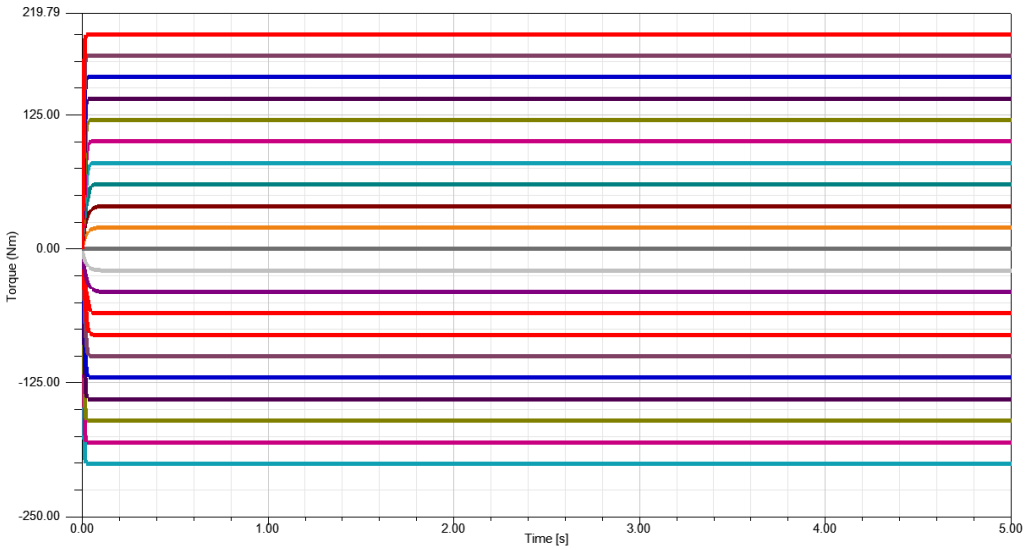

Figure 5.26: Transient torque results of the proposed IPM model

5.5. Summary

IPM motor is both current and temperature dependent. To capture these phenomena, we proposed a new IPM model based on FEA that is suitable for system level simulation. The theory and detailed implementation has been presented, finally, we have validated the proposed model by showing the results of model are in excellent agreement with the FEA results. Even though the flux linkages are obtained from FEA in this work, however they can also be obtained from experiment testing.

CHAPTER 6: VEHICLE SYSTEM MODELING

6.1. Background

Energy efficiency and environment pollution issues are an increasing global concern. For the automotive industry, fuel economy and vehicle emissions are concerns for both manufacturers and customers. A HEV is a vehicle that has both conventional mechanical (i.e. internal combustion engine) and electrical propulsion systems. The electrical powertrain is used to work with the conventional powertrain to achieve higher fuel economy and lower emissions. However, this approach leads to increased design complexity and increased costs [141]-[142]. Computer based modeling and simulation techniques are therefore essential to help reduce the design cost and optimize system performance. Due to the complexity of hybrid vehicles, multi-domain modeling ability is preferred for both component modeling and system simulation.

In this work, we present a HEV library developed using VHDL-AMS. The library provides reusable and extensible generic components for further design.

6.2. Library structure and library component

The elements in the library can be classified into three main categories: data/control components, mechanical components and electrical components.

6.2.1. Data/Control Components

The **data/control components** include components for data processing, control and signal distribution purposes. There are four components in the data/control category: driving cycle, driver, central controller and motor controller.

The *driving cycle* component provides desired vehicle velocity for the vehicle to follow. It is achieved by using a 2-dimensional look-up table model which uses imported time-speed data from standard drive cycles [143]-[144].

The *driver* model represents the velocity tracking behavior, which is used to minimize the difference between vehicle velocity reference and the actual system calculated vehicle velocity. Two PI controllers are used to generate the control signals for propulsion and brake operations separately [145]. The driver also need to indicate what condition the vehicle is in (e.g. start, drive , stop) to help other controllers or components to take different behaviors in different stage.

The *central controller* is the main controller to handle the control signal distribution. One of its functionalities is to define the power distribution of the mechanical and electrical propulsion and braking system. In this model, a simple engine on-off control is implemented to achieve simple HEV control strategy [145]. However, it is very easy for the user to customize the control strategy in different test case scenario.

The *motor controller* is used to generate voltage and current for the DC motor based on desired motor torque and estimated motor rotational speed. It also gives the connection between battery and motor.

6.2.2. Electrical Components

The electrical components mainly contain the models for the electrical propulsion system. The DC motor and battery model are described as follow.

6.2.2.1 Electrical Motor

The *electrical motor* model represents the mathematical modeling of the permanent magnet DC motor (PMDC) following [146]. The voltage over the DC motor can be given by (6.1) by using Kirchoff's law:

$$V_m = R_a i_m + L_a \frac{di_m}{dt} + V_{emf} \tag{6.1}$$

where R_a is the armature resistance, L_a is the armature inductance , V_{emf} is the back emf of the motor and i_m is the current through the DC motor. The generated motor torque can be given approximately by

$$T_m = k_i \cdot i_m \tag{6.2}$$

where k_i is the so-called motor torque constant. The back emf is also related to the mechanical part by

$$V_{emf} = k_e \omega_m \tag{6.3}$$

where k_e is the back emf constant, ω_m is the rotational velocity of the motor. The motor dynamics is represented by

$$T_m = J\dot{\omega}_m + b\omega_m \tag{6.4}$$

where J is the system inertia, b is the friction coefficient. The system inertia is evaluated during the entire system simulation, and it changes when vehicle conditions change.

6.2.2.2 Battery (VDA/FAT AK30 Library)

The currently used *battery* model is not in the Simplorer HEV library, it is from **VDA/FAT AK30 Library**. It uses look-up tables to represent the battery characteristics (VDA/FAT 2013).

6.2.3. Mechanical Components

The mechanical components mainly contain the models for the mechanical propulsion and brake systems as well as the connection/coupling parts for the mechanical-electrical combination. It includes the internal combustion engine, fuel tank, clutch, transmission, mechanical torque coupling, brake, wheel and vehicle body (chassis).

6.2.3.1 Internal Combustion Engine (ICE)

The *internal combustion engine* (ICE) model is a so-called mean value internal combustion engine model following [147]-[148]. It is mainly composed by three components, includes throttle body, intake manifold and engine cylinder. The air mass flow rate throttled into engine can be given by

$$\dot{m}_{thr} = \dot{m}_{\max} \cdot A_{thr} \cdot f\left(\frac{P_{im}}{P_{atm}}\right) \tag{6.5}$$

where $\dot{m}_{\max}$ is the maximum air mass flow rate with an entirely opened throttle. A_{thr} is the normalized throttle area can be given by

$$A_{thr} = \begin{cases} -\dfrac{d \cdot D}{2}\sqrt{1-a^2} + \dfrac{d \cdot D}{2}\sqrt{1-\left(a\dfrac{\cos\varphi_0}{\cos\varphi}\right)^2} + \dfrac{D^2}{2}\arcsin\sqrt{1-a^2} - \\ \dfrac{D^2}{2}\dfrac{\cos\varphi}{\cos\varphi_0}\arcsin\sqrt{1-\left(a\dfrac{\cos\varphi_0}{\cos\varphi}\right)^2} & \text{if } \varphi < \arccos\left(a\cos\varphi_0\right) - \varphi_0 \\ \dfrac{D^2}{2}\arcsin\sqrt{1-a^2} - \dfrac{d \cdot D}{2}\sqrt{1-a^2} & \text{otherwise} \end{cases} \tag{6.6}$$

where d is the throttle pin diameter, D is the throttle bore and $a = d/D$; φ and φ_0 are the throttle angle and the throttle angle at closed position, respectively. The pressure ratio can be given by

$$f\left(\frac{P_{im}}{P_{atm}}\right)=\begin{cases}2\sqrt{\frac{P_{im}}{P_{atm}}-\left(\frac{P_{im}}{P_{atm}}\right)^2} & \text{if } P_{im}>\frac{P_{atm}}{2}\\ 1 & \text{otherwise}\end{cases} \tag{6.7}$$

The air dynamics in the intake manifold can be given by

$$\frac{dm_{im}}{dt}=\dot{m}_{thr}-\dot{m}_e \tag{6.8}$$

With isothermal assumption, we have

$$T_{thr}=T_{im} \text{ and } P_{im}=\frac{RT_{im}}{V_{im}m_{im}} \tag{6.9}$$

where R is the gas constant. The mass flow rate to the engine is

$$\dot{m}_e=\frac{n_{cyl}\eta_{vol}m_{im}\omega_e V_d}{4\pi V_{im}} \tag{6.10}$$

where n_{cyl} is the number of cylinders, ω_e is the engine rotational velocity, V_d is the cylinder displacement volume. η_{vol} is the volumetric efficiency of engine, can be given by

$$\eta_{vol}=\left(24.5\omega_e-3.1\times10^4\right)m_{im}^2+\left(-0.167\omega_e+222\right)m_{im}+\left(8.1\times10^{-4}\omega_e+0.352\right) \tag{6.11}$$

The fuel dynamics is described as

$$\tau_f\ddot{m}_{fi}+\dot{m}_{fi}=\dot{m}_{fc}=\frac{\dot{m}_e}{r_{AF}} \tag{6.12}$$

Where τ_f is the fueling time constant. $\dot{m}_{fc}$ and $\dot{m}_{fi}$ are the requested and actual fuel mass flow rate, respectively. r_{AF} is the air/fuel ratio into the engine. The engine rotational dynamics can be describe as

$$J_e\dot{\omega}_e = T_i - T_f - T_p \tag{6.13}$$

where J_e is the engine inertia; T_i is the engine indicated torque given by

$$T_i = c_T \frac{\dot{m}_e}{\omega_e} \cdot c_{AFI} \cdot c_{SI} \tag{6.14}$$

where c_T is the maximum torque constant of engine for specified $\dot{m}_e$. c_{AFI} is the normalized air fuel influence coefficient given by

$$c_{AFI} = \cos\left(7.3834\left(r_{AF} - 13.5\right)\right) \tag{6.15}$$

c_{SI} is the normalized spark influence coefficient given by

$$c_{SI} = \left(\cos\left(SA - MBT\right)\right)^{2.875} \tag{6.16}$$

where $\left(SA - MBT\right)$ is the difference of spark advance from top dead center and the minimum spark advance for best torque. T_f is the friction torque of engine given by

$$T_f = 0.1056\omega_e \tag{6.17}$$

T_p is the engine output torque to the clutch.

6.2.3.2 *Fuel Tank*

The *fuel tank* model is a tank model to represent the fuel change and the fuel remain in the tank. The fuel consumption rate can be given by

$$FR = \frac{\dot{m}_{fuel}}{\rho_{fuel} \cdot V_{tank}} \tag{6.18}$$

where $\dot{m}_{fuel}$ is the mass flow rate of fuel consumption estimated from ICE model. ρ_{fuel} is the fuel density and V_{tank} is the volume of the fuel tank.

6.2.3.3 *Clutch*

The *clutch* model describes a simple behavior of clutch based on the control signal *lock* from the controller. When *lock* is true then the torque and the rotational velocity is fully transferred, otherwise, the torque and rotational velocity are not transferred. A more detailed clutch model is under development.

6.2.3.4 *Transmission*

The *transmission* model simply represents the transmission performance based on given gear ratio data set (Ehsani, Gao and Emadi 2007). The equations can be given by

$$\omega_{in} = r_{gear} \cdot \omega_{out} \tag{6.19}$$

$$T_{in} \cdot \eta_{tran} \cdot r_{gear} + T_{out} \tag{6.20}$$

where ω_{in} and T_{in} are the rotational velocity and torque transferred from clutch, respectively; ω_{out} and T_{out} are the rotational velocity and torque transferred to mechanical torque coupling,

respectively; r_{gear} is the gear ratio selected by central controller based on vehicle condition and η_{tran} is the transmission efficiency.

6.2.3.5 Mechanical Torque Coupling

The *mechanical torque coupling* model represents the torque coupling from the conventional powertrain line and electrical motor line following [149]. The torque coupling can be given by

$$T_3 + k_1 \cdot T_1 + k_2 \cdot T_2 = 0 \tag{6.21}$$

where T_1, T_2 and T_3 are the torque from the electrical propulsion system, torque from the mechanical propulsion system and torque transfer to wheel, respectively. k_1 and k_2 are coefficients depending on the coupling type. For pulley or chain assembly, $k_1 = r_2 / r_1$ and $k_2 = 1$, where r_1 and r_2 are the radii of pulley 1 and pulley 2 respectively. The rotational velocities can be given by

$$k_1 \cdot \omega_3 = \omega_1 \tag{6.22}$$

$$k_2 \cdot \omega_1 = k_1 \cdot \omega_2 \tag{6.23}$$

where ω_1, ω_2 and ω_3 are the rotational velocities from electrical propulsion system, mechanical propulsion system and transfer to wheel, respectively.

6.2.3.6 Brake

The *brake* model describes the performance of the vehicle brake system following [150]. The pressure in the master cylinder can be described as

$$P_{mc} = \left(F_{in} - F_{cs} - F_{cf} \right) / A_{mc} \tag{6.24}$$

where F_{in} is the input force to the brake system, given by

$$F_{in} = c_s \cdot f_{max} \tag{6.25}$$

where c_s is the control signal from the controller, f_{max} is the maximum force can be provided. F_{cs} is the master cylinder spring pre-load, F_{cf} is the seal friction in the cylinder and A_{mc} is the area of master cylinder. The dynamics of the volume of displaced brake fluid can be given by

$$\dot{V}_b = \text{sgn}\left(P_{mc} - P_w \right) c_q \sqrt{|P_{mc} - P_w|} \tag{6.26}$$

where c_q is the effective flow coefficient and the lumped fluid capacity of the brake system is given by

$$P_w = 23.4375 \cdot V_b^3 + 89.0625 \cdot V_b^2 + 356.25 \cdot V_b \tag{6.27}$$

And the output torque can be given by

$$T_b = \begin{cases} k_b \left(P_w - P_{po} \right) & \text{if } P_w \geq P_{po} \\ 0 & \text{otherwise} \end{cases} \tag{6.28}$$

with $k_b = 1.05$ and $P_{po} = 5.7143$.

6.2.3.7 Wheel

The *wheel* model describes the longitudinal direction wheel dynamics as well as the slip. The relation between friction and the slip is provided by empirical function. Only one wheel is

considered in the modeling for simplicity (the so-called quarter car model). The rolling resistance is moved to the chassis (vehicle body) part, together with all other driving resistance [151]-[152]. The slip ratio can be calculated as

$$\lambda = \begin{cases} (v_w - v_{veh})/v_w & \text{if } \dot{v}_{veh} > 0 \\ (v_w - v_{veh})/v_{veh} & \text{otherwise} \end{cases} \tag{6.29}$$

where $v_w = \omega_w \cdot r_w$ with ω_w as the wheel rotational velocity and r_w as the wheel radius. The wheel dynamics can be presented as

$$J_w \frac{d\omega_w}{dt} = T_w + r_w \cdot f_{long} \tag{6.30}$$

where J_w is the inertia of the wheel, T_w is the torque from mechanical coupling and f_{long} is the longitudinal wheel friction force, which can be further obtained by

$$f_{long} = \left(d_x \sin\left(c_x \arctan\left(b_x \phi\right)\right) + s_{vx}\right) \cdot \cos(\alpha) \tag{6.31}$$

where $b_x, c_x d_x$ and s_{vx} are all fitted wheel constant. α is the grading angle and ϕ can be obtained from

$$\phi = (1 - e_x)(\lambda + S_{hx}) + \frac{e_x}{b_x} \arctan\left(b_x (\lambda + S_{hx})\right) \tag{6.32}$$

where e_x and S_{hx} are constants fitted from test data.

6.2.3.8 Vehicle Body

The *vehicle body* (chassis) model simply describes the performance of vehicle body with consideration of rolling resistance, aerodynamic drag, grading resistance and dynamic behavior

of the chassis. The vehicle velocity is always assumed as positive in this model. The chassis dynamics can be presented as

$$m_{veh}\frac{d\dot{v}_{veh}}{dt} = f_{veh} + \left(f_{rol} + f_{wind}\right)\cdot \mathrm{sgn}\left(v_{veh}\right) + f_{grad} \tag{6.33}$$

where m_{veh} is the mass of the vehicle and f_{veh} is the force from wheel; the rolling force can be given by

$$f_{rol} = m_{veh}\cdot g\cdot c_{rr}\cos(\alpha) \tag{6.34}$$

where the rolling resistance coefficient can be obtained by :

$$c_{rr} = 0.01\cdot\frac{1+v_{veh}}{160} \tag{6.35}$$

The aerodynamic drag force from wind can be given by

$$f_{wind} = \frac{1}{2}\rho_{air}A_{front}c_{drag}\left(v_{veh}-v_{wind}\right)^2 \tag{6.36}$$

where ρ_{air} is the air density, A_{front} is the vehicle front projection area, c_{drag} is the air drag coefficient and v_{wind} is the wind velocity. The grading force can be obtained by

$$f_{grad} = m_{veh}\cdot g\cdot\sin(\alpha) \tag{6.38}$$

6.3. Application example and simulation

Three applications of hybrid electrical vehicle, conventional vehicle and electrical vehicle constructed by the library components are discussed in this section.

6.3.1. Hybrid Electrical Vehicle

The hybrid electrical vehicle application schematic is shown as Figure 6.1, it mainly contains 14 components: driving cycle, driver, central controller, motor controller, electrical motor, battery, and internal combustion engine (ICE), fuel tank, clutch, transmission, and mechanical coupling, brake, wheel and vehicle body.

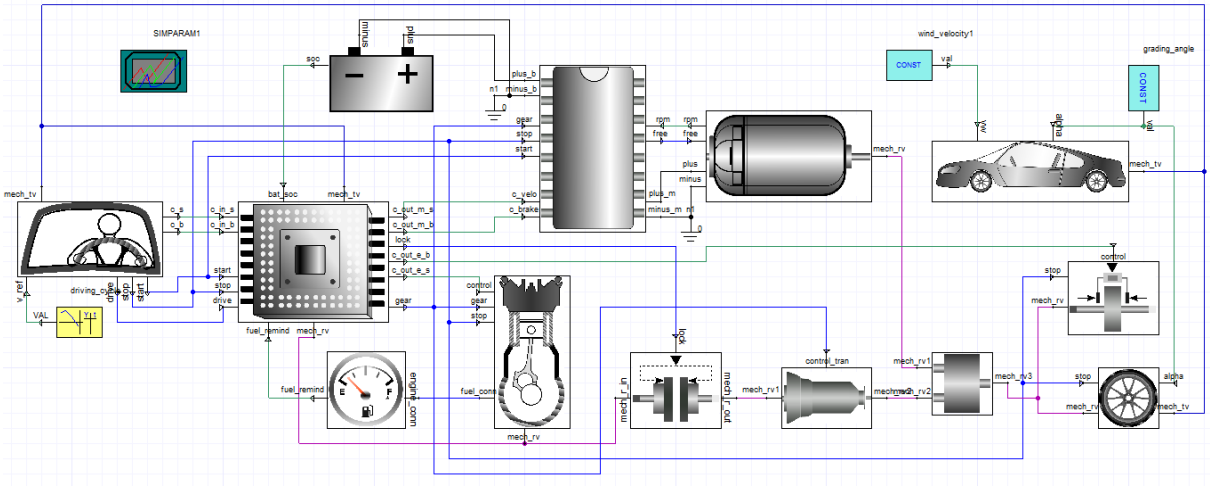

Figure 6.1: Hybrid electrical vehicle/conventional vehicle schematic

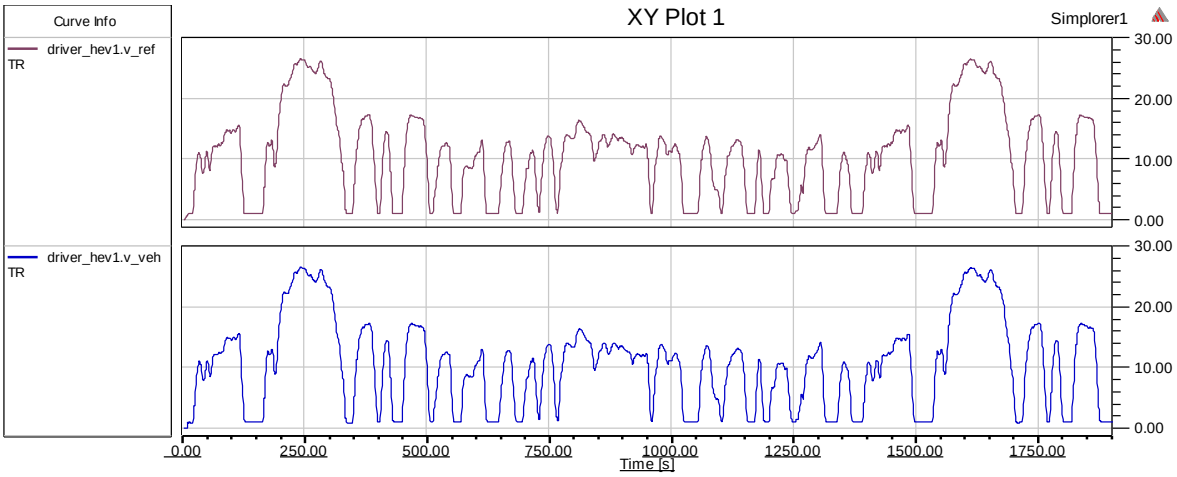

Figure 6.2: Given reference velocity vs. model calculated vehicle velocity of HEV application

When starting simulation, the hybrid electrical vehicle model follows the provided velocity reference from the *driving cycle* component. Two parallel connected powertrains (the **EM-Battery line** and the **conventional ICE line**) are combined together to provide the propulsion and brake power for the vehicle. The fuel in the fuel tank is continuously consumed whenever the ICE is on. The battery will be charged when braking and will be discharged when provide power to the vehicle. The power distribution follows the desired control strategy defined in the central controller component. Figure 6.2 shows the comparison of the given reference velocity from driving cycle and the achieved simulated vehicle velocity for the hybrid electrical vehicle. The two velocities correspond closely as expected. The fuel remaining in the fuel tank and the battery state of charge (SOC) changes during the vehicle driving process of HEV application is shown in Figure 6.3 and Figure 6.4 shows the performance attributes of the ICE. The slip ratio and the torque from mechanical coupling of wheel during the driving cycle are shown in Figure 6.5.

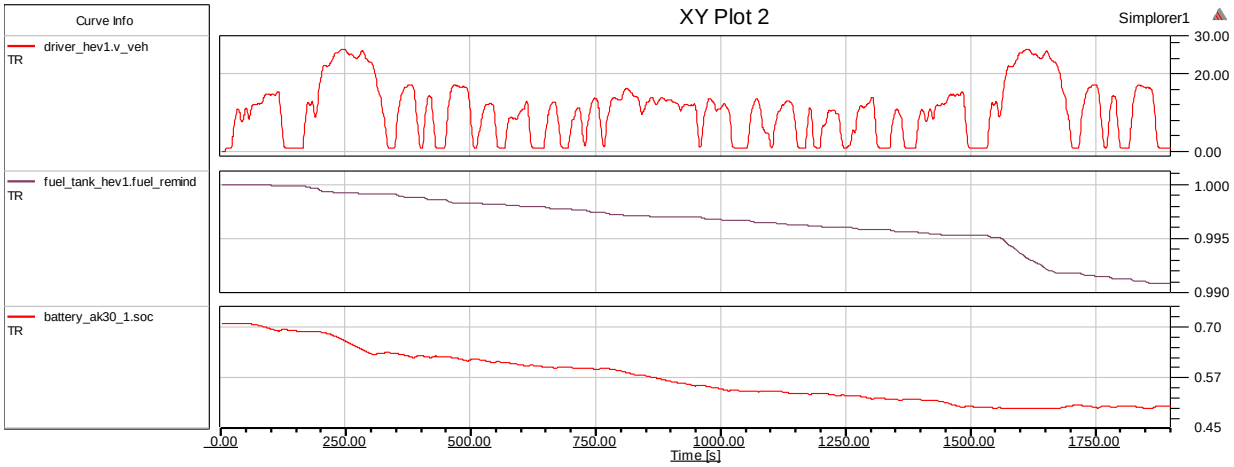

Figure 6.3: Model calculated vehicle velocity vs. fuel remain and battery SOC of HEV application

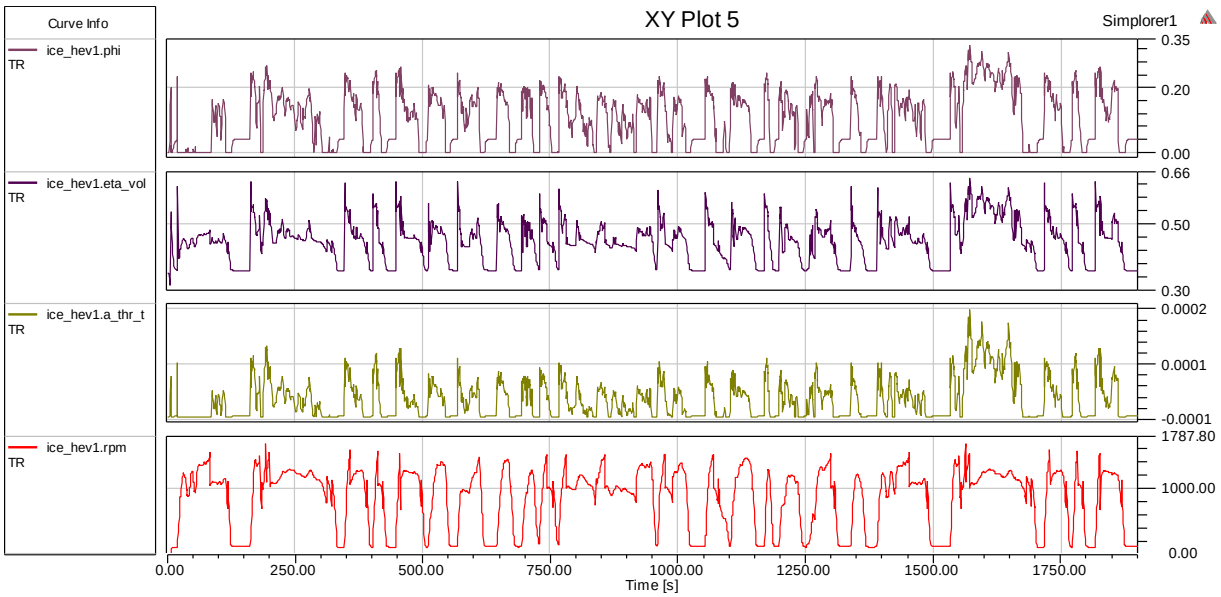

Figure 6.4: Throttle angle, volumetric efficiency, normalized throttle area and rotational speed of engine

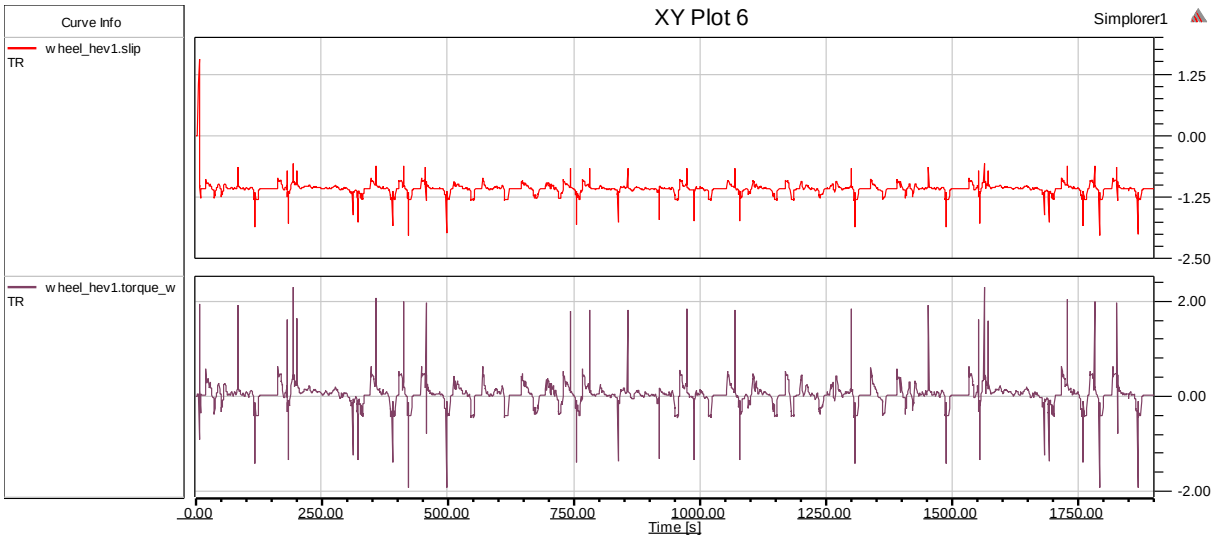

Figure 6.5: Slip ratio and torque from wheel during the driving process

6.3.2. Conventional Vehicle

The conventional vehicle application has the similar structure as the HEV in Figure 6.1. The primary difference between the two configurations is that the ICE line is the only powertrain used to provide the propulsion and brake power when in the driving phase. The EM-Battery line is only used to help the vehicle start. In this application example, the battery is only discharged at the initial start point, and then keeps the same SOC (state of charge) as the vehicle is in the driving phase. The fuel in the fuel tank is continuously consumed since ICE is always in operation. The fuel remaining in the fuel tank and the battery state of charge (SOC) changes during the vehicle driving process of CV application are shown in Figure 6.6. From Figure 6.6, it is obvious that the motor line is disabled after start period.

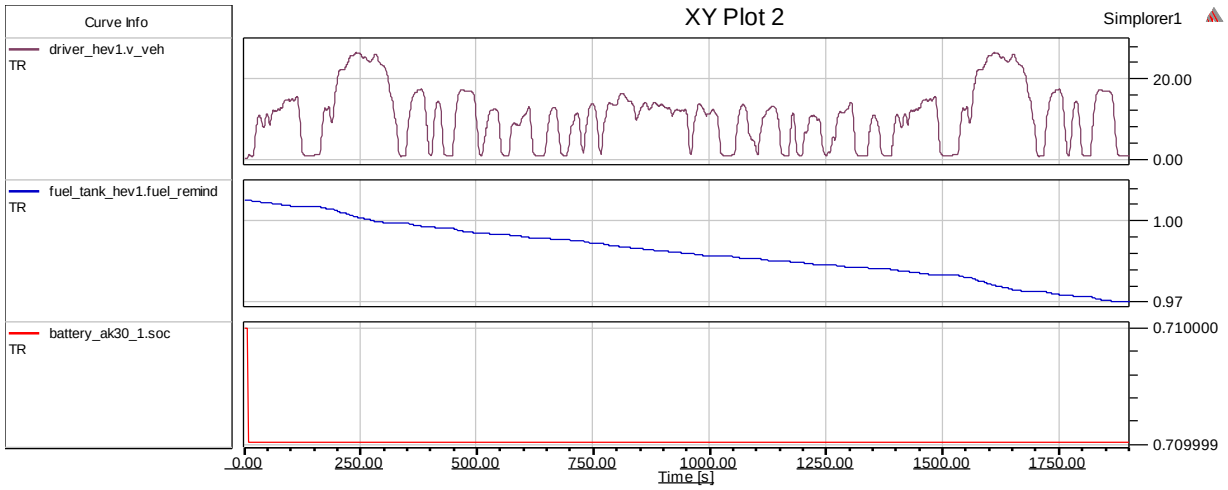

Figure 6.6: Model calculated vehicle velocity vs. fuel remain and battery SOC of CV application

6.3.3. Electrical Vehicle

The structure of the pure electrical vehicle is shown in Fig 6.7. It is different from the CV/HEV applications; the mechanical powertrain is removed in this application example. The electrical vehicle application mainly contains 10 components: driving cycle, driver, central controller (for EV), motor controller, electrical motor, battery, clutch, brake, and wheel and vehicle body. In this application example, the EM-Battery line is the only powertrain used to provide the propulsion and brake power in the driving phase, the battery will be charged when brake and will be discharged when provide propulsion power to speed up the vehicle. The battery SOC change during the vehicle driving process of EV application is shown in Figure 6.8.

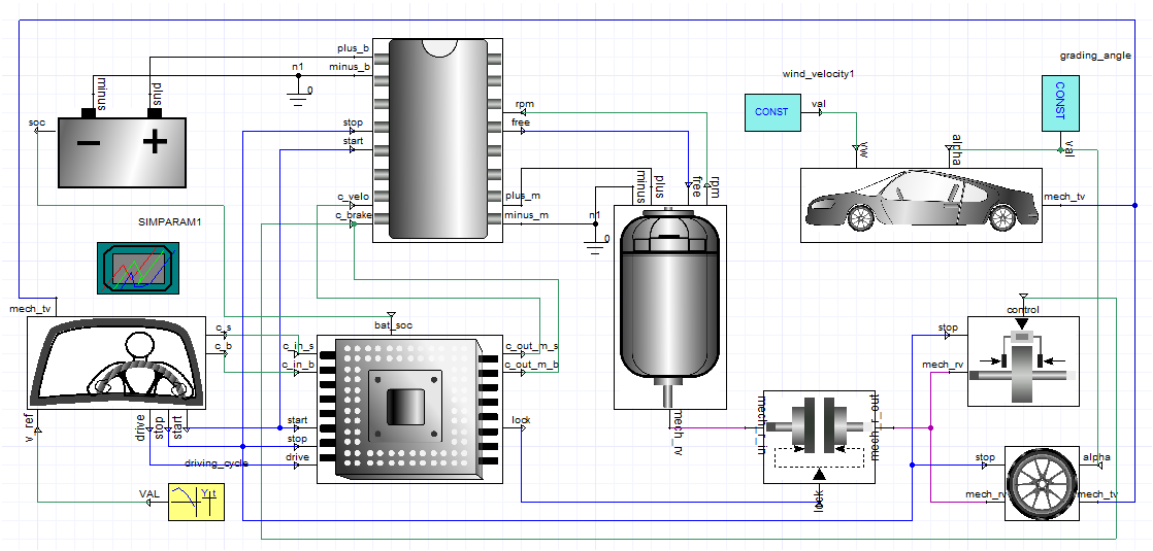

Figure 6.7: Electrical vehicle schematic

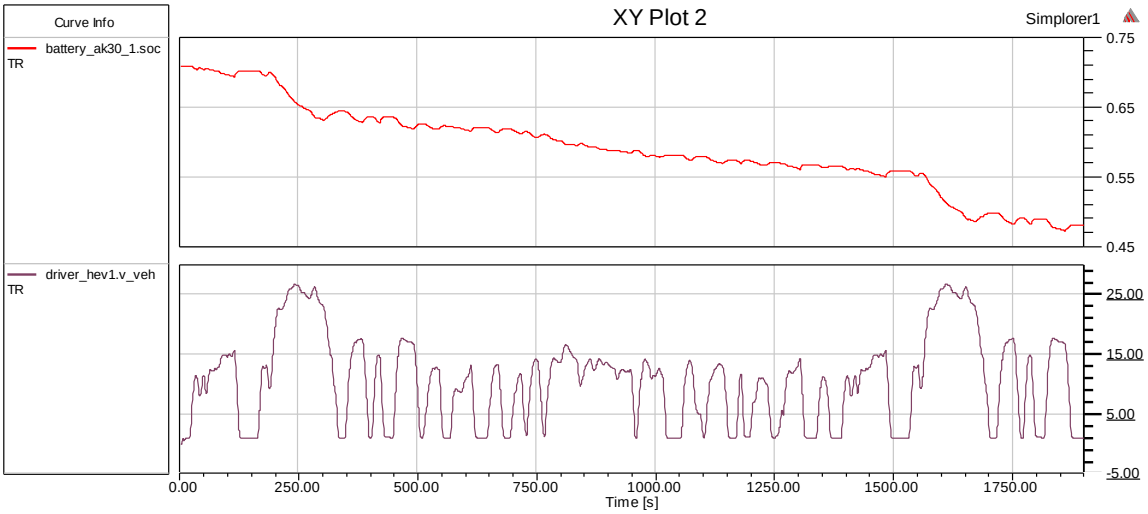

Figure 6.8: Battery SOC of EV application vs. model calculated vehicle velocity

Finally, we incorporate the temperature dependent IPM model proposed in Chapter 5 into the HEV model, and command the HEV to follow the city drive cycle 75 as in Figure 6.9 at

magnet temperature 20, 80, 150 °C. The current profiles are shown in Figure 6.10 and Figure 6.11. Higher the operating magnet temperature, higher current is used to supply the motor.

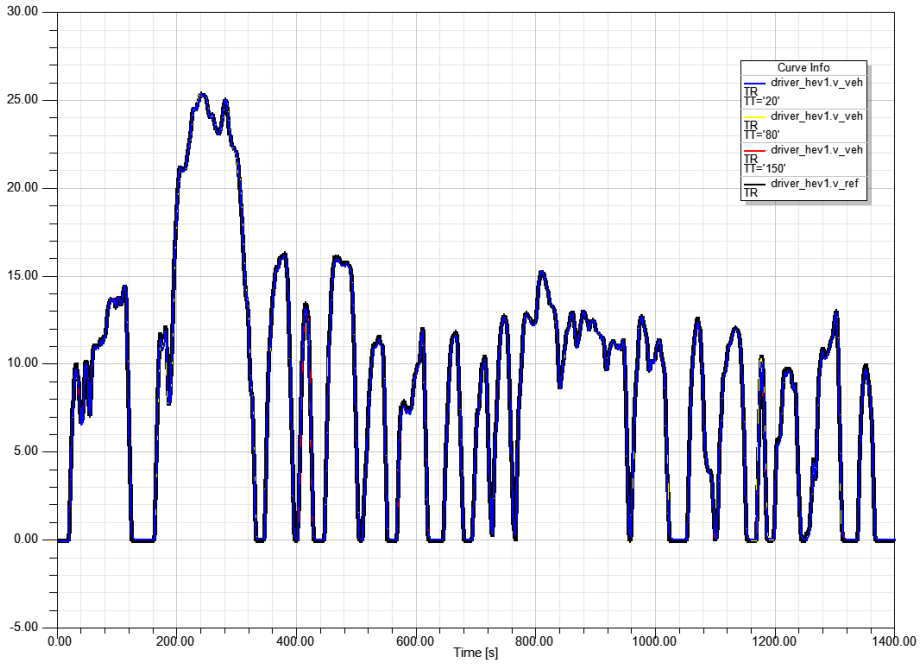

Figure 6.9: City drive cycle FTP 75

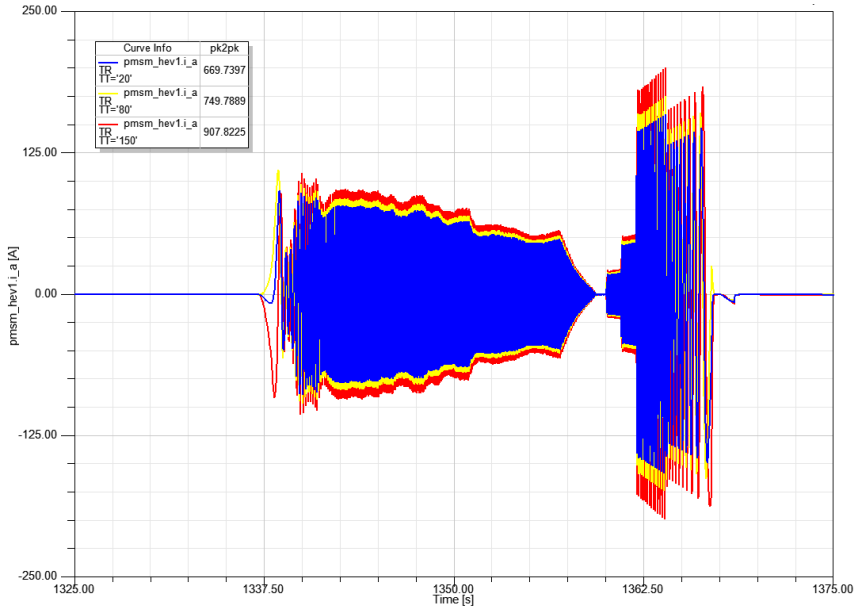

Figure 6.10: Phase A current from 1325 to 1375 second at 20, 80, 150 °C

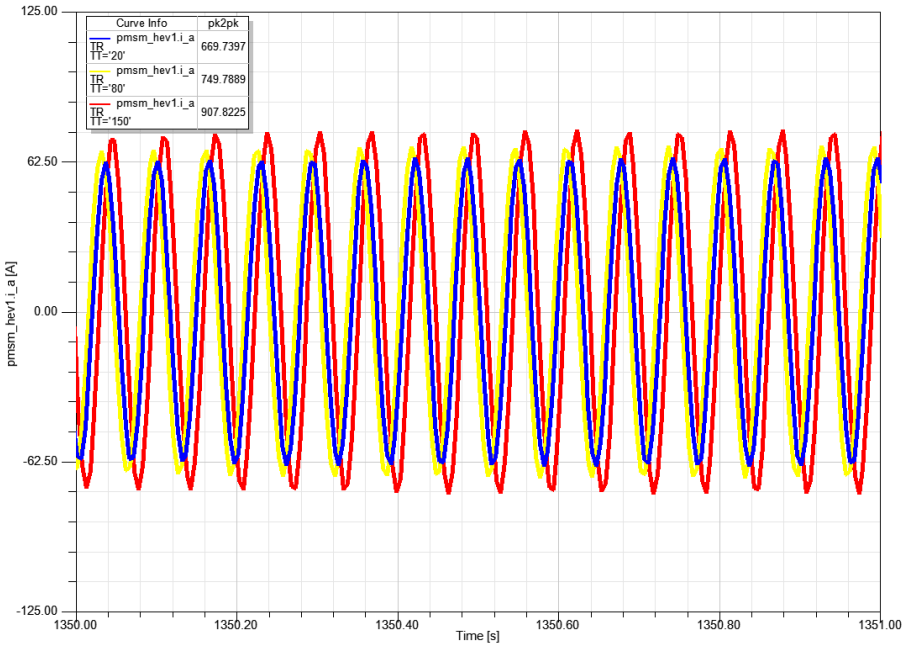

Figure 6.11: Phase A current from 1350 to 1351 second at 20, 80, 150 °C

6.4. Summary

The vehicle system becomes more and more complicated when involving the electrical propulsion part. Multi-domain, mixed-signal system level modeling and simulation techniques are critical for design and validation purposes. In this work, we presented a VHDL-AMS based HEV library. The mathematical implementation of the individual components is discussed. Simulation results of HEV, CV, and EV models are presented. We have also shown the proposed temperature dependent IPM motor can be used in the HEV system level simulation.

CHAPTER 7: CONCLUSION AND FUTURE WORK

In this dissertation, the electrical battery and IPM motor has been studied from both device and system level perspectives considering multi-physics phenomenon. Fundamental vehicle system level simulation has also been presented.

In Chapter 2, a novel circuit-CFD methodology of analysis has been proposed for HEV/EV battery thermal management design. The model consists of a heat generating electrical circuit model and a CFD model. The model provides temperature distribution of the battery while having an accurate runtime heat generation mechanism. The analysis can be used to predict electrical terminal performance but most importantly the temperature distribution that are due to various battery geometries, materials, current loadings, and cooling conditions. Implementation, simulation results, and validation have been provided for the 4-cell battery model under 3 current loading conditions. Finally, a 6-cell and a 16-cell battery models have been presented to show the flexibility and scalability of the proposed model for implementation in engineering design and development.

In Chapter 3, we have shown that we can represent the battery thermal system as a Foster matrix if the system is a LTI system. Foster network model gives the same results as the CFD model. The simulation time of the Foster network is order of magnitude less than that of the CFD model. However, to calibrate the Foster network model, step responses from either CFD simulation or lab testing are required. We have shown that the Foster network can replace the traditional thermal network, and the Foster network approach is more accurate. The Foster network will give identical results as the CFD model if the thermal system satisfies linear and

time invariant assumptions. However in reality, most thermal systems are nonlinear. We have shown for battery cooling applications, even with nonlinear effects, the results will only differ by 2% with a 90 K temperature rise. Most battery cooling applications will have temperature rise less than 90 K, therefore smaller than 2% difference in results can be expected.

In Chapter 4, we have shown that temperature dependency of the magnets of the IPM has significant impact to its performance. The torque of IPM decreases as temperature increases due to reversible and irreversible demagnetization. And when the control angle is greater than 90 degree, the magnets of IPM are more susceptible to irreversible demagnetization due to temperature rise. Also the maximum torque control angle may differ at various temperatures. In addition, the flux linkage and induced voltages increases with temperature. Interestingly, The IPM motor tends to lose its saliency as temperature rises, or even reverse its saliency, depending on the operating control angle. Finally, a non-uniform temperature distribution could change the machine performance significantly. Therefore detailed thermal model is necessary to capture the non-uniform thermal effects on the IPM performance.

In Chapter 5, we acknowledged the IPM motor is load and temperature dependent and we have proposed a novel reduced order IPM model based on FEA that takes into account the PM temperature impact. The theory and detailed implementation has been presented, finally, we have shown that the proposed model result is in excellent agreement with the FEA results.

In Chapter 6, we presented a VHDL-AMS based HEV library. The mathematical implementation of the individual components is discussed. Results are presented for typical

vehicle applications using the library components. We have also incorporated the proposed temperature dependent IPM model in the HEV simulation.

In conclusion, vehicle systems become more and more complicated when involving the electrical propulsion, and batteries and IPMs are especially important in such systems because they provide sustaining power for the vehicles. While multi-domain, mixed-signal system level modeling and simulation techniques are used for design and validation, batteries and IPM motors should also be studied in great details on the device level considering the multi-physics phenomenon. The final system integration engineer must keep a good balance between the system level and device level studies to achieve an optimized vehicle drive design. For future work, we will develop accurate reduced order thermal model for the IPM, along with the proposed reduced order IPM model, we will strive to invent novel optimized control algorithm to achieve even higher efficiency.

LIST OF REFERENCES

[1] M. de Koning, A. Veltman, and P. van den Bosch, "Modeling battery efficiency with parallel branches," in *Proc. IEEE 35th Annu. Power Electron. Spec. Conf.*, Jun. 2004, vol. 1, pp. 141–147.

[2] C. Brandolese, W. Fornaciari, L. Pomante, F. Salice, and D. Sciuto, "A multi-level strategy for software power estimation," in *Proc. 13th Int. Symp. Synth.*, 2000, pp. 187–192.

[3] H. Visairo and P. Kumar, "A reconfigurable battery pack for improving power conversion efficiency in portable devices," in *Proc. 7th Int.Caribbean Conf. Devices, Circuits Syst.*, Apr. 2008, pp. 1–6.

[4] M. Alahmad and H. Hess, "Reconfigurable topology for JPLs rechargeable micro-scale batteries," in *Proc. 12th NASA Symp. VLSI Des.*, Coeur dAlene, ID, 2005, pp. 4–5.

[5] S. Ci, J. Zhang, H. Sharif, and M. Alahmad, "A novel design of adaptive reconfigurable multicell battery for power-aware embedded networked sensing systems," in *Proc. IEEE Global Telecommun. Conf.*, Nov. 2007, pp. 1043–1047.

[6] R. Rao, S. Vrudhula, and D. Rakhmatov, "Battery modeling for energy aware system design," *Computer*, vol. 36, no. 12, pp. 77–87, Dec. 2003.

[7] D. N. Rakhmatov and S. B. K. Vrudhula, "An analytical high-level battery model for use in energy management of portable electronic systems," in *Proc. Int. Conf. Comput. Aided Des.*, 2001, pp. 488–493.

[8] M. Chen and G. Rincon-Mora, "Accurate electrical battery model capable of predicting runtime and i-v performance," *IEEE Trans. EnergyConvers.*, vol. 21, no. 2, pp. 504–511, Jun. 2006.

[9] J. Zhang, S. Ci, H. Sharif, and M. Alahmad, "An enhanced circuit-based model for single-cell battery," in *Proc. IEEE Conf. Appl. Power Electron. Conf. Expo.*, Plam Sprints, CA, Fab. 2010, pp. 672–675.

[10] R. Spurrett, C. Thwaite, A. Holland, D. Lizius, and G. Dudley, "Modeling of highly-parallel lithium-ion batteries," in *Proc. Eur. Space Power Conf.*, Porto, Portugal, 2002, vol. 502, pp. 685–691.

[11] M.Wua, C. Linb,Y.Wangb, C.Wanb, andC.Yang, "Numerical simulation for the discharge behaviors of batteries in series and/or parallel-connected battery pack," *Electrochim. Acta*, vol. 52, no. 3, pp. 1349–1357, 2006.

[12] T. Matsushita, K. Yabuta, T. Tsujikawa, T. Matsushima, M. Arakawa, and K. Kurita, "Construction of three-dimensional thermal simulation model of lithium-ion secondary battery," in *Proc. IEEE 30th Int. Telecommun. Energy Conf.*, Sep. 2008, pp. 1–6.

[13] W. X. Shen, C. C. Chan, E. W. C. Lo, and K. T. Chau, "Estimation of battery available capacity under variable discharge currents," *J. Power Sources*, vol. 103, no. 2, pp. 180–187, 2002.

[14] P. Rong andM. Pedram, "An analytical model for predicting the remaining battery capacity of lithium-ion batteries," *IEEE Trans. Very Large Scale Integr. Syst.*, vol. 14, no. 5, pp. 441–451, May 2006.

[15] S. Abu-Sharkh and D. Doerffel, "Rapid test and non-linear model characterization of solid-state lithium-ion batteries," *J. Power Sources*, vol. 130, no. 1–2, pp. 266–274, 2004.

[16] B. Schweighofer, K. Raab, and G. Brasseur, "Modeling of high power automotive batteries by the use of an automated test system," *IEEE Trans. Instrum. Meas.*, vol. 52, no. 4, pp. 1087–1091, Aug. 2003.

[17] M. Alahmad and H. Hess, "Evaluation and analysis of a new solid-state rechargeable microscale lithium battery," *IEEE Trans. Ind. Electron.*, vol. 55, no. 9, pp. 3391–3401, Sep. 2008.

[18] L. Benini, G. Castelli, A. Macci, E. Macci, M. Poncino, and R. Scarsi, "Discrete-time battery models for system-level low-power design," *IEEE Trans. VLSI Syst.*, vol. 9, no. 5, pp. 630–640, Oct. 2001.

[19] C. J. Zhan, X. G.Wu, V. K. Ramachandaramurthy,M. Barnes, N. Jenkins, and A. J. Ruddell, "Two electrical models of the lead-acid battery used in a dynamic voltage restorer," in *IEE Proc. Generation, Transmission, and Distribution*, vol. 150, no. 2, Mar., pp. 175–182, 200.

[20] M. Pedram and Q. Wu, "Design considerations for battery-powered electronics," in *Proc. 1999 Des. Autom. Conf.*, pp. 861–866.

[21] P. H. Chou, C. Park, J. Park, K. Pham, and J. Liu, "B#: A battery emulator and power profiling instrument," in *Proc. Int. Symp. Low Power Design*, 2003, pp. 288–293.

[22] C. F. Chiasserini and R. R. Rao, "Energy efficient battery management," *IEEE J. Sel. Areas Commun.*, vol. 19, no. 7, pp. 1235–1245, Jul. 2001.

[23] L. Song and J. W. Evans, "Electrochemical-thermal model of lithium polymer batteries," *J. Electrochem. Soc.*, vol. 147, pp. 2086–2095, 2000.

[24] P. M. Gomadam, J. W. Weidner, R. A. Dougal, and R. E. White, "Mathematical modeling of lithium-ion and nickel battery systems," *J. Power Sources*, vol. 110, no. 2, pp. 267–24, Aug. 2002.

[25] D.W. Dennis,V. S. Battaglia, andA.Belanger, "Electrochemical modeling of lithium polymer batteries," *J. Power Source*, vol. 110, no. 2, pp. 310– 320, Aug. 2002.

[26] W. Soong and N. Ertugrul, "Field-weakening performance of interior permanent-magnet motors," *IEEE Trans. Ind. Appl.*, vol. 38, no. 5, pp. 1251–1258, Sep./Oct. 2002.

[27] M. Negrea and M. Rosu, "Thermal analysis of a large permanent magnet synchronous motor for different permanent magnet rotor configurations," in *Proc. IEEE Int. Electr. Mach. Drives Conf. 2001*, pp. 777–781.

[28] M. Rosu, A. Arkkio, T. Jokinen, J. Mantere, and J. Westerlund, "Demagnetisation

state of permanent magnets in large output power permanent magnet synchronous motor," in *Proc. IEEE Int. Electr.Mach. Drives Conf. 1999*, May, pp. 776–778.

[29] N. Demerdash, T. Nyamusa, and T. Nehl, "Comparison of effects of overload on parameters and performance of samarium-cobalt and strontium ferrite radially oriented permanent magnet brushless dc motors," *IEEE Trans. Power App. Syst.*, vol. PAS-104, no. 8, pp. 2223–2231, Aug. 1985.

[30] J. Sprooten and J.-C. Maun, "Influence of saturation level on the effect of broken bars in induction motors using fundamental electromagnetic laws and finite element simulations," *IEEE Trans. Energy Convers.*, vol. 24, no. 3, pp. 557–564, Sep. 2009.

[31] M. Aydin, S. Huang, and T. Lipo, "Optimum design and 3d finite element analysis of nonslotted and slotted internal rotor type axial flux pm disc machines," in *Proc. IEEE Power Eng. Soc. SummerMeeting, 2001*, vol. 3,

[32] S. Salon, Finite Element Analysis of Electrical Machines. Boston, MA: Kluwer, 1995.

[33] N. Bianchi, Electrical Machine Analysis Using Finite Elements. Boca Raton, FL: CRC Press, 2005.

[34] J. R. Hendershot and T. J. E. Miller, Design of Brushless Permanent-Magnet Motors. Mentor, OH: Magna Phys., 1994.

[35] E. C. Lovelace, T. M. Jahns, and J. Lang, "A saturating lumped-parameter model for an interior PM synchronous machine," IEEE Trans. Ind. Appl., vol. 38, no. 3, pp. 645–650, May/Jun. 2002.

[36] O. A.Mohammed, S. Liu, and Z. Liu, "Physical modeling of PMsynchronous motors for integrated coupling with machine drives," IEEE Trans. Magn., vol. 41, no. 5, pp. 1628–1631, May 2005.

[37] N. Demerdash and H. Hamilton, "Effect of rotor asymmetry on field forms and eddy current losses in stator conductors due to radial flux," IEEE Trans. Power App. Syst., vol. PAS-91, no. 5, pp. 1999–2010, Sep. 1972.

[38] F. A. Fouad, T. W. Nehl, and N. Demerdash, "Magnetic field modeling of permanent magnet type electronically operated synchronous machines using finite elements," IEEE Trans. Power App. Syst., vol. PAS-100, no. 9, pp. 4125–4133, Sep. 1981.

[39] R. Schiferl and T. Lipo, "Core loss in buried magnet permanent magnet synchronous motors," *IEEE Trans. Energy Convers.*, vol. 4, no. 2, pp. 279–284, Jun. 1989.

[40] S. Williamson, L. Lim, and M. Robinson, "Finite-element models for cage induction motor analysis," *IEEE Trans. Ind. Appl.*, vol. 26, no. 6, pp. 1007–1017, Nov./Dec. 1990.

[41] S. Williamson, T. Flack, and A. Volschenk, "Representation of skew in time-stepped two-dimensional finite-element models of electrical machines," *IEEE Trans. Ind. Appl.*, vol. 31, no. 5, pp. 1009–1015, Sep./Oct. 1995.

[42] T. Miller, M. Popescu, C. Cossar, M. McGilp, M. Olaru, A. Davies, J. Sturgess, and A. Sitzia, "Embedded finite-element solver for computation of brushless permanent-magnet motors," *IEEE Trans. Ind. Appl.*, vol. 44, no. 4, pp. 1124–1133, Jul./Aug. 2008.

[43] A. Knight and Y. Zhan, "Identification of flux density harmonics and resulting iron losses in induction machines with nonsinusoidal supplies," *IEEE Trans. Magn.*, vol. 44, no. 6, pp. 1562–1565, Jun. 2008.

[44] D. M. Ionel and M. Popescu, "Finite element surrogate model for electric machines with revolving field—Application to IPM motors," *IEEE Trans. Ind. Appl.*, vol. 46, no. 6, pp. 2424–2433, Nov./Dec. 2010.

[45] D. M. Ionel, M. Popescu, M. I. McGilp, T. J. E.Miller, S. J. Dellinger, and R. J. Heideman, "Computation of core losses in electrical machines using improved models for laminated steel," *IEEE Trans. Ind. Appl.*, vol. 43, no. 6, pp. 1554–1564, Nov./Dec. 2007.

[46] J. F. Eastham, *FEA of Electrical Machines—Private Communication*. Bath, U.K.: Univ. Bath, 1994.

[47] D. M. Ionel, M. Popescu, M. I. McGilp, T. J. E.Miller, and S. J. Dellinger, "Assessment of torque components in brushless permanent-magnet machines through numerical analysis of the electromagnetic field," *IEEE Trans. Ind. Appl.*, vol. 41, no. 5, pp. 1149–1158, Sep./Oct. 2005.

[48] J. Eastham, D. Ionel, M. Balchin, T. Betzer, and E. Demeter, "Finite element analysis of an interior-magnet brushless dc machine, with a step-skewed rotor," *IEEE Trans. Magn.*, vol. 33, no. 2, pp. 2117–2119, Mar. 1997.

[49] D. M. Ionel and S. J. Dellinger, "Brushless permanent magnet machine with reduced cogging and torque ripple and method of producing the same," U.S. Patent 6 940 198, Sep. 6, 2005.

[50] D. M. Ionel, M. V. Cistelecan, T. J. E. Miller, and M. I. McGilp, "A new analytical method for the computation of air-gap reactances in 3-phase induction motors," in *Conf. Rec. IEEE IAS Annu. Meeting*, Oct. 1998, vol. 1, pp. 65–72.

[51] W. L. Soong, D. A. Staton, and T. J.E. Miller, "Design of a new axiallylaminated interior permanent magnet motor," *IEEE Trans. Ind. Appl.*, vol. 31, no. 2, pp. 358–367, Mar./Apr. 1995.

[52] Y. Honda, T. Higaki, S. Morimoto, and Y. Takeda, "Rotor design optimization of multi-layer interior permanent-magnet synchronous motor," *IEEE Proc. Electr. Power Appl.*, vol. 145, no. 2, pp. 119–124, Mar. 1998.

[53] R. Dutta andM. F. Rahman, "Design and analysis of an interior permanent magnet (IPM) machine with very wide constant power operation range," *IEEE Trans. Energy Convers.*, vol. 23, no. 1, pp. 25–33, Mar. 2008.

[54] M. Kamiya, "Development of traction drive motors for the toyota hybrid system," *Trans. Inst. Electr. Eng. Jpn.*, vol. 126, pp. 473–479, 2006.

[55] A. M. El-Refaie, T. M. Jahns, P. J.McCleer, and J. W. McKeever, "Experimental verification of optimal flux weakening in surface PM Machines using concentrated windings," *IEEE Trans. Ind. Appl.*, vol. 42, no. 2, pp. 443–453, Mar.–Apr. 2006.

[56] N. Bianchi, S. Bolognani,M. D. Pre, and G. Grezzani, "Design considerations for fractional-slot winding configurations of synchronous machines," *IEEE Trans. Ind. Appl.*, vol. 42, no. 4, pp. 997–1006, Jul.–Aug. 2006.

[57] N.Bianchi, S. Bolognani, and M. Dai Pre, "Magnetic loading of fractional slot three-phase PM motors with non overlapped coils," *IEEE Trans. Ind. Appl.*, vol. 44, no. 5, pp. 1513–1521, Sep–Oct. 2008.

[58] Y. Honda, T. Nakamura, T. Higaki, and Y. Takeda, "Motor design consideration and test results of an interior permanent magnet synchronous motor for electrical vehicles," in *Proc. Annu. Meeting IEEE Ind. Appl. Soc.*, 1997, pp. 75–82.

[59] J. Cros and P. Viarouge, "Synthesis of high performance PM motors with concentrated windings," *IEEE Trans. Energy Convers.*, vol. 17, no. 2, pp. 248–253, Jun. 2002.

[60] F. Magnussen and C. Sadarangani, “Winding factors and Joule losses of permanent magnet machines with concentrated windings,” in *Proc. IEEE Int. Elect. Mach. Drives Conf.*, 2003, pp. 333–339.

[61] P. B. Reddy, A. El-Refaie, H. Kum-Kang, J. K. Tangudu, and T. M. Jahns, “Comparison of interior and surface PM machines equipped with fractional-slot concentrated windings for hybrid traction applications,” in *Proc. Energy Convers. Congr. Expo.*, 2011, pp. 2252–2259.

[62] J. K. Tangudu, T. M. Jahns, and T. P. Bohn, “Design, analysis and loss minimization of a fractional-slot concentrated winding IPM machine for traction applications,” in *Proc. IEEE Energy Convers. Congr. Expo.*, 2011, pp. 2236–2243.

[63] L. J. Wu, Z. Q. Zhu, J. T. Chen, Z. P. Xia, and G. W. Jewell, “Optimal split ratio in fractional-slot interior permanent-magnetmachines with nonoverlapping windings,” *IEEE Trans.Magn.*, vol. 46, no. 5, pp. 1235–1242, May 2010.

[64] M. S. Islam, S. Mir, T. Sebastian, and S. Underwood, “Design considerations of sinusoidally excited permanent-magnetMachines for low-torqueripple applications,” *IEEE Trans. Ind. Appl.*, vol. 41, no. 4, pp. 955–962, 2005.

[65] J. K. Tangudu, T. M. Jahns, and A. El-Refaie, “Unsaturated and saturated saliency trends in fractional-slot concentrated-winding interior permanent magnet machines,” in *Proc. IEEE Energy Convers. Congr. Expo.*, 2010, pp. 1082–1089.

[66] N. Bianchi, S. Bolognani, and P. Frare, “Design criteria for high-efficiency SPM synchronous motors,” *IEEE Trans. Energy Convers.*, vol. 21, no. 4, pp. 396–404, Jul.–Aug. 2006.

[67] D. Evans, Z. Azar, L. J.Wu, and Z. Q. Zhu, “Comparison of optimal design and performance of PM machines having non-overlapping windings and different rotor topologies,” in *Proc. Power 5th IET Electron.,Mach. Drives Conf.*, 2010, pp. 1–7.

[68] R. Dutta, M. Rahman, and L. Chong, “Winding inductances of an Interior permanent magnet (IPM) machine with fractional slot concentrated winding,” *IEEE Trans. Magn.*, to be published.

[69] L. Ji-Young, L. Sang-Ho, L. Geun-Ho, H. Jung-Pyo, and H. Jin, “Determination of parameters considering magnetic nonlinearity in an interior permanentmagnet synchronous motor,” *IEEE Trans.Magn.*, vol. 42, no. 4, pp. 1303–1306, Apr. 2006.

[70] E. C. Lovelace, T. M. Jahns, and J. H. Lang, “A saturating lumped-parameter model for an interior PM synchronous machine,” *IEEE Trans. Ind. Appl.*, vol. 38, no. 3, pp. 645–650, May/Jun. 2002.

[71] K. J. Meessen, P. Thelin, J. Soulard, and E.A. Lomonova, "Inductance calculations of permanent-magnet synchronous machines including flux change and self- and cross-saturations," *IEEE Trans. Magn.*, vol.44, no. 10, pp. 2324–2331, Oct. 2008.

[71] Y. S. Chen, Z. Q. Zhu, and D. Howe, "Calculation of d- and q-axis inductances of PM brushless ac machines accounting for skew," *IEEE Trans. Magn.*, vol. 41, no. 10, pp. 3940–3942, Oct. 2005.

[73] R. Dutta and M. F. Rahman, "A comparative analysis of two test methods of measuring d- and q-axes inductances of interior permanent-magnet machine," *IEEE Trans. Magn.*, vol. 42, no. 11, pp. 3712–3718, Nov. 2006.

[74] K. M. Rahman and S. Hiti, "Identification of machine parameters of a synchronous motor," *IEEE Trans. Ind. Appl.*, vol. 41, no. 2, pp.557–565, Mar./Apr. 2005.

[75] S. L. Kellner, M. Seilmeier, and B. Piepenbreier, "Impact of iron losses on parameter identification of permanent magnet synchronous machines," in *Proc. 1st Int. Electr. Drives Production Conf.*, 2011, pp. 11–16.

[76] J. F. Gieras, E. Santini, and M. Wing, "Calculation of synchronous reactances of small permanent-magnet alternating-current motors: Comparison of analytical approach and finite element method with measurements," *IEEE Trans. Magn.*, vol. 34, no. 5, pp. 3712–3720, Sep. 1998.

[77] D. Pavlik, V. K. Garg, J. R. Repp, and J. Weiss, "A finite element technique for calculating the magnet sizes and inductances of permanent magnet machines," *IEEE Trans. Energy Convers.*, vol. 3, no. 1, pp. 116–122, Mar. 1988.

[78] G. Kang, J. Hong, G. Kim, and J. Park, "Improved parameter modeling of interior permanent magnet synchronous motor based on finite element analysis," *IEEE Trans. Magn.*, vol. 36, no. 4, pp. 1867–1870, Jul. 2000.

[79] L. Chang, "An improved FE inductance calculation for electrical machines," *IEEE Trans. Magn.*, vol. 32, no. 4, pp. 3237–3245, Jul. 1996.

[80] N. A. Demerdash and T. W. Nehl, "Electric machinery parameters and torques by current and energy perturbations from field computations. II. Applications and results," *IEEE Trans. Energy Convers.*, vol. 14, no. 4, pp. 1514–1522, Dec. 1999.

[81] T. J. E. Miller, M. Popescu, C. Cossar, and M. McGilp, "Performance estimation of interior permanent-magnet brushless motors using the voltage-driven flux-MMF diagram," *IEEE Trans. Magn..*, vol. 42, no. 7, pp. 1867–1872, Jul. 2006.

[82] L. Ji-Young, L. Sang-Ho, L. Geun-Ho, H. Jung-Pyo, and H. Jin, "Determination of parameters considering magnetic nonlinearity in an interior permanent magnet synchronous motor," *IEEE Trans. Magn..*, vol. 42, no. 4, pp. 1303–1306, Apr. 2006.

[83] K. M. Rahman and S. Hiti, "Identification of machine parameters of a synchronous motor," in *Industry Applications Conf. 38th IAS Annu. Meeting*, vol. 1, Oct. 12–16, 2003, pp. 409–415.

[84] E. C. Lovelace, T. M. Jahns, and J. H. Lang, "A saturating lumped-parameter model for an interior PM synchronous machine," *IEEE Trans. Ind. Appl.*, vol. 38, no. 3, pp. 645–650, May/Jun. 2002.

[85] A. Chiba and F. Nakamura, "Inductance of cageless reluctance-synchronous machines having nonsinusoidal space distribution," *IEEE Trans. Ind. Appl.*, vol. 27, no. 1, pp. 44–51, Jan./Feb. 1991.

[86] E. C. Lovelace, T. M. Jahns, J. Wai, T. Keim, J. H. Lang, D. D. Wentzloff, F. Leonardi, and J. M. Miller, "Design and experimental verification of a direct-drive interior PM synchronous machine using a saturable lumped-parameter model," in *Industry Applications Conf. 37th IAS Annu. Meeting*, vol. 4, Oct. 13–18, 2002, pp. 2486–2492.

[87] B. ˇStumberger, G. ˇStumberger, D. Dolinar, A. Hamler, and M. Trlep, "Evaluation of saturation and cross-magnetization effects in interior permanent- magnet synchronous motor," *IEEE Trans. Ind. Appl.*, vol. 39, no 5, pp. 1264–1271, Sep./Oct. 2003.

[88] R. H. Engelmann and W. H. Middendorf, *Handbook of Electric Motors*. New York: Marcel Dekker, 1995.

[89] M. A. Rahman and P. Zhou, "Analysis of brushless permanent magnet synchronous motors," *IEEE Trans. J. Ind.*, vol. 43, no. 2, pp. 256–267,Apr. 1996.

[90] J. F. Gieras, E. Santini, and M. Wing, "Calculation of synchronous reactances of small permanent-magnet alternating-current motors: Comparison of analytical approach and finite element method with measurements," *IEEE Trans. J. Magn.*, vol. 34, no. 5, pp. 3712–3720, Sept. 1998.

[91] A. M. El-Serafi and A. S. Abdallah, "Saturated synchronous reactances of synchronous machines," *IEEE Trans. J. Ener.*, vol. 7, no. 3, pp. 570–579, Sept. 1992.

[92] L. Chang, "In improved FE inductance calculation for electrical machine," *IEEE Trans. J. Magn.*, vol. 32, no. 4, pp. 3237–3245, July 1996.

[93] E. Levi, "Saturation modeling in D-Q axis models of salient pole synchronous machines," *IEEE Trans. J. Ener.*, vol. 14, no. 1, pp. 44–50, Mar. 1999.

[94] N. Bianchi, S. Bolognani, and G. Eason, Magnetic models of saturated interior permanent magnet motors base on finite element analysis, .

[95] M. Sanada, S. Morimoto, and Y. ta keda, "Interior permanent magnet linear synchronous motor for high-performance drives," *IEEE Trans. J. Ind.*, vol. 33, no. 3, pp. 966–972, July/Aug. 1997.

[96] A. H.Wijenayake and P. B. Schmidt, "Modeling and analysis of permanent magnet synchronous motor by taking saturation and core loss into account," in *Proc. PEDS 97*, May 1997, pp. 530–534.

[97] I. Iglesias, L. Garcia-Tabares, and J. Tamarit, "A d–q model for the selfcommutated synchronous machine considering the effects of magnetic saturation," *IEEE Trans. Energy Conversion*, vol. 7, pp. 768–776, Dec. 1992.

[98] E. Levi, "Saturation modeling in d–q axis models of salient pole synchronous machines," IEEE Trans. Energy Conversion, vol. 14, pp. 44–50, Mar. 1999.

[99] E. Levi and V. A. Levi, "Impact of dynamic cross-saturation on accuracy of saturated synchronous machine models," *IEEE Trans. Energy Conversion*, vol. 15, pp. 224–230, June 2000.

[100] M. Trlep, P. ˇSkerget, B. Kreˇca, and B. Hribernik, "Hybrid finite-element- boundary element method for nonlinear electromagnetic problems," *IEEE Trans. Magn.*, vol. 31, pp. 1380–1383, May 1995.

[101] D. Ghosh, P. D. Maguire and D. X. Zhu, "Design and CFD simulation of a battery module for a hybrid electric vehicle battery pack," presented at SAE World Congr. & Exhibition, Detroit, Michigan, United States, 2009.

[102] M. Zolot, K. Kelly, M. Keyser, M. Mihalic, A. Pesaran, and A. Hieronymus, "Thermal evaluation of the Honda insight battery pack," presented at the 36th Intersociety Energy Conversion Eng. Conf., Savannah, Georgia, United States, 2001.

[103] M. Doyle, T.F. Fuller, and J. Newman, "Modeling of Galvanostatic Charge and Discharge of the Lithium/Polymer/Insertion Cell", *Journal of Electrochem*. Soc., vol. 140, pp. 1526-1533, 1993.

[104] M. Doyle, J. Newman, "Comparison of Modeling Predictions with Experimental Data from Plastic Lithium Ion Cells", *Journal of Electochem*. Soc., vol .143, pp. 1890-1903, 1996.

[105] M. Chen and G. A. Rincon-Mora, "Accurate electrical battery model capable of predicting runtime and performance," *IEEE Trans. Energy Convers.*, vol. 21, no. 2, pp. 504–511, Jun. 2006.

[106] L. Gao, S. Liu, and R. A. Dougal, "Dynamic lithium-ion battery model for system simulation," *IEEE Trans. Compon. Packag. Technol.*, vol. 25, no. 3, pp. 495-505, Sep. 2002.

[107] J. Jang and J. Yoo, "Equivalent circuit evaluation method of lithium polymer battery using Bode plot and numerical analysis," *IEEE Trans. Energy Convers.*, vol. 26, no. 1, pp. 290-298, Mar. 2011.

[108] J. Zhang, S. Ci, H. Sharif and M. Alahmad, "Modeling discharge behavior of multicell battery," *IEEE Trans. Energy Convers.* , vol. 25, no. 4, pp. 1133-1141, Dec. 2010.

[109] T. Kim and W. Qiao, "A hybrid battery model capable of capturing dynamic circuit characteristics and nonlinear capacity effects," *IEEE Trans. Energy Convers.*, vol. 26, no. 4, pp. 1172-1180, Dec. 2011.

[110] S. Lin, S. Stanton, W. Lian and T. Wu, "Battery modeling based on the coupling of electrical circuit and computational fluid dynamics," Energy Conversion Congress and Exposition, Phoenix, AZ, 2011, pp.2622-2627.

[111] J. R. Pillai and B. Bak-Jensen, "Integration of vehicle-to-grid in the Western Danish power system," *IEEE Trans. Sustain. Energy*, vol. 2, no. 1, pp. 12-19, Jan. 2011.

[112] M. A. Roscher, O. S. Bohlen and D. U. Sauer, "Reliable state estimation of multicell lithium-ion battery systems," *IEEE Trans. Energy Convers.*, vol. 26, no. 3, pp. 737-743, Sep. 2011.

[113] L. Wang, M. P. Polis, G. G. Yin, W. Chen, Y. Fu and C.C. Mi, "Battery cell identification and SOC estimation using string terminal voltage measurements," *IEEE Trans. Veh. Technol.*, vol. 61, no. 7, pp. 2925–2935, Sep. 2012.

[114] M. Urbain, M. Hinaje, S. Raël, B. Davat, and P. Desprez, "Energetical modeling of lithium-ion batteries including electrode porosity effects," *IEEE Trans. Energy Convers.*, vol. 25, no. 3, pp. 862-872, Sep. 2010.

[115] S. Grillo, M. Marinelli, S. Massucco and F. Silvestro, "Optimal management strategy of a battery-based storage system to improve renewable energy integration in distribution networks," *IEEE Trans. Smart Grid*, vol. 3, no. 2, pp. 950-958, Jun. 2012.

[116] W. X. Shen, C. C. Chan, E. W. C. Lo, and K. T. Chau, "Estimation of battery available capacity under variable discharge currents, " *Journal of Power Sources*, vol. 103, no. 2, pp. 180-187, Jan. 2002.

[117] P. Rong and M. Pedram, "An analytical model for predicting the remaining battery capacity of lithium-ion batteries," *IEEE Trans. Very Large Scale Integr. (VLSI) Syst*., vol. 14, no. 5, pp. 441-451, May. 2006.

[118] B. Schweighofer, K. M. Raab, and G. Brasseur, "Modeling of high power automotive batteries by the use of an automated test system," *IEEE Trans. Instrum. Meas.*, vol. 52, no. 4, pp. 1087-1091 Aug. 2003.

[119] X. Hu, L. Collins, S. Stanton, S. Jiang, "A model parameter identification method for battery applications," SAE Technical Paper 2013-01-1529, 2013, doi:10.4271/2013-01-1529.

[120] X. Hu, S. Lin, S. Stanton and W. Lian, "A Foster network thermal model for HEV/EV battery modeling," *IEEE Trans. Ind. Appl.*, vol. 47, no. 4, pp. 1692-1699, Jul. 2011.

[121] S. Karagol and M. Bikdash, "Generation of equivalent-circuit models from simulation data of a thermal system," *IEEE Trans. Power Electron.*, vol. 25, no. 4, pp. 820-828, Apr. 2010.

[122] G. Swift, T.S. Molinski and W. Lehn, "A fundamental approach to transformer thermal modeling. I. Theory and equivalent circuit," *IEEE Trans. Power Del.*, vol. 16, no. 2, pp. 171-175, Apr. 2001.

[123] C. Kral, A. Haumer, M. Haigis, H. Lang and H. Kapeller, "Comparison of a CFD analysis and a thermal equivalent circuit Model of a TEFC induction machine with measurements," *IEEE Trans. Energy Convers.*, vol. 24, no. 4, pp. 809-818, Dec. 2009.

[124] X. Hu, S. Lin, S. Stanton, and W. Lian, "A state space thermal model for HEV/EV battery modeling," SAE Technical Paper 2011-01-1364, 2011, doi:10.4271/2011-01-1364.

[125] M. Doyle, T.F. Fuller, and J. Newman, "Modeling of Galvanostatic Charge and Discharge of the Lithium/Polymer/Insertion Cell", *Journal of Electrochem*. Soc., vol. 140, pp. 1526-1533, 1993.

[126] M. Doyle, J. Newman, "Comparison of Modeling Predictions with Experimental Data from Plastic Lithium Ion Cells", *Journal of Electochem*. Soc., vol .143, pp. 1890-1903, 1996.

[127] X. Hu, Battery Thermal Management and Design Using Numerical Simulation to Accelerate Battery Development, ANSYS Journal Article, 2010.

[128] M. Chen and G. A. Rincon-Mora, "Accurate electrical battery model capable of predicting runtime and I–V performance," *IEEE Trans. Energy Convers.*, vol. 21, no. 2, pp. 504–511, Jun. 2006.

[129] Lijun Gao, Shengyi Liu, and Roger A. Dougal, "Dynamic Lithium-Ion Battery Model for System simulation", *IEEE Trans. Comp. Package. Technology*, vol. 25, No 3, pp.495-505, Sep. 2002.

[130] S.X. Chen , K.J. Tseng, and S.S. Choi, "Modeling of Lithium-Ion Battery for Energy Storage System Simulation", Power and Energy Engineering Conference, 2009. APPEEC 2009. Asia-Pacific 27-31 March 2009 Page(s):1-4.

[131] Roger Stout, "Linear Superposition Speeds Thermal Modeling", Part One, *Power Electronics Technology*, pp. 22-25, Jan. 2007.

[132] Roger Stout, "Linear Superposition Speeds Thermal Modeling", Part Two, *Power Electronics Technology*, pp. 28-33, Feb. 2007.

[133] B.P. Lathi, Signals and Systems, Oxford, 2002.

[134] Alan V. Oppenheim, Alan S. Willsky, with S. Hamid Nawab, Signals and Systems, Prentice Hall, 1996.

[135] D. G. Dorrell, M. Hsieh, M. Popescu, L. Evans, D. A. Staton, V. Grout, "A review of the design issues and techniques for radial-flux brushless surface and internal rare-earth permanent-magnet motors," *IEEE Trans. Ind. Electron.*, vol.58, no.9, pp.3741-3757, Sep. 2011.

[136] P. Zhou, D. Lin, Y. Xiao, N. Lambert, M. A. Rahman, "Temperature-dependent demagnetization model of permanent magnets for finite element analysis," *IEEE Trans. Magn.*, vol.48, no.2, pp.1031-1034, Feb. 2012.

[137] Dexter Magnetic Technologies. http://www.dextermag.com/N5211

[138] J. S. Hsu *et al*, "Report on Toyota/Prius motor torque capability, torque property, no-load back EMF, and mechanical losses," Oak Ridge National Laboratory, Oak Ridge Institute for Science and Education, ORNL/TM-2004/185.

[139] D. G. Dorrell, M. Hsieh, A. M. Knight, "Alternative rotor designs for high performance brushless permanent magnet machines for hybrid electric vehicles," *IEEE Trans. Magn.*, vol.48, no.2, pp.835-838, Feb. 2012.

[140] M. Kamiya, Y. Kawase, T. Kosaka, N. Matsui, "Temperature distribution analysis of permanent magnet in interior permanent magnet synchronous motor considering pwm carrier harmonics," in *Proc. ICEMS.*, 2007, pp.2023-2027.

[141] Zhang, M. 2011. "HEV Powertrain Fundamentals." In the 2011 IEEE Vehicle Power and Propulsion Conference, Chicago, IL: 1-144.

[142] Ashenden, P.J., G.D. Peterson and D.A. Teegarden. 2003. *The System Designer's Guide to VHDL-AMS*. Morgan Kaufmann Publishers.

[143] Dieselnet. 2013. http://www.dieselnet.com/standards.

[144] VDA/FAT. 2013.VDA/FAT AK30 library. http://fat-ak30.eas.iis.fhg.de/mb/index_en.html.

[145] Ehsani, M., Y. Gao and A. Emadi. 2010. *Modern Electric,Hybrid Electric, and Fuel Cell Vehicles - Fundamentals, Theory, and Design*. 2nd ed. CRC Press, Boca Raton, FL: Taylor and Francis Group, LLC.

[146] Wolm, P., X.Q. Chen, J.G. Chase, W. Pettigrew and C.E. Hann. 2008. "Analysis of a PM DC Motor Model for Application in Feedback Design for Electric Powered Mobility Vehicles." In the 15th International Conference on Mechatronics and Machine Vision in Practice, Auckland, New Zealand.

[147] Saeedi, M. 2010. "A Mean Value Internal Combustion Engine Model in MapleSim." Master Thesis, Department of Mechanical Engineering, University of Waterloo, Ontario, Canada.

[148] Samanuhut, P. 2011. "Modeling and Control of Automatic Transmission with Planetary Gears for Shift Quality." Ph.D. Dissertation, Department of Mechanical Engineering, University of Texas at Arlington, Arlington, Texas.

[149] Ehsani, M., Y. Gao and A. Emadi. 2007. "Hybrid Electric Vehicles Architecture and Motor Drives." IEEE Proceedings, 95(4): 719-728.

[150] Hedrick, J.K., J.C. Gerdes, D.B. Maciuca and D. Swaroop. 1997. "Brake System Modeling, Control and Integrated Brake/Throttle Switching: Phase I." California PATH Research Report, UCB-ITS-PRR, Institute of Transportation studies (UCB), UC Berkeley, Berkeley, California.

[151] Yi, K. and J. Chung. 2001. "Nonlinear Brake Control for Vehicle CW/CA Systems." IEEE/ASME Transactions on Mechatronics, 6(1): 17-25.

[152] Nobrant, P. 2001. "Driveline Modeling Using MathModelica." Master Thesis, Vehicular Systems, Department of Electrical Engineering, Linköpings Institute of Technology, Linköping and Norrköping, Sweden.